Models and simulation of non-ideal fluid flows in unconventional turbomachinery

Toward highly efficient next-generation green power systems

Proefschrift

ter verkrijging van de graad van doctor
aan de Technische Universiteit Delft,
op gezag van de Rector Magnificus prof. ir. K. Ch. A. M. Luyben,
voorzitter van het College voor Promoties
in het openbaar te verdedigen op
vriijdag 2 oktober 2015 om 10:00 uur.

door

Enrico RINALDI

ingegnere aeronautico, Politecnico di Milano, Italy

Dit proefschrift is goedgekeurd door de:

Promotor: Prof. dr. P. Colonna

Copromotor: Dr. R. Pecnik

Samenstelling promotiecommissie:

Rector Magnificus	voorzitter
Prof. dr. P. Colonna	Technische Universiteit Delft, promotor
Dr. R. Pecnik	Technische Universiteit Delft, copromotor

Onafhankelijke leden:

Prof. dr. J.J. Alonso	Stanford University, Verenigde Staten
Dr. A. Guardone	Politecnico di Milano, Italië
Prof. dr. S. Hickel	Technische Universiteit Delft
Prof. dr. H.W.M. Hoeijmakers	Universiteit Twente
Prof. dr. D.J.E.M. Roekaerts	Technische Universiteit Delft

ISBN 978-94-6233-090-0

Published by Enrico Rinaldi, Delft

Printed by Gilde Print in the Netherlands

Cover image adapted from https://thenounproject.com/

[1]Author e-mail address: enri.rinaldi@gmail.com

Dedicated to my mum and dad,
to Sandro, Giorgia, and Alison,
and to a cat.

Table of Contents

Summary

The new generation of power plants based on innovative thermodynamic cycles operating with unconventional working fluids, such as CO_2 close to its thermodynamic critical point or organic fluids close to their vapour saturation line, is an attractive option for high efficiency conversion of sustainable energy sources in the low and medium power output range. One of the most challenging tasks is to make this technology competitive by realizing highly efficient turbomachinery components. The main difficulty stems from the strongly non-ideal fluid dynamic behaviour of such fluids, which largely deviates from that of fluids commonly employed in standard applications. As a consequence, special design is needed, as available methods for turbomachinery of steam or gas turbine power plants cannot be used. The scarce knowledge on both the numerical modeling of non-ideal fluid flows and on their performance in turbomachinery applications makes research crucial. Computational fluid dynamics (CFD) is a powerful tool to investigate the physics of non-ideal flows and to assist the design of unconventional machines.

This thesis presents original research in the field of non-ideal fluid dynamics on three complementary aspects, namely numerical methods, applications, and theory, aiming at (i) developing new numerical schemes for the accurate and efficient CFD simulation of non-ideal compressible flows; (ii) investigating the performance of turbomachinery operating with unconventional fluids; (iii) studying the hydrodynamic stability of variable property fluid flows. The core of the report consists of five self-contained chapters, each addressing a specific problem, which are grouped into three parts according to their area of contribution.

In the first part, novel implicit schemes for the spatial discretization of the Navier–Stokes equations in the framework of the finite-volume method are introduced (Chapter 2). The look-up table approach is extensively analyzed and proposed as an accurate and efficient alternative to the direct solution of the equation of state model for fluid property evaluation. In order to address the proper handling of sub-domains interfaces needed in unsteady turbomachinery simulations, a new flux-conserving treatment of non-conformal mesh blocks interfaces is proposed in Chapter 3.

In the second part, the focus shifts to the investigation of non-ideal fluid flows in turbomachines. Chapter 4 reports the CFD computation of the performance map of a 20 mm diameter radial compressor operating with supercritical CO_2 designed for a power of 50 kW and a rotational speed of 75 krpm. Results obtained by means of Reynolds-averaged Navier–Stokes (RANS) simulations are compared to experimental measurements of isentropic efficiency and specific enthalpy rise, showing a reasonable agreement and providing a validation for the numerical schemes introduced in Chapter 2. Chapter 5

investigates the unsteady operation of a supersonic turbine for organic Rankine cycle applications using unsteady RANS simulations. The evolution of shock waves and viscous wakes and their interaction are described in details and related to the fluctuations of blade loads, which can be of the same order of magnitude of their time-averaged values, demonstrating the primary importance of performing unsteady simulations when studying such non-conventional machines.

A third part concludes the thesis presenting an analytical study of the hydrodynamic stability of a thermally-stratified channel flow with temperature dependent properties. The classical linear stability analysis framework is extended to include the effect of variable transport properties. Various distributions of thermal conductivity and specific heat across the channel height are considered in order to assess under which conditions variable properties contribute to the stabilization or destabilization of the flow. The presented results have practical implications in the study of the transition to turbulence of wall bounded flows of unconventional fluids and in devising flow control strategies.

1
Introduction

1.1 Green power technologies in the global energy scenario

Worldwide urbanization and economic growth occurred at a continuously increasing rate in the last century and are expected to follow the same trend in the future. Consequently, global energy demand dramatically rose, e.g., it doubled since 1980[1], making energy provision one of the primary challenges our Society has to face. Nowadays, most of energy production comes from the use of fossil fuels, which accounts for 80% of the total[2], with coal playing a major role due to its easy accessibility and low cost. Despite regulations and limitations introduced by governments on the use of fossil fuels, they are expected to continue to play a large role in the future[2]. China represents a striking example of the large utilization of fossil fuels: its total fossil fuels electricity net generation rose from 230 TWh in 1980 to 3700 TWh in 2012, topping the United States in 2009[3].

It is well documented that the most serious threat posed by the use of fossil fuels is the emission of green house gases (GHG) to the atmosphere, which are responsible for climate change. The International Panel on Climate Change report[4] from last year affirms that the total anthropogenic GHG emissions steadily increased by 80% from 1970 to 2010. In these four decades, the CO_2 share of GHG emissions remained constant to about 75%. Economic and population growth are the main drivers for increasing levels of CO_2 emissions from fossil fuel combustion. While the contribution of population growth was roughly constant in the period 1970-2010, the contribution of economic growth considerably increased during 2000-2010.

One of the consequences of high CO_2 concentrations in the atmosphere is that it reduces the transmission of thermal radiation from the earth surface and low atmosphere, therefore warming the surface by the so-called greenhouse mechanism[5]. Consistent increase of the global mean earth surface temperature for over a century was observed and matched by numerical predictions of climate models up to 1975[6]. After a short period of time characterized by a temperature drop, a more rapid warming followed at a rate 0.2 °C per decade in the following four decades, reaching a total temperature increase of 0.8 °C in the post-industrial era[7–10]. Several studies demonstrated that the consequences of the surface mean temperature increase already affect our everyday life. Global warming is responsible for increasing sea levels[9,11] due to the ocean thermal expansion[12] and the melting from non-polar glaciers, with an increasing contribution of the ice sheet[13]. Convincing arguments were proposed for recent climate change being a primary agent of observed ecological changes, namely in the breeding and migration date, and geographical and breeding range of animals due to their sensitivity of habitat or food supply to altered temperatures and precipitations[7,14–18]. Increasing extreme climate events, although difficult to monitor and analyze on a global scale due to the lack of high-quality long-term climate data[19], may also be directly or partially attributed to global warming[4,20], as it is the case for the observed intensification of heavy precipitation events in the Northern Hemisphere land areas[21].

In order to draw possible pathways which could lead to a mitigation of global warming, the International Energy Agency published a report in 2012 whereby a so-called two-

degrees scenario was introduced. Several recommendations and guidelines were given in order to limit the global temperature increase with respect to pre-industrial era to 2 °C by 2050. Other studies also proposed policies and technological options to achieve the target of comply with the 2 °C maximum temperature rise, proposing to limit the CO_2 concentration levels in the atmosphere to the range 350-450 ppm[4,22] (nowadays the concentration is 400 ppm). This maximum CO_2 concentration threshold might be dangerously further reduced as a consequence of the feedback between the climate and the biosphere[23]. Delaying efforts to mitigate emissions will substantially decrease the range of options for reaching the two-degrees objective[4] and overshoot of CO_2 concentration could lead to irreversible catastrophic effects[22].

It is certainly evident that a drastic change in the energy policies must be undertaken now in order to significantly reduce or divest from fossil fuels usage. Strategic decisions are to be made by governments in order to promote the role of renewable energy conversion alternatives which are CO_2-neutral. Decentralized production, integrated systems and smart grids are key elements for a sustainable future. Significant steps in the direction of green energy have been made by several countries, with Germany being at the forefront with its energy transition plan, the Energiewende[24], which aims at replacing nuclear and most of fossil energy with renewables by 2050. In 2005, the share of the country total electricity generation hold by renewables amounted to 8%, it increased to 25% in 2015 and is planned to reach around 87% by 2050. The process undergoing in Germany does not only include a switch to new technologies, but involves lower energy consumption through efficiency and conservation, and an energy usage based on the availability. Long-term policies adopted in Germany in the last decades made possible a reduction of the GHG emissions by -22% despite an increase in the gross domestic product of 28% in the period 1991-2012. These policies also created more than 380,000 jobs, reduced the country dependence on the imports of fossil fuels, and helped developing the most important green technology sector worldwide.

Among the alternatives for sustainable energy conversion, the new generation of power systems based on innovative thermodynamic cycles, having the working fluid operating in the sub- and supercritical thermodynamic region is an attractive option. Organic Rankine cycle (ORC) and supercritical CO_2 (sCO_2) Brayton cycle turbogenerators are widely recognized as power systems which are particularly suited to exploit renewable energy sources such as solar radiation, waste heat from industrial processes and engines, and geothermal reservoirs.

In the last two decades, ORC power systems became the technology of choice for the conversion of renewable or renewable-equivalent energy sources in the low power output range, from few kW_e to few MW_e. The working principle of the thermodynamic cycle is the same as for a steam Rankine cycle. However, the working fluid is an organic compound, which can be chosen or designed in order to best match the external energy source/sink, thus making the technology extremely flexible. High conversion efficiency, low cost, and compact assembly make ORC power plants attractive. For more information on the history, characteristics and perspective on this technology the reader is referred to the recent review paper by Colonna *et al.*[25].

The idea of using sCO_2 as the working fluid of a Brayton cycle power plant was first

proposed in the 60's by Angelino[26] and Feher[27], who highlighted as one of its key features the very high thermodynamic efficiency, up to 50%, reachable at moderate turbine inlet temperatures if compared to competing technologies, e.g., the well established steam power plant. Moreover, sCO_2 power systems are very compact due to the large operating density and pressure of the working fluid. Despite the working principles being introduced long ago, only in the last decade the scientific community and companies have been undertaking the needed research and development in order to bring the technology to the market. Studies of the application to next-generation nuclear reactors[28,29], concentrated solar power plants[30–33] and waste heat recovery[34,35] have been documented in the literature. An example of the wide interest in this technology is the SunShot Initiative which was sponsored by the U.S. Department of Energy in 2012 with a budget contribution of 8 million USD in order to build a 10 MW concentrated solar power plant in which the power block is a sCO_2 turbogenerator[36].

One of the most challenging aspects of devising competitive ORC or sCO_2 turbogenerators is the fluid dynamic design of efficient turbomachinery components, namely the compressor and turbine. The fluid thermophysical properties exhibit strong non-linearities in the thermodynamic region in which the expansions and compression processes occur, namely close to the fluid vapour-liquid critical point. This makes the fluid dynamics peculiar and substantially different from the case of fluids used in standard power cycle technologies, such as steam and air, which comply with the ideal gas model. The lack of experience, experimental data and knowledge on the physical behaviour of fluids in the sub- and supercritical thermodynamic region is arguably the main limitation in the design of efficient machines, which still nowadays often relies on simplified models or on design strategies developed for air or steam compressors or turbines. Computational fluid dynamics (CFD) is a powerful tool to investigate fundamental aspects of non-ideal fluid flow behaviour as well as to assist the components design. By predicting fluid flow through the machine it allows to optimize the turbomachinery efficiency and limit the number of experiments and prototypes, thereby reducing the project cost. Despite the numerous advancements in the field of CFD for ideal fluids, only recently non-ideal fluid flows received the attention of the scientific community, as demonstrated by the scarce available literature on both the numerical aspects of the simulations[37–42] and on the study of specific applications[43–50].

This thesis presents original research in the field of fluid dynamics of non-ideal fluids and documents the study of the problem with three different but complementary approaches, namely the numerical, applicative, and analytical investigation. The aim of this work is therefore threefold and consists of:

- developing new numerical schemes for the accurate and efficient CFD simulation of non-ideal compressible flows;
- studying with the developed CFD tools turbomachinery problems relevant for ORC and sCO_2 applications which were never investigated before;
- analyzing the hydrodynamic stability of non-ideal fluid flows using analytical tools.

1.2 Thesis outline

The material included was partly presented at international conferences and/or appeared in peer-reviewed international scientific journals. The thesis is organized in five self-contained chapters, each addressing a specific problem, which can be subdivided according to their specific aim into three parts, i) numerical methods, ii) applications, and iii) analytical study. The final Chapter summarizes the conclusions and proposes future steps for research in this field.

Numerical methods

The main achievement of this study is the development of a comprehensive methodology to simulate turbomachinery flows of compressible non-ideal fluids in the framework of the finite-volume discretization of the Navier–Stokes equations.

Chapter 2 documents the exact derivation of Jacobian matrices for several numerical schemes for the approximation of convective and diffusive fluxes, in order to account for a generic equation of state model of the fluid. The use of look-up table interpolation of fluid properties is analyzed and proposed as alternative to the direct solution of the equation of state model. The accuracy and convergence of the newly introduced schemes are verified on a series of one and two-dimensional test cases, and assessed against analytical solutions when available. It is demonstrated that the best convergence is obtained with a consistent discretization of the right-hand-side and left-hand-side of the equations, i.e., by using the same scheme to evaluate the flux and the Jacobian part.

Chapter 3 presents a new flux-conserving treatment of non-conformal mesh blocks interfaces. The method uses a local auxiliary mesh to establish connectivity between the non-conformal blocks and is conservative by construction, avoiding any flux interpolation and without enforcing additional constraints. The Chapter discusses the details of the auxiliary mesh generation and its parallelization, and of the flux calculation at the interface. The accuracy of the gradient reconstruction at the interface, needed in high order and viscous simulations, is also investigated analytically and numerically. Numerical stability is verified empirically by solving the equations using both explicit and implicit time integration schemes. Applications to two- and three-dimensional fluid dynamic problems verify the method for stationary non-conformal mesh blocks simulations as well for simulations whereby mesh blocks are in relative motion.

Applications

The numerical methodology developed in the first part is applied here to study challenging turbomachinery problems, providing new insights on the peculiarities of the fluid dynamic operation of non-conventional machines compressing or expanding the fluid in the proximity of its vapour-liquid critical point.

Chapter 4 reports the numerical prediction of the performance map of a radial compressor operating with sCO_2 by means of steady state RANS simulations. The considered compressor (50 kW, 20 mm diameter, 75 krpm design rotational speed) is part of

a 250 kW sCO_2 turbogenerator prototype designed, realized, and operated for demonstration purposes at the Sandia National Laboratories (SNL) site in Albuquerque, New Mexico.

The highest possible accuracy in the fluid properties description is achieved using look-up tables generated with a multiparameter equation of state model. Numerical results are compared to experiments and their agreement validates the developed CFD methodology. A detailed flow analysis shows that conditions for local fluid condensation might be met at the leading edge of the compressor main-blade and that the extent of these regions grows with the rotational speed. The occurrence of condensation is relevant to efficiency and stability of operation.

Chapter 5 investigates the stator/rotor interaction in a highly supersonic ORC turbine (60-170 kW, 26 krpm design rotational speed, pressure ratio > 100, maximum vane Mach number $M \approx 3$). Unsteady RANS simulations are performed to highlight the main flow characteristics and to study the interaction between shock waves and viscous wakes. Blade loads are calculated and analyzed in the time and frequency domain. Their temporal fluctuation is found to be of the same order of magnitude of the static loads, therefore demonstrating the importance of performing unsteady simulation in the design process of non-conventional supersonic turbomachines. The most important fluid dynamic mechanisms are described and related to the blade load trends, providing unique insights which might be used along with modern shape optimization techniques to improve the turbine performance.

Analytical tools

The classic modal and non-modal stability theory developed in the last two decades for a constant property flow is extended in order to study more realistic fluid flows with variable transport properties. The flow transition from a laminar to a turbulent state strongly influences parameters such as the skin friction and heat transfer properties. Thus, its understanding and modeling is of paramount importance for a number of engineering applications, e.g., in turbomachines or heat exchangers.

Chapter 6 focuses on the effect of temperature dependent thermal conductivity and specific heat on the maximum growth of perturbations in a thermally stratified laminar channel flow. Two different reference temperature profiles are considered, namely a linear and a parabolic profile. The influence of variable properties is assessed in two steps, first by looking at the individual effects, and subsequently by considering the coupled variation of thermal conductivity and specific heat. A parametric study of the influence of the property profiles and of the Prandtl number shows that substantial maximum energy growth amplification/reduction can be achieved with respect to a constant property case, therefore promoting or delaying the transition of the flow from a laminar to a turbulent state. The time needed by the flow to reach the maximum growth of the perturbations is also studied under variable properties, and shows that the growth mechanism can be either speeded-up or slowed-down, depending on the Prandtl number.

References

[1] International Energy Agency, 2012. Energy technology perspectives 2012. Tech. rep.

[2] Massachusetts Institute of Technology, 2007. The future of coal. Tech. rep.

[3] U.S. Energy Information Administration, 2015. International Energy Statistics. website: www.iea.gov.

[4] International Panel on Climate Change, 2014. Climate change 2014, fifth assessment report. Tech. rep.

[5] Wang, W., Yung, Y., Lacis, A., Mo, T., and Hansen, J., 1976. "Greenhouse effects due to man made perturbations of trace gases. anthropogenic gases may alter our climate by plugging an atmospheric window for escaping thermal radiation". *Science,* **194**(4266), pp. 685–690.

[6] Hansen, J., 1981. "Climate impact of increasing atmospheric carbon dioxide.". *Science,* **213**(4511), pp. 957–966.

[7] Root, T., Price, J., Hall, K., Schneider, S., Rosenzweig, C., and Pounds, J., 2003. "Fingerprints of global warming on wild animals and plants". *Nature,* **421**(6918), pp. 57–60.

[8] Hansen, J., Sato, M., Ruedy, R., Lo, K., Lea, D., and Medina-Elizade, M., 2006. "Global temperature change". *Proc. Natl. Acad. Sci. U. S. A.,* **103**(39), pp. 14288–14293.

[9] Rahmstorf, S., Cazenave, A., Church, J., Hansen, J., Keeling, R., Parker, D., and Somerville, R., 2007. "Recent climate observations compared to projections". *Science,* **316**(5825), p. 709.

[10] Hansen, J., Ruedy, R., Sato, M., and Lo, K., 2010. "Global surface temperature change". *Rev. Geophys.,* **48**(4), pp. 1–29.

[11] Hansen, J., Nazarenko, L., Ruedy, R., Sato, M., Willis, J., Del Genio, A., Koch, D., Lacis, A., Lo, K., Menon, S., Novakov, T., Perlwitz, J., Russell, G., Schmidt, G., and Tausnev, N., 2005. "Climate change: Earth's energy imbalance: Confirmation and implications". *Science,* **308**(5727), pp. 1431–1435.

[12] Willis, J., Roemmich, D., and Cornuelle, B., 2004. "Interannual variability in upper ocean heat content, temperature, and thermosteric expansion on global scales". *J. Geophys. Res.-Oceans,* **109**(12), pp. 1–13.

[13] Cazenave, A., 2006. "Atmosphere: How fast are the ice sheets melting?". *Science,* **314**(5803), pp. 1250–1252.

[14] Hughes, L., 2000. "Biological consequences of global warming: Is the signal already apparent?". *Trends Ecol. Evol.,* **15**(2), pp. 56–61.

[15] Wuethrich, B., 2000. "How climate change alters rhythms of the wild". *Science,* **287**(5454), pp. 793–795.

[16] McCarty, J., 2001. "Ecological consequences of recent climate change [consecuencias biolgicas de cambios climticos recientes]". *Conserv. Biol.,* **15**(2), pp. 320–331.

[17] Walther, G.-R., Post, E., Convey, P., Menzel, A., Parmesan, C., Beebee, T., Fromentin, J.-M., Hoegh-Guldberg, O., and Bairlein, F., 2002. "Ecological responses to recent climate change". *Nature,* **416**(6879), pp. 389–395.

[18] Parmesan, C., and Yohe, G., 2003. "A globally coherent fingerprint of climate change impacts across natural systems". *Nature,* **421**(6918), pp. 37–42.

[19] Easterling, D., Evans, J., Groisman, P., Karl, T., Kunkel, K., and Ambenje, P., 2000. "Observed variability and trends in extreme climate events: A brief review". *Bull. Amer. Meteor. Soc.,* **81**(3), pp. 417–425.

[20] Menon, S., Hansen, J., Nazarenko, L., and Luo, Y., 2002. "Climate effects of black carbon aerosols in china and india". *Science,* **297**(5590), pp. 2250–2253.

[21] Min, S.-K., Zhang, X., Zwiers, F., and Hegerl, G., 2011. "Human contribution to more-intense precipitation extremes". *Nature,* **470**(7334), pp. 378–381.

[22] Hansen, J., Sato, M., Kharecha, P., Beerling, D., Berner, R., Masson-Delmotte, V., Pagani, M., Raymo, M., Royer, D. L., and Zachos, J. C., 2008. "Target atmospheric CO_2: Where should humanity aim?". *arXiv preprint arXiv:0804.1126*.

[23] Cox, P., Betts, R., Jones, C., Spall, S., and Totterdell, I., 2000. "Acceleration of global warming due to carbon-cycle feedbacks in a coupled climate model". *Nature,* **408**(6809), pp. 184–187.

[24] http://energytransition.de/. Energy Transition. The German Energiewende.

[25] Colonna, P., Casati, E., Trapp, C., Mathijssen, T., Larjola, J., Turunen-Saaresti, T., and Uusitalo, A., 2015. "Organic Rankine cycle power systems: From the concept to current technology, applications, and an outlook to the future". *J. Eng. Gas Turb. Power,* **137**(10), p. 100801.

[26] Angelino, G., 1968. "Carbon dioxide condensation cycles for power production". *ASME J. Eng. Power,* **10**, July, pp. 287–295.

[27] Feher, E. G., 1968. "The supercritical thermodynamic power cycle". *Ennerg. Convers.,* **8**, pp. 85–90.

[28] Dostal, V., Hejzlar, P., and Driscoll, M. J., 2006. "High-performance supercritical carbon dioxide cycle for next-generation nuclear reactors". *Nucl. Technol.,* **154**(3), pp. 265–282.

[29] Dostal, V., Hejzlar, P., and Driscoll, M. J., 2006. "The supercritical carbon dioxide power cycle: Comparison to other advanced power cycles". *Nucl. Technol.,* **154**(3), pp. 283–301.

[30] Kim, Y. M., Kim, C. G., and Favrat, D., 2012. "Transcritical or supercritical CO_2 cycles using both low- and high-temperature heat sources". *Energy,* **43**(1), pp. 402–415.

[31] Turchi, C. S., Ma, Z., Neises, T. W., and Wagner, M. J., 2013. "Thermodynamic study of advanced supercritical carbon dioxide power cycles for concentrating solar power systems". *ASME J. Sol. Energ.,* **135**(4), p. 041007.

[32] Garg, P., Kumar, P., and Srinivasan, K., 2013. "Supercritical carbon dioxide Brayton cycle for concentrated solar power". *J. Supercrit. Fluid.,* **76**, pp. 54–60.

[33] Iverson, B. D., Conboy, T. M., Pasch, J. J., and Kruizenga, A. M., 2013. "Supercritical CO_2 Brayton cycles for solar-thermal energy". *Appl. Energ.,* **111**, pp. 957–970.

[34] Chen, Y., Lundqvist, P., and Platell, P., 2005. "Theoretical research of carbon dioxide power cycle application in automobile industry to reduce vehicle's fuel consumption". *Appl. Therm. Eng.,* **25**(14-15), pp. 2041–2053.

[35] Chen, Y., Lundqvist, P., Johansson, A., and Platell, P., 2006. "A comparative study of the carbon dioxide transcritical power cycle compared with an organic Rrankine cycle with R123 as working fluid in waste heat recovery". *Appl. Therm. Eng.,* **26**(17-18), pp. 2142–2147.

[36] http://energy.gov/eere/sunshot/project-profile-10-megawatt-supercritical-carbon-dioxide-turbine.

[37] Colonna, P., and Rebay, S., 2004. "Numerical simulation of dense gas flows on unstructured grids with an implicit high resolution upwind Euler solver". *Int. J. Numer. Meth. Fl.,* **46**(7), pp. 735–765.

[38] Cinnella, P., and Congedo, P., 2005. "Numerical solver for dense gas flows". *AIAA J.,* **43**(11), Nov., pp. 2457–2461.

[39] Cirri, M., Adami, P., and Martelli, F., 2005. "Development of a CFD real gas flow solver for hybrid grid". *Int. J. Numer. Meth. Fl.,* **47**(8-9), pp. 931–938.

[40] Cinnella, P., 2006. "Roe-type schemes for dense gas flow computations". *Comput. Fluids,* **35**(10), pp. 1264–1281.

[41] Congedo, P. M., Corre, C., and Cinnella, P., 2011. "Numerical investigation of dense-gas effects in turbomachinery". *Comput. Fluids,* **49**(1), pp. 290–301.

[42] Urbano, A., and Nasuti, F., 2013. "An approximate Riemann solver for real gas parabolized Navier–Stokes equations". *J. Comput. Phys.,* **233**, pp. 574–591.

[43] Colonna, P., Harinck, J., Rebay, S., and Guardone, A., 2008. "Real-gas effects in organic Rankine cycle turbine nozzles". *J. Propul. Power,* **24**(2), pp. 282–294.

[44] Harinck, J., Guardone, A., and Colonna, P., 2009. "The influence of molecular complexity on expanding flows of ideal and dense gases". *Phys. Fluids,* **21**(8), p. 086101.

[45] Harinck, J., Colonna, P., Guardone, A., and Rebay, S., 2010. "Influence of thermodynamic models in two-dimensional flow simulations of turboexpanders". *J. Turbomach.,* **132**(1), pp. 1–17.

[46] Harinck, J., Turunen-Saaresti, T., Colonna, P., Rebay, S., and van Buijtenen, J., 2010. "Computational study of a high-expansion ratio radial organic Rankine cycle turbine stator". *J. Eng. Gas Turb. Power,* **132**(5), p. 054501.

[47] Harinck, J., Pasquale, D., Pecnik, R., van Buijtenen, J., and Colonna, P., 2013. "Performance improvement of a radial organic Rankine cycle turbine by means of automated computational fluid dynamic design". *Proc. IMechE, Part A: J. Power and Energy,* **227**(6), pp. 637–645.

[48] Pasquale, D., Ghidoni, A., and Rebay, S., 2013. "Shape optimization of an organic Rankine cycle radial turbine nozzle". *J. Eng. Gas Turb. Power,* **135**(4), pp. 042308–1.

[49] Wheeler, A. P. S., and Ong, J., 2013. "The role of dense gas dynamics on organic Rankine cycle turbine performance". *J. Eng. Gas Turb. Power,* **135**(10), p. 102603.

[50] Sauret, E., and Gu, Y., 2014. "Three-dimensional off-design numerical analysis of an organic Rankine cycle radial-inflow turbine". *Appl. Energ.,* **135**, pp. 202–211.

2

Exact Jacobians for implicit Navier–Stokes simulations of equilibrium real gas flows

The contents of this chapter appeared in:

Rinaldi, E., Pecnik, R., and Colonna, P., 2014. *J. Comput. Phys.*, **270**, pp. 459–477.

Abstract *This paper documents the extension of several widespread flux schemes, used in finite-volume Navier–Stokes solvers, for the simulation of flows whose fluid properties must be estimated with complex thermophysical models. Exact Jacobian matrices for the convective fluxes are derived with no assumption on the fluid equations of state model for Liou's AUSM$^+$, Toro* et al.*'s HLLC, and Kurganov and Tadmor's central scheme. The Jacobians of the diffusive fluxes are expressed using the formulation proposed by Pulliam and Steger, resulting in additional terms due to the viscosity and thermal conductivity variations. An efficient look-up table approach is thoroughly studied and proposed as an alternative to the direct solution of the equation of state model for the fluid thermophysical property evaluation. The newly introduced schemes are validated and tested in terms of accuracy and convergence rate on a series of one and two-dimensional test cases. The results indicate that the Jacobian must be based on the same flux formulation as the one used on the right-hand side of the implicit equation to achieve numerically converged solutions.*

2.1 Introduction

Nowadays, computational fluid dynamics (CFD) is a widely used tool for the analysis and design of many engineering applications, as well as for the study of the physics of complex flows. Most of the numerical techniques applicable to compressible flows developed throughout the years have been derived under the assumption that the fluid complies with the ideal gas model. However, several assumptions (e.g., constant specific heats, ideal gas law) do not hold if a fluid state is close to its vapor-liquid critical point (dense gas region) or at high temperatures and low pressures. There is a wide variety of flows for which real gas effects are predominant and must be considered, some of them being hypersonic flows, reacting flows, and supercritical flows.

The main focus of this paper is on fluid non-ideality in the dense gas region. Throughout the paper the fluid is assumed to be in single phase. However, the methods proposed here can be applied to model two-phase vapor-liquid flows when the assumption of homogeneous mixture can be made, see for example Refs.[1,2]. The interest in dense gasdynamics is motivated by the application to energy conversion systems, e.g. organic Rankine cycle turbines (see Ref.[3] for a recent review), and by the peculiar gasdynamic behaviour of fluids in such thermodynamic region, whereby non-classical phenomena may occur for molecularly complex compounds[4,5].

A number of theoretical studies on dense gas flows were conducted in the last few decades. Some examples are the study of propagation of waves showing classical and non-classical characteristics[6], of compressible internal flows with heat addition[7,8], of inviscid flows in cascade configurations[9], in shock tubes[10,11], in nozzles[12], and around airfoils[13,14]. Recently, applications to turbomachinery were investigated by several authors[15–19].

The topic of adapting standard numerical techniques to be applicable for real gas simulations using the finite-volume Godunov method[20] has been proposed in the 80's by several authors. Colella and Glaz[21] were among the first to study the numerical solution

of the Riemann problem of gasdynamics for a real fluid. The extension of the Roe's approximate Riemann solver[22] and of some variants of the original scheme, with the aim of including complex equations of state, was considered by Glaister[23–26], Montagné and co-workers[27,28], and Gallouët and co-workers[29,30]. Guardone and Vigevano[31] generalized Roe's linearization to the case of a van der Waals gas, and Mottura *et al.*[32] to a high temperature reacting flow. Further contributions are the ones of Colonna and Rebay [33], Cinnella and Congedo[34,35], and Cirri *et al.*[36]. Other splitting schemes such as the Steger–Warming's[37], van Leer's[38], Osher's[39], and Liou's AUSM$^+$[40] were considered by Liou *et al.*[41], Suresh and Liou[42], and Edwards and co-workers[43,44]. Central difference schemes were studied by Saurel *et al.*[45] and later by Merkel *et al.*[46].

The aim of this paper is to provide a complete methodology for incorporating complex thermophysical models in several well established inviscid and viscous flux schemes for the Navier–Stokes equations. The inviscid flux schemes considered are the AUSM$^+$ scheme introduced by Liou[40], the HLLC scheme of Toro *et al.*[47], and the central scheme of Kurganov and Tadmor (KT)[48]. No assumption on the equation of state model is assumed. The description of the Roe solver is included for the purpose of comparison and its implementation is taken from Colonna and Rebay[33]. The diffusive fluxes and their implicit formulation are discretized following Pulliam and Steger[49]. Additional terms in the Jacobian caused by temperature-dependent viscosity and thermal conductivity are highlighted and discussed. Furthermore, a look-up table (LUT) interpolation is proposed and comprehensively evaluated. A detailed assessment of the LUT accuracy, consistency, and computational efficiency with respect to direct solution of the equation of state model is given to provide a solid basis for its use.

The paper is structured as follows. Sec. 2.2 describes the analysis of the LUT interpolation method and the evaluation of its performance compared to the direct calculation of fluid properties using EoS models. The formulation of the convective and diffusive numerical fluxes and the expression of the Jacobians for both is provided in Sec. 2.3 and 2.4. A series of one and two-dimensional test cases is presented in Sec. 5.4 and convergence histories are also reported. Finally, conclusions are drawn in Sec. 3.7. The appendices give the generic expressions of the pressure derivatives needed for the fluxes and the Jacobians (A.1), and the strategy adopted to obtain the exact solution of the Riemann problem of gasdynamics for a real gas (A.2).

2.2 Look-up tables for fluid property evaluations

The main limitation of CFD simulations for the analysis of fluids governed by complex thermodynamics is the computational effort required for their thermophysical property evaluation. This issue can be the bottle-neck of the use of real gas flow simulations within the framework of uncertainty quantification or numerical optimization. If real gas equations of state models are adopted, various levels of approximation are possible, whereby high accuracy implies large computational cost. In order to reduce the latter an approximate property evaluation must be considered instead of a direct solution of the equation of state. A LUT interpolation provides the best features in terms of efficiency, simplic-

ity, and flexibility. A grid is generated over a range for two independent thermodynamic variables (e.g., temperature and density), and all the thermophysical properties of interest are stored in its nodes. The table can be accessed specifying any pair of properties, and the cell identification can be easily done with standard search algorithms. If the tabulated region encompasses the vapor-liquid equilibrium (VLE) region, we split the grid into two sub-grids, one for the single phase and one for the VLE region. This is done because of the discontinuity across the saturation lines of thermophysical properties such as pressure derivatives and the speed of sound. The accuracy, consistency, and computational cost of table interpolation are analyzed in the following sections.

2.2.1 Accuracy

The comparison of the results of three table interpolation schemes is described hereafter, namely the bilinear, the 3$^{\text{rd}}$ order Lagrange polynomial, and the least-squares gradient interpolation schemes. The accuracy of the property interpolation is assessed in the supercritical region of carbon dioxide CO_2 (similar results can be obtained with different fluids), where several thermophysical properties show a nonlinear behavior, e.g. density, specific heats, thermal conductivity, and viscosity. Interpolated values for 40,000 random input states are compared with the values obtained from the solution of the thermodynamic model, namely the multiparameter EoS for technical applications of Span and Wagner type[50–52]. The thermodynamic model is expressed in terms of the reduced Helmholtz free energy as a function of the reduced density and of the inverse of the reduced temperature. The model parameters (12 in total) are optimized fitting a large set of high accuracy experimental data. The average relative interpolation error is shown in Fig. 2.1 as a function of the number of discretization nodes for the single edge of the table. The convergence rate for the three schemes is not affected by the different choice of input variables. As expected, the polynomial interpolation shows the best accuracy and convergence. Similar results and trends are obtained if values calculated in other thermodynamic regions are compared. It is worth mentioning that a limited number of discretization nodes (around 100 for each dimension in the presented case) leads to a level of accuracy acceptable for many practical applications.

2.2.2 Consistency

If the direct solution of the thermodynamic model is replaced by property interpolation, the consistency of the approximate state with an EoS is of primary concern. The numerical study of this aspect is illustrated in this section with a focus on the evaluation of the speed of sound, which can be expressed as

$$c = \sqrt{\frac{\partial \Pi}{\partial \rho} + \left(h^{\mathrm{t}} - \|\mathbf{v}\|^2\right) \frac{\partial \Pi}{\partial E^{\mathrm{t}}}}\,, \tag{2.1}$$

where $\Pi = \Pi(\rho, \mathbf{m}, E^{\mathrm{t}})$ is the pressure as a function of density ρ, momentum $\mathbf{m} = \rho\mathbf{v}$, and total energy $E^{\mathrm{t}} = \rho\left(e + \frac{1}{2}\|\mathbf{m}\|^2/\rho^2\right)$. The analytic expression of the pressure derivatives

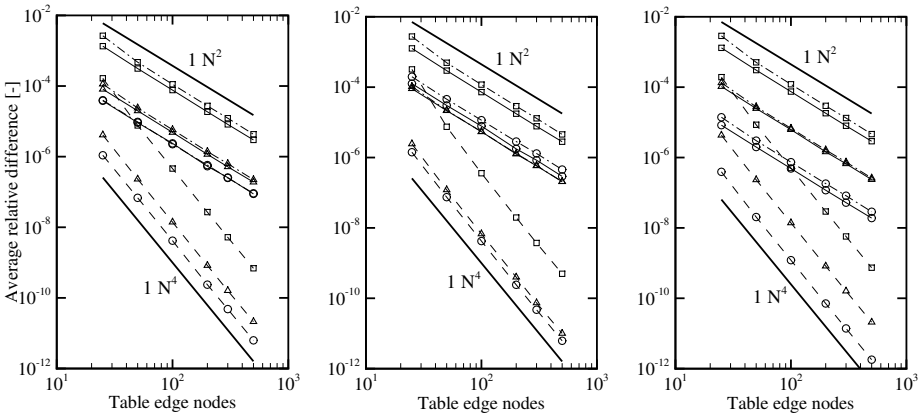

(a) P, ρ. (b) ρ, e. (c) ρ, T.

Figure 2.1: Average interpolation error using different input variables for bilinear (—), least-squares gradient (-·-) and 3rd order Lagrange polynomial interpolation (- - -) schemes. Different symbols correspond to speed of sound (△), isobaric specific heat capacity (□) and pressure (center) or specific internal energy (left and right) (○). The tabulated region is $\rho = [200, 600]\,\mathrm{kg/m^3}$ and $T = [308, 500]\,\mathrm{K}$. 40,000 random input states are computed.

is provided in A.1. The derivatives can be tabulated at the nodes and then interpolated (method A), or calculated based on the interpolated values of the pressure (method B), e.g., using finite differences. Another possibility is to directly interpolate the speed of sound (method C). Fig. 2.2 shows the differences for the speed of sound between the methods A and C, and B and C for the same thermodynamic region as in Sec. 2.2.1, and the same number of samples. If the pressure derivatives are interpolated (method A), the difference converges one order faster as compared to method B. It can be inferred from Fig. 2.2 that the inconsistency due to these different approaches can be considered negligible in most practical applications, even if a relatively small number of discretization points is selected.

2.2.3 Computational cost

The implementation of the LUT method can be effectively optimized in order to reduce the number of operations needed for each property evaluation. In this respect, the compact barycentric form of the Lagrange polynomials[53] was used in this work. Furthermore, all the geometrical coefficients needed for the least-squares gradient reconstruction were computed in a pre-processing step. Two thermodynamic models were compared with the LUT approach, namely the improved Stryjek–Vera modified Peng–Robinson cubic EoS

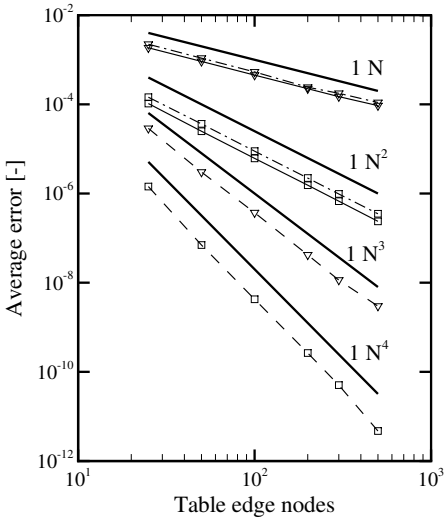

Figure 2.2: Numerical error in the evaluation of the speed of sound for bilinear (—), least-squares gradient (-··-) and 3rd order Lagrange polynomial interpolation (- - -) schemes. The pressure derivatives of Eq. (2.1) are either interpolated from the table (□) or computed using central finite differences of the interpolated pressure (▽). The reference value is directly interpolated from the tabulated speed of sound data. 40,000 random input variables are considered on the tabulated region $\rho = [200, 600]\,\mathrm{kg/m^3}$ and $T = [308, 500]\,\mathrm{K}$.

(iPRSV)[54], and the Span–Wagner multiparameter EoS for technical applications[52]. To perform the analysis of the computational cost, a function which calculates 15 primary and secondary thermophysical properties, commonly used in CFD solvers, was implemented for both thermodynamic models and for the three table interpolation schemes. The thermodynamic state of the fluid is specified by setting ρ and e, which is the typical combination of input variables used in a finite volume scheme to calculate the thermodynamic state after the solution is advanced in time. For a given thermodynamic model, and for a given implementation, the cost of the direct solution of the thermodynamic model largely depends on the choice of the specified state variables and on their thermodynamic region. Fig. 2.3 shows the average computational cost of the two EoS's for input states in the supercritical and VLE region of CO_2 (this is interesting for the applications in which the homogeneous mixture assumption can be adopted[1,2]). The computational cost of the table interpolation is also reported, and shows a reduction of up to 4 orders of magnitude when compared to the direct solution of the thermodynamic model. Furthermore, the computational cost of the table approach does not depend on the thermodynamic region, as seen for the direct EOS model evaluations. The computational cost reduction can be even larger if more complex EOS models are considered for the comparison, e.g., a

reference equation of state as the one presented in Ref.[55]. A further advantage of look-up tables is that any secondary property can be evaluated very efficiently. For example, the computation of derivatives can be avoided for the evaluation of secondary properties, e.g., speed of sound, fundamental derivative of gasdynamics Γ[4], which can be directly interpolated.

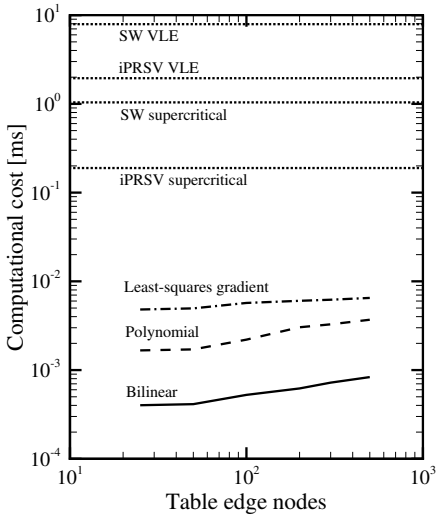

Figure 2.3: The computational cost of the direct solution of the thermodynamic model and table interpolation is assessed with 2.5M random calls to a function which evaluates 15 primary and secondary thermophysical properties commonly used in CFD simulations. The thermodynamic models based on the Span–Wagner type multiparameter EoS for technical applications[52] and cubic iPRSV EoS[54] are considered for the comparison using (ρ, e) as the input state, in the supercritical and VLE region of CO_2.

2.3 Approximate Riemann solver fluxes and Jacobians for an equilibrium real gas

An extension of several widespread convective flux evaluation schemes and their Jacobians is presented in this section to account for an equilibrium real gas thermodynamic model. Analytical implicit formulations are provided for the AUSM$^+$[40], HLLC[47], and Kurganov and Tadmor[48] schemes (the variables at the cell faces are considered independent of the speed of sound) and an approximate derivation of the Jacobian is given for the Roe solver[22].

Hereafter, the analytical convective (Euler) fluxes and Jacobian matrix will be referred to as $\mathbf{F}_{\text{con}}$ and A_{con}, as

$$\mathbf{F}_{\text{con}}(\mathbf{U}) = \begin{pmatrix} \mathbf{m}\cdot\mathbf{n} \\ (\rho u)q_n + \Pi(\mathbf{U})n_x \\ (\rho v)q_n + \Pi(\mathbf{U})n_y \\ (\rho w)q_n + \Pi(\mathbf{U})n_z \\ \rho q_n h^{\text{t}} \end{pmatrix}, \quad \text{and} \quad A_{\text{con}}(\mathbf{U}) = \frac{\partial \mathbf{F}_{\text{con}}(\mathbf{U})}{\partial \mathbf{U}}, \tag{2.2}$$

where $\mathbf{m} = (\rho u, \rho v, \rho w)^{\text{T}}$ denotes the linear momentum, $E^{\text{t}} = \rho\left(e + \frac{1}{2}\|\mathbf{v}\|^2\right)$ the total energy, $\mathbf{U} = (\rho, \mathbf{m}, E^{\text{t}})^{\text{T}}$ the conserved variables vector, $\Pi(\mathbf{U})$ the pressure, h^{t} the specific total enthalpy, $\mathbf{n} = \left(n_x, n_y, n_z\right)^{\text{T}}$ the surface normal unit vector, and $q_n = \mathbf{v}\cdot\mathbf{n}$ the covariant velocity.

2.3.1 Roe

The Roe scheme[22] is based on the definition of an average state $\mathbf{U}^{\text{Roe}}$. While the expressions for $\rho^{\text{Roe}}, \mathbf{v}^{\text{Roe}}, h^{\text{tRoe}}$ for a real gas are identical to the ones for an ideal gas, the definition of an average speed of sound c^{Roe} requires average values for the partial derivatives of pressure with respect to density and internal energy, which are not uniquely defined for an equilibrium real gas[27,28]. The solution proposed by Vinokur and Montagné[28] is used to close the problem. The numerical convective fluxes for the Roe scheme can be expressed as

$$\mathbf{F}_{j+\frac{1}{2}}(\mathbf{U}_{\text{L}}, \mathbf{U}_{\text{R}}) = \frac{\mathbf{F}_{\text{con}}(\mathbf{U}_{\text{R}}) + \mathbf{F}_{\text{con}}(\mathbf{U}_{\text{L}})}{2} - \frac{1}{2}\sum_{k=1}^{5} |\lambda^k| w^k \mathbf{r}^k, \tag{2.3}$$

where λ^k is the k-th eigenvalue of the Euler Jacobian matrix, Eq. (2.2), $w^k = (L\Delta\mathbf{U})_k$ the k-th Riemann invariant, and $\mathbf{r}^k$ the k-th right eigenvector. The definition of the Riemann invariants and right and left eigenvectors for a real gas are taken from Colonna and Rebay[33]. The subscripts $_{\text{L}}$ and $_{\text{R}}$ denote the left and right states of the considered cell interface $j + \frac{1}{2}$, respectively.

Due to the complexity of an exact derivation of the second term in Eq. (2.3) for a real gas, an approximate Jacobian is adopted, namely

$$A_{\text{L,R}}(\mathbf{U}_{\text{L}}, \mathbf{U}_{\text{R}}) = \frac{1}{2}\left(A_{\text{con}_{\text{L,R}}} \pm |A^{\text{Roe}}_{\pm}|\right), \tag{2.4}$$

where $|A^{\text{Roe}}_{\pm}| = R\Lambda_{\pm}L$, with $\Lambda_{\pm}$ the diagonal matrices of the positive and negative eigenvalues. The matrices $L, R, \Lambda_{\pm}$ are evaluated using the Roe average state.

2.3.2 AUSM$^+$

The numerical flux for the Liou's approximate Riemann solver[40] can be expressed as a function of the conserved variables as

$$\mathbf{F}_{j+\frac{1}{2}}(\mathbf{U}_\mathrm{L},\mathbf{U}_\mathrm{R}) = a_{j+\frac{1}{2}}\left\{ m^+_{j+\frac{1}{2}}\mathbf{U}_\mathrm{L} + m^+_{j+\frac{1}{2}}\begin{pmatrix}0\\0\\0\\0\\\Pi_\mathrm{L}\end{pmatrix} + m^-_{j+\frac{1}{2}}\mathbf{U}_\mathrm{R} + m^-_{j+\frac{1}{2}}\begin{pmatrix}0\\0\\0\\0\\\Pi_\mathrm{R}\end{pmatrix}\right\} + p_{j+\frac{1}{2}}\begin{pmatrix}0\\n_x\\n_y\\n_z\\0\end{pmatrix}, \tag{2.5}$$

whereby the only difference with the original formulation is the substitution of $H^\mathrm{t} = E^\mathrm{t} + \Pi$. The common interface speed of sound is chosen as $a_{j+\frac{1}{2}} = \sqrt{c_\mathrm{L}c_\mathrm{R}}$. The other terms are defined as $m^\pm_{j+\frac{1}{2}} = \frac{1}{2}\left(m_{j+\frac{1}{2}} \pm |m_{j+\frac{1}{2}}|\right)$, $p_{j+\frac{1}{2}} = \mathcal{P}^+(M_\mathrm{L})\Pi_\mathrm{L} + \mathcal{P}^-(M_\mathrm{R})\Pi_\mathrm{R}$, and $m_{j+\frac{1}{2}} = \mathcal{M}^+(M_\mathrm{L}) + \mathcal{M}^-(M_\mathrm{R})$, with M being the Mach number. The split Mach numbers $\mathcal{M}^\pm$ and pressures $\mathcal{P}^\pm$ are

$$\mathcal{M}^\pm(M) = \begin{cases} \frac{1}{2}\left(M \pm |M|\right), & \text{if } |M| \geq 1, \\ \pm\frac{1}{4}(M \pm 1)^2\left(1 + 4\beta(M \mp 1)^2\right), & \text{otherwise,}\end{cases} \tag{2.6}$$

$$\mathcal{P}^\pm(M) = \begin{cases} \frac{1}{2}\left(1 \pm |M|/M\right), & \text{if } |M| \geq 1, \\ \frac{1}{4}(M \pm 1)^2(2 \mp M \pm 4\alpha M(M \mp 1)^2), & \text{otherwise,}\end{cases} \tag{2.7}$$

with $\alpha = 3/16$ and $\beta = 1/8$ as in the original paper[40].

Neglecting the dependence of the interface speed of sound on the conserved variables (frozen speed of sound), the complete Jacobian of the AUSM$^+$ flux can be written in the

compact form

$$A_{\mathrm{L,R}}(\mathbf{U}_\mathrm{L},\mathbf{U}_\mathrm{R}) = a_{j+\frac{1}{2}} \begin{pmatrix} \left(\frac{\partial m^+_{j+\frac{1}{2}}}{\partial \mathbf{U}_{\mathrm{L,R}}}\right)^\mathrm{T} \rho_\mathrm{L} + \left(\frac{\partial m^-_{j+\frac{1}{2}}}{\partial \mathbf{U}_{\mathrm{L,R}}}\right)^\mathrm{T} \rho_\mathrm{R} \\ \left(\frac{\partial m^+_{j+\frac{1}{2}}}{\partial \mathbf{U}_{\mathrm{L,R}}}\right)^\mathrm{T} (\rho u)_\mathrm{L} + \left(\frac{\partial m^-_{j+\frac{1}{2}}}{\partial \mathbf{U}_{\mathrm{L,R}}}\right)^\mathrm{T} (\rho u)_\mathrm{R} \\ \left(\frac{\partial m^+_{j+\frac{1}{2}}}{\partial \mathbf{U}_{\mathrm{L,R}}}\right)^\mathrm{T} (\rho v)_\mathrm{L} + \left(\frac{\partial m^-_{j+\frac{1}{2}}}{\partial \mathbf{U}_{\mathrm{L,R}}}\right)^\mathrm{T} (\rho v)_\mathrm{R} \\ \left(\frac{\partial m^+_{j+\frac{1}{2}}}{\partial \mathbf{U}_{\mathrm{L,R}}}\right)^\mathrm{T} (\rho w)_\mathrm{L} + \left(\frac{\partial m^-_{j+\frac{1}{2}}}{\partial \mathbf{U}_{\mathrm{L,R}}}\right)^\mathrm{T} (\rho w)_\mathrm{R} \\ \left(\frac{\partial m^+_{j+\frac{1}{2}}}{\partial \mathbf{U}_{\mathrm{L,R}}}\right)^\mathrm{T} ({E^\mathrm{t}}_\mathrm{L} + \Pi_\mathrm{L}) + m^{+,-}_{j+\frac{1}{2}} \Pi^\mathrm{T}_{\mathrm{L,R_U}} + \left(\frac{\partial m^-_{j+\frac{1}{2}}}{\partial \mathbf{U}_{\mathrm{L,R}}}\right)^\mathrm{T} ({E^\mathrm{t}}_\mathrm{R} + \Pi_\mathrm{R}) \end{pmatrix} + a_{j+\frac{1}{2}} m^{+,-}_{j+\frac{1}{2}} \mathbb{I} + \begin{pmatrix} \mathbf{0}^\mathrm{T} \\ \left(\frac{\partial p_{j+\frac{1}{2}}}{\partial \mathbf{U}_{\mathrm{L,R}}}\right)^\mathrm{T} n_x \\ \left(\frac{\partial p_{j+\frac{1}{2}}}{\partial \mathbf{U}_{\mathrm{L,R}}}\right)^\mathrm{T} n_y \\ \left(\frac{\partial p_{j+\frac{1}{2}}}{\partial \mathbf{U}_{\mathrm{L,R}}}\right)^\mathrm{T} n_z \\ \mathbf{0}^\mathrm{T} \end{pmatrix}, \quad (2.8)$$

where $\mathbb{I}$ represents the identity matrix and $\Pi_\mathbf{U} = \left(\Pi_\rho, \Pi_{\rho u}, \Pi_{\rho v}, \Pi_{\rho w}, \Pi_{E^\mathrm{t}}\right)^\mathrm{T}$ the gradient of the pressure with respect to the conserved variables. The subscripts indicate the partial derivatives. The expressions of the pressure derivatives for a generic equation of state are given in A.1. The partial derivatives in Eq. (2.8) are expressed as

$$\frac{\partial m_{j+\frac{1}{2}}}{\partial \mathbf{U}_\mathrm{L}} = \frac{\partial \mathcal{M}^+}{\partial \mathbf{U}_\mathrm{L}}, \quad (2.9)$$

$$\frac{\partial m_{j+\frac{1}{2}}}{\partial \mathbf{U}_\mathrm{R}} = \frac{\partial \mathcal{M}^-}{\partial \mathbf{U}_\mathrm{R}}, \quad (2.10)$$

$$\frac{\partial m^\pm_{j+\frac{1}{2}}}{\partial \mathbf{U}_\mathrm{L}} = \frac{1}{2} \frac{\partial m_{j+\frac{1}{2}}}{\partial \mathbf{U}_\mathrm{L}} \left(1 \pm \mathrm{sign}(m_{j+\frac{1}{2}})\right), \quad (2.11)$$

$$\frac{\partial m^\pm_{j+\frac{1}{2}}}{\partial \mathbf{U}_\mathrm{R}} = \frac{1}{2} \frac{\partial m_{j+\frac{1}{2}}}{\partial \mathbf{U}_\mathrm{R}} \left(1 \pm \mathrm{sign}(m_{j+\frac{1}{2}})\right), \quad (2.12)$$

$$\frac{\partial \mathcal{M}^\pm(M)}{\partial \mathbf{U}} = \begin{cases} \frac{1}{2}\left(1 \pm \mathrm{sign}(M)\right) M_\mathbf{U}, & \text{if } |M| \geq 1, \\ \pm\frac{1}{2}(M \pm 1)\left(1 + 8\beta M(M \mp 1)\right) M_\mathbf{U}, & \text{otherwise,} \end{cases} \quad (2.13)$$

$$\frac{\partial p_{j+\frac{1}{2}}}{\partial \mathbf{U}_\mathrm{L}} = \mathcal{P}^+ \Pi_{\mathrm{L}_\mathrm{U}} + \Pi_\mathrm{L} \frac{\partial \mathcal{P}^+}{\partial \mathbf{U}_\mathrm{L}}, \tag{2.14}$$

$$\frac{\partial p_{j+\frac{1}{2}}}{\partial \mathbf{U}_\mathrm{R}} = \mathcal{P}^- \Pi_{\mathrm{R}_\mathrm{U}} + \Pi_\mathrm{R} \frac{\partial \mathcal{P}^-}{\partial \mathbf{U}_\mathrm{R}}, \tag{2.15}$$

$$\frac{\partial \mathcal{P}^\pm}{\partial \mathbf{U}} = \begin{cases} 0, & \text{if } |M| \geq 1, \\ \pm\frac{1}{4}(M \pm 1)\left(\pm 3 - 3M + 4\alpha(5M^2 - 1)(M \mp 1)\right) M_\mathbf{U}, & \text{otherwise.} \end{cases} \tag{2.16}$$

The derivatives of the Mach number with respect to the conservative variables are

$$\frac{\partial M}{\partial \mathbf{U}} = \begin{pmatrix} -M/\rho \\ n_x/(\rho a_{j+\frac{1}{2}}) \\ n_y/(\rho a_{j+\frac{1}{2}}) \\ n_z/(\rho a_{j+\frac{1}{2}}) \\ 0 \end{pmatrix}. \tag{2.17}$$

2.3.3 HLLC

In Batten *et al.*[56], a thorough analysis and derivation of the implicit formulation for the HLLC scheme of Toro *et al.*[47] is presented, but limited to a fluid complying with the ideal gas assumption. In case of a real gas equation of state, several modifications need to be made. The average Roe state, used for the estimation of the wave speeds to decompose the solution, see[57,58], is calculated according to Vinokur and Montagné[28]. The numerical fluxes at each interface are expressed as

$$\mathbf{F}_{j+\frac{1}{2}}(\mathbf{U}_\mathrm{L}, \mathbf{U}_\mathrm{R}) = \begin{cases} \mathbf{F}_\mathrm{con}(\mathbf{U}_\mathrm{L}) & \text{if } S_L > 0, \\ \mathbf{F}^*_\mathrm{L} & \text{if } S_L \leq 0 < S_M, \\ \mathbf{F}^*_\mathrm{R} & \text{if } S_M \leq 0 \leq S_R, \\ \mathbf{F}_\mathrm{con}(\mathbf{U}_\mathrm{R}) & \text{if } S_R < 0. \end{cases} \tag{2.18}$$

The wave speeds $S_L = \min\left(\lambda_1(\mathbf{U}_\mathrm{L}), \lambda_1(\mathbf{U}^\mathrm{Roe})\right)$ and $S_R = \max\left(\lambda_5(\mathbf{U}_\mathrm{R}), \lambda_5(\mathbf{U}^\mathrm{Roe})\right)$ are taken from Einfeldt *et al.*[57], with $\lambda_{1,5} = q_n \mp c$. S_L and S_R are not differentiated in the derivation of the Jacobians, and are considered frozen hereafter. The intermediate wave speed S_M is defined in Batten *et al.*[58] as

$$S_M = \frac{\rho_\mathrm{R} q_{n_\mathrm{R}} (S_R - q_\mathrm{R}) - \rho_\mathrm{L} q_{n_\mathrm{L}} (S_L - q_{n_\mathrm{L}}) + p_\mathrm{L} - p_\mathrm{R}}{\rho_\mathrm{R} (S_R - q_{n_\mathrm{R}}) - \rho_\mathrm{L} (S_L - q_{n_\mathrm{L}})}. \tag{2.19}$$

For supersonic states, the interface flux is given by the convective flux $\mathbf{F}_{\text{con}}$ evaluated either in the left or right state. For intermediate conditions the following fluxes are defined

$$\mathbf{F}^*_{\text{L,R}} = \begin{pmatrix} \rho^*_{\text{L,R}} S_M \\ (\rho u)^*_{\text{L,R}} S_M + p^* n_x \\ (\rho v)^*_{\text{L,R}} S_M + p^* n_y \\ (\rho w)^*_{\text{L,R}} S_M + p^* n_z \\ \left(E^{t*}_{\text{L,R}} + p^*\right) S_M \end{pmatrix}, \tag{2.20}$$

with average states

$$\mathbf{U}^*_{\text{L,R}} = \begin{pmatrix} \rho^*_{\text{L,R}} \\ (\rho u)^*_{\text{L,R}} \\ (\rho v)^*_{\text{L,R}} \\ (\rho w)^*_{\text{L,R}} \\ E^{t*}_{\text{L,R}} \end{pmatrix} = \Omega_{\text{L,R}} \begin{pmatrix} \rho_{\text{L,R}} \left(S_{L,R} - q_{n_{\text{L,R}}}\right) \\ \left(S_{L,R} - q_{n_{\text{L,R}}}\right) (\rho u)_{\text{L,R}} + (p^* - p_{\text{L,R}}) n_x \\ \left(S_{L,R} - q_{n_{\text{L,R}}}\right) (\rho v)_{\text{L,R}} + (p^* - p_{\text{L,R}}) n_y \\ \left(S_{L,R} - q_{n_{\text{L,R}}}\right) (\rho w)_{\text{L,R}} + (p^* - p_{\text{L,R}}) n_z \\ \left(S_{L,R} - q_{n_{\text{L,R}}}\right) e_{\text{L,R}} - p_{\text{L,R}} q_{\text{L,R}} + p^* S_M \end{pmatrix}, \tag{2.21}$$

with

$$\Omega_{\text{L,R}} = \left(S_{L,R} - S_M\right)^{-1}, \tag{2.22}$$

and

$$p^* = \rho_{\text{L}} \left(q_{n_{\text{L}}} - S_L\right) \left(q_{n_{\text{L}}} - S_M\right) + p_{\text{L}} = \rho_{\text{R}} \left(q_{n_{\text{R}}} - S_R\right) \left(q_{n_{\text{R}}} - S_M\right) + p_{\text{R}}. \tag{2.23}$$

As reported in Ref.[56], the implicit formulation takes the form

$$A_{\text{L,R}}(\mathbf{U}_{\text{L}}, \mathbf{U}_{\text{R}}) = \begin{cases} A_{\text{L}} = A_{\text{con}}(\mathbf{U}_{\text{L}}), & A_{\text{R}} = 0, & \text{if } S_L > 0, \\ A_{\text{L}} = \frac{\partial \mathbf{F}^*_{\text{L}}}{\partial \mathbf{U}_{\text{L}}}, & A_{\text{R}} = \frac{\partial \mathbf{F}^*_{\text{L}}}{\partial \mathbf{U}_{\text{R}}}, & \text{if } S_L \leq 0 < S_M, \\ A_{\text{L}} = \frac{\partial \mathbf{F}^*_{\text{R}}}{\partial \mathbf{U}_{\text{L}}}, & A_{\text{R}} = \frac{\partial \mathbf{F}^*_{\text{R}}}{\partial \mathbf{U}_{\text{R}}}, & \text{if } S_M \leq 0 \leq S_R, \\ A_{\text{L}} = 0, & A_{\text{R}} = A_{\text{con}}(\mathbf{U}_{\text{R}}), & \text{if } S_R < 0. \end{cases} \tag{2.24}$$

The main difference between the proposed derivation and Ref.[56] is that the pressure derivatives maintain their generic expression, which is valid for any equation of state model.

$$\frac{\partial F^*_{\mathrm{L}}}{\partial \mathbf{U}_{\mathrm{L,R}}} = \begin{pmatrix} \left(\frac{\partial \rho^*_{\mathrm{L}}}{\partial \mathbf{U}_{\mathrm{L,R}}}\right)^{\mathrm{T}} S_M + \left(\frac{\partial S_M}{\partial \mathbf{U}_{\mathrm{L,R}}}\right)^{\mathrm{T}} \rho^*_{\mathrm{L}} \\ \left(\frac{\partial (\rho u)^*_{\mathrm{L}}}{\partial \mathbf{U}_{\mathrm{L,R}}}\right)^{\mathrm{T}} S_M + \left(\frac{\partial S_M}{\partial \mathbf{U}_{\mathrm{L,R}}}\right)^{\mathrm{T}} (\rho u)^*_{\mathrm{L}} + \left(\frac{\partial p^*}{\partial \mathbf{U}_{\mathrm{L,R}}}\right)^{\mathrm{T}} n_x \\ \left(\frac{\partial (\rho v)^*_{\mathrm{L}}}{\partial \mathbf{U}_{\mathrm{L,R}}}\right)^{\mathrm{T}} S_M + \left(\frac{\partial S_M}{\partial \mathbf{U}_{\mathrm{L,R}}}\right)^{\mathrm{T}} (\rho v)^*_{\mathrm{L}} + \left(\frac{\partial p^*}{\partial \mathbf{U}_{\mathrm{L,R}}}\right)^{\mathrm{T}} n_y \\ \left(\frac{\partial (\rho w)^*_{\mathrm{L}}}{\partial \mathbf{U}_{\mathrm{L,R}}}\right)^{\mathrm{T}} S_M + \left(\frac{\partial S_M}{\partial \mathbf{U}_{\mathrm{L,R}}}\right)^{\mathrm{T}} (\rho w)^*_{\mathrm{L}} + \left(\frac{\partial p^*}{\partial \mathbf{U}_{\mathrm{L,R}}}\right)^{\mathrm{T}} n_z \\ \left(\frac{\partial E^{\mathrm{t}*}_{\mathrm{L}}}{\partial \mathbf{U}_{\mathrm{L,R}}} + \frac{\partial p^*}{\partial \mathbf{U}_{\mathrm{L,R}}}\right)^{\mathrm{T}} S_M + \left(E^{\mathrm{t}*}_{\mathrm{L}} + p^*\right)\left(\frac{\partial S_M}{\partial \mathbf{U}_{\mathrm{L,R}}}\right)^{\mathrm{T}} \end{pmatrix}. \tag{2.25}$$

The derivative of the flux $\mathbf{F}^*_{\mathrm{R}}$ is the same as Eq. (2.25) once the left average state $\mathbf{U}^*_{\mathrm{L}}$ is changed to $\mathbf{U}^*_{\mathrm{R}}$.

The average states derivatives are

$$\frac{\partial \rho^*_{\mathrm{L}}}{\partial \mathbf{U}_{\mathrm{L}}} = \Omega_{\mathrm{L}} \begin{pmatrix} S_L \\ -n_x \\ -n_y \\ -n_z \\ 0 \end{pmatrix} + \rho^*_{\mathrm{L}} \Omega_{\mathrm{L}} \frac{\partial S_M}{\partial \mathbf{U}_{\mathrm{L}}}, \tag{2.26}$$

$$\frac{\partial \rho^*_{\mathrm{L}}}{\partial \mathbf{U}_{\mathrm{R}}} = \rho^*_{\mathrm{L}} \Omega_{\mathrm{L}} \frac{\partial S_M}{\partial \mathbf{U}_{\mathrm{R}}}, \tag{2.27}$$

$$\frac{\partial (\rho u)^*_{\mathrm{L}}}{\partial \mathbf{U}_{\mathrm{L}}} = \Omega_{\mathrm{L}} \begin{pmatrix} (\rho u)_{\mathrm{L}} q_{n_{\mathrm{L}}}/\rho_{\mathrm{L}} - n_x \Pi_{\mathrm{L}_\rho} \\ S_L - q_{n_{\mathrm{L}}} - (\rho u)_{\mathrm{L}} n_x/\rho_{\mathrm{L}} - n_x \Pi_{\mathrm{L}_{m_x}} \\ -(\rho u)_{\mathrm{L}} n_y/\rho_{\mathrm{L}} - n_x \Pi_{\mathrm{L}_{m_y}} \\ -(\rho u)_{\mathrm{L}} n_z/\rho_{\mathrm{L}} - n_x \Pi_{\mathrm{L}_{m_z}} \\ -\Pi_{\mathrm{L}_{E^{\mathrm{t}}}} n_x \end{pmatrix} + \Omega_{\mathrm{L}} \left(n_x \frac{\partial p^*}{\partial \mathbf{U}_{\mathrm{L}}} + (\rho u)^*_{\mathrm{L}} \frac{\partial S_M}{\partial \mathbf{U}_{\mathrm{L}}} \right), \tag{2.28}$$

$$\frac{\partial (\rho u)^*_{\mathrm{L}}}{\partial \mathbf{U}_{\mathrm{R}}} = \Omega_{\mathrm{L}} \left((\rho u)^*_{\mathrm{L}} \frac{\partial S_M}{\partial \mathbf{U}_{\mathrm{R}}} + n_x \frac{\partial p^*}{\partial \mathbf{U}_{\mathrm{R}}} \right), \tag{2.29}$$

$$\frac{\partial(\rho v)^*_{\mathrm{L}}}{\partial \mathbf{U}_{\mathrm{L}}} = \Omega_{\mathrm{L}} \begin{pmatrix} (\rho v)_{\mathrm{L}} q_{n_{\mathrm{L}}}/\rho_{\mathrm{L}} - n_y \Pi_{\mathrm{L}_\rho} \\ -(\rho v)_{\mathrm{L}} n_x/\rho_{\mathrm{L}} - n_y \Pi_{\mathrm{L}_{m_x}} \\ S_L - q_{n_{\mathrm{L}}} - (\rho v)_{\mathrm{L}} n_y/\rho_{\mathrm{L}} - n_y \Pi_{\mathrm{L}_{m_y}} \\ -(\rho v)_{\mathrm{L}} n_z/\rho_{\mathrm{L}} - n_y \Pi_{\mathrm{L}_{m_z}} \\ -\Pi_{\mathrm{L}_{E^{\mathrm{t}}}} n_y \end{pmatrix} + \Omega_{\mathrm{L}} \left(n_y \frac{\partial p^*}{\partial \mathbf{U}_{\mathrm{L}}} + (\rho v)^*_{\mathrm{L}} \frac{\partial S_M}{\partial \mathbf{U}_{\mathrm{L}}} \right), \tag{2.30}$$

$$\frac{\partial(\rho v)^*_{\mathrm{L}}}{\partial \mathbf{U}_{\mathrm{R}}} = \Omega_{\mathrm{L}} \left((\rho v)^*_{\mathrm{L}} \frac{\partial S_M}{\partial \mathbf{U}_{\mathrm{R}}} + n_y \frac{\partial p^*}{\partial \mathbf{U}_{\mathrm{R}}} \right), \tag{2.31}$$

$$\frac{\partial(\rho w)^*_{\mathrm{L}}}{\partial \mathbf{U}_{\mathrm{L}}} = \Omega_{\mathrm{L}} \begin{pmatrix} (\rho w)_{\mathrm{L}} q_{n_{\mathrm{L}}}/\rho_{\mathrm{L}} - n_z \Pi_{\mathrm{L}_\rho} \\ -(\rho w)_{\mathrm{L}} n_x/\rho_{\mathrm{L}} - n_z \Pi_{\mathrm{L}_{m_x}} \\ -(\rho w)_{\mathrm{L}} n_y/\rho_{\mathrm{L}} - n_z \Pi_{\mathrm{L}_{m_y}} \\ S_L - q_{n_{\mathrm{L}}} - (\rho w)_{\mathrm{L}} n_z/\rho_{\mathrm{L}} - n_z \Pi_{\mathrm{L}_{m_z}} \\ -\Pi_{\mathrm{L}_{E^{\mathrm{t}}}} n_z \end{pmatrix} + \Omega_{\mathrm{L}} \left(n_z \frac{\partial p^*}{\partial \mathbf{U}_L} + (\rho w)^*_{\mathrm{L}} \frac{\partial S_M}{\partial \mathbf{U}_{\mathrm{L}}} \right), \tag{2.32}$$

$$\frac{\partial(\rho w)^*_{\mathrm{L}}}{\partial \mathbf{U}_{\mathrm{R}}} = \Omega_{\mathrm{L}} \left((\rho w)^*_{\mathrm{L}} \frac{\partial S_M}{\partial \mathbf{U}_{\mathrm{R}}} + n_z \frac{\partial p^*}{\partial \mathbf{U}_{\mathrm{R}}} \right), \tag{2.33}$$

$$\frac{\partial E^{\mathrm{t}*}_{\mathrm{L}}}{\partial \mathbf{U}_{\mathrm{L}}} = \Omega_{\mathrm{L}} \begin{pmatrix} q_{n_{\mathrm{L}}}/\rho_{\mathrm{L}}(E^{\mathrm{t}}{}_{\mathrm{L}} + p_{\mathrm{L}}) - q_{n_{\mathrm{L}}} \Pi_{\mathrm{L}_\rho} \\ -n_x/\rho_{\mathrm{L}}(E^{\mathrm{t}}{}_{\mathrm{L}} + p_{\mathrm{L}}) - q_{n_{\mathrm{L}}} \Pi_{\mathrm{L}_{m_x}} \\ -n_y/\rho_{\mathrm{L}}(E^{\mathrm{t}}{}_{\mathrm{L}} + p_{\mathrm{L}}) - q_{n_{\mathrm{L}}} \Pi_{\mathrm{L}_{m_y}} \\ -n_z/\rho_{\mathrm{L}}(E^{\mathrm{t}}{}_{\mathrm{L}} + p_{\mathrm{L}}) - q_{n_{\mathrm{L}}} \Pi_{\mathrm{L}_{m_z}} \\ S_L - q_{n_{\mathrm{L}}} - \Pi_{\mathrm{L}_{E^{\mathrm{t}}}} q_{n_{\mathrm{L}}} \end{pmatrix} + \Omega_{\mathrm{L}} \left(S_M \frac{\partial p^*}{\partial \mathbf{U}_{\mathrm{L}}} + \left(E^{\mathrm{t}*}_{\mathrm{L}} + p^* \right) \frac{\partial S_M}{\partial \mathbf{U}_{\mathrm{L}}} \right), \tag{2.34}$$

$$\frac{\partial E^{\mathrm{t}*}_{\mathrm{L}}}{\partial \mathbf{U}_{\mathrm{R}}} = \Omega_{\mathrm{L}} \left(S_M \frac{\partial p^*}{\partial \mathbf{U}_{\mathrm{R}}} + \frac{\partial S_M}{\partial \mathbf{U}_{\mathrm{R}}} \left(E^{\mathrm{t}*}_{\mathrm{L}} + p^* \right) \right), \tag{2.35}$$

$$\frac{\partial p^*}{\partial \mathbf{U}_{\mathrm{L,R}}} = \rho_{\mathrm{L,R}} \left(S_{R,L} - q_{n_{\mathrm{R,L}}} \right) \frac{\partial S_M}{\partial \mathbf{U}_{\mathrm{L,R}}}. \tag{2.36}$$

In Eq. (2.26)-(2.36) the relation $\partial\Omega_{\mathrm{L}}/\partial\mathbf{U}_{\mathrm{L}} = \Omega^2_{\mathrm{L}} \partial S_M/\partial\mathbf{U}_{\mathrm{L}}$ has been used. The expressions for the pressure derivatives are given in A.1. The derivatives of the right state $\mathbf{U}^*_{\mathrm{R}}$ are easily obtained by interchanging the subscript $_{\mathrm{L}}$ with $_{\mathrm{R}}$, and S_L with S_R on the right-hand side

of Eq. (2.26)-(2.34). The derivatives of the intermediate wave speed are given by

$$\frac{\partial S_M}{\partial \mathbf{U}_{\mathrm{L,R}}} = \tilde{\rho}^{-1} \begin{pmatrix} \mp q_{n_{\mathrm{L,R}}}^2 \pm \Pi_{\mathrm{L,R}_\rho} \pm S_M S_{L,R} \\ n_x \left(\pm 2 q_{n_{\mathrm{L,R}}} \mp S_{L,R} \mp S_M \right) \pm \Pi_{\mathrm{L,R}_{m_x}} \\ n_y \left(\pm 2 q_{n_{\mathrm{L,R}}} \mp S_{L,R} \mp S_M \right) \pm \Pi_{\mathrm{L,R}_{m_y}} \\ n_z \left(\pm 2 q_{n_{\mathrm{L,R}}} \mp S_{L,R} \mp S_M \right) \pm \Pi_{\mathrm{L,R}_{m_z}} \\ \pm \Pi_{\mathrm{L,R}_{E^t}} \end{pmatrix}, \tag{2.37}$$

with $\tilde{\rho} = \rho_{\mathrm{R}} \left(S_R - q_{n_{\mathrm{R}}} \right) - \rho_{\mathrm{L}} \left(S_L - q_{n_{\mathrm{L}}} \right)$.

2.3.4 Kurganov and Tadmor central scheme

The Kurganov and Tadmor (KT) central scheme [48] allows to calculate the inviscid fluxes without any knowledge of the eigenstructure of the interface Riemann problem. They are expressed as

$$\mathbf{F}_{j+\frac{1}{2}}(\mathbf{U}_{\mathrm{L}}, \mathbf{U}_{\mathrm{R}}) = \frac{\mathbf{F}_{\mathrm{con}}(\mathbf{U}_{\mathrm{R}}) + \mathbf{F}_{\mathrm{con}}(\mathbf{U}_{\mathrm{L}})}{2} - \frac{a_{j+\frac{1}{2}}}{2} \left(\mathbf{U}_{\mathrm{R}} - \mathbf{U}_{\mathrm{L}} \right), \tag{2.38}$$

with $a_{j+\frac{1}{2}}$ being the maximum local propagation speed

$$a_{j+\frac{1}{2}} = \max_{\mathrm{L,R}} \left(\rho \left(\frac{\partial \mathbf{F}_{\mathrm{con}}}{\partial \mathbf{U}} \left(\mathbf{U}_{\mathrm{L,R}} \right) \right) \right). \tag{2.39}$$

In this three-dimensional extension its value is taken as $a_{j+\frac{1}{2}} = \max(\lambda_{\mathrm{L}}, \lambda_{\mathrm{R}})$, with $\lambda_{\mathrm{L}} = \max(|q_{n_{\mathrm{L}}} + c_{\mathrm{L}}|, |q_{n_{\mathrm{L}}} - c_{\mathrm{L}}|)$ and $\lambda_{\mathrm{R}} = \max(|q_{n_{\mathrm{R}}} + c_{\mathrm{R}}|, |q_{n_{\mathrm{R}}} - c_{\mathrm{R}}|)$. Considering a frozen local propagation speed, the derivation of the implicit Jacobians is

$$A_{\mathrm{L,R}}(\mathbf{U}_{\mathrm{L}}, \mathbf{U}_{\mathrm{R}}) = \frac{1}{2} \left(A_{\mathrm{con}}(\mathbf{U}_{\mathrm{L,R}}) \pm a_{j+\frac{1}{2}} \mathbb{I} \right). \tag{2.40}$$

This scheme is extremely compact and requires only few operations to evaluate both fluxes and Jacobians. The extension to include a dense gas equation of state model only needs the generalization of the expression of $\mathbf{F}_{\mathrm{con}}$ and A_{con}, see e.g. [33]. However, the simplified approximations of the KT scheme lead to a higher numerical dissipation in its semi-discrete formulation, if compared to Roe, AUSM$^+$, and HLLC. Several modifications were proposed to overcome this issue, often applicable to two-dimensional structured grids only [48,59–61].

2.3.5 Hybrid schemes: AUSM$^+$-KT and HLLC-KT

A hybrid numerical discretization is also possible, whereby the Jacobian on the left hand side (LHS) and the explicit flux on the right hand side (RHS) of the Newton–Raphson scheme are evaluated using two different approximate Riemann solvers. Two combinations considered in this paper are: AUSM$^+$ (RHS) and KT (LHS) referred to as AUSM$^+$-KT; and HLLC (RHS) and KT (LHS) referred to as HLLC-KT. This is a simple commonly used approach and the results of these hybrid methods will be discussed in therms of convergence achieved in Sec. 5.4.

2.3.6 Scalar transport equations

It is common to solve scalar transport equations in numerical simulations, such as turbulence models in the framework of Reynolds-averaged Navier–Stokes (RANS), combustion models, scalar dispersion, etc. All the schemes described above can be easily extended to the advection of a generic scalar ϕ_i. It should be mentioned that for the KT scheme the intensity of the artificial dissipation can be reduced by replacing the maximum local propagation speed, defined in Eq. (2.39), with the convective velocity

$$a_{j+\frac{1}{2}} \equiv \max(|q_{n_\mathrm{L}}|, |q_{n_\mathrm{R}}|). \tag{2.41}$$

The flux for the scalar then reads

$$F_{\mathrm{sca},i} = \frac{1}{2}\left(q_{n_\mathrm{R}}\rho_\mathrm{R}\phi_{i_\mathrm{R}} + q_{n_\mathrm{L}}\rho_\mathrm{L}\phi_{i_\mathrm{L}} - a_{j+\frac{1}{2}}\left(\rho_\mathrm{R}\phi_{i_\mathrm{R}} - \rho_\mathrm{L}\phi_{i_\mathrm{L}}\right)\right), \tag{2.42}$$

and the Jacobian is

$$\mathbf{A}_{\mathrm{sca},i_{\mathrm{R,L}}} = \frac{1}{2}\left(\left(q_{n_{\mathrm{R,L}}} \mp a_{j+\frac{1}{2}}\right)\phi_{i_{\mathrm{R,L}}},\ n_x\phi_{i_{\mathrm{R,L}}},\ n_y\phi_{i_{\mathrm{R,L}}},\ n_z\phi_{i_{\mathrm{R,L}}},\ 0,\ q_{n_{\mathrm{R,L}}} \mp a_{j+\frac{1}{2}}\right). \tag{2.43}$$

2.4 Diffusive fluxes

The diffusive fluxes are expressed as

$$\mathbf{F}_\mathrm{dif}(\mathbf{Q}) = \begin{pmatrix} 0 \\ \mathbf{n}\cdot\tau \\ \mathbf{v}\cdot(\mathbf{n}\cdot\tau) + \mathbf{n}\cdot(\lambda\nabla T) \end{pmatrix}, \tag{2.44}$$

with $\tau = \mu\left(\nabla\otimes\mathbf{v} + (\nabla\otimes\mathbf{v})^\mathrm{T} - \frac{2}{3}(\nabla\cdot\mathbf{v})\,\mathbb{I}\right)$ being the viscous stress tensor, μ the fluid dynamic viscosity, and λ the thermal conductivity. $\mathbf{Q} = (\rho, u, v, w, T)^\mathrm{T}$ is the vector of the primitive variables. The velocity and temperature gradients at each face are calculated as

$$\nabla\phi|_\mathrm{f}\cdot\mathbf{n}_\mathrm{f} = \frac{\phi_\mathrm{A} - \phi_\mathrm{B}}{\|\mathbf{x}_\mathrm{A} - \mathbf{x}_\mathrm{B}\|}\alpha_\mathrm{f} + \frac{1}{2}\left(\nabla\phi|_\mathrm{A} + \nabla\phi|_\mathrm{B}\right)\cdot\left(\mathbf{n}_\mathrm{f} - \alpha_\mathrm{f}\mathbf{s}_\mathrm{f}\right), \tag{2.45}$$

where ϕ is a generic variable, A and B denote the two cell centers sharing the face f, $\alpha = \mathbf{s}\cdot\mathbf{n}$, and $\mathbf{s}$ is the normalized vector connecting the A and B cell centroids. More details can be found in Refs.[62,63]. The flux Jacobian needed for the implicit time integration is obtained following Pulliam and Steger[49] as:

$$A_\mathrm{dif}(\mathbf{U}) = \frac{\partial\mathbf{F}_\mathrm{dif}(\mathbf{Q})}{\partial\mathbf{Q}}\frac{\partial\mathbf{Q}}{\partial\mathbf{U}}. \tag{2.46}$$

For a dense gas, the viscosity and thermal conductivity variations must be included in the calculation of $\partial\mathbf{F}_\mathrm{dif}(\mathbf{Q})/\partial\mathbf{Q}$. If not available from the thermodynamic library, the following derivatives

$$\frac{\partial\mu(\rho,T)}{\partial\rho},\quad \frac{\partial\mu(\rho,T)}{\partial T},\quad \frac{\partial\lambda(\rho,T)}{\partial\rho},\quad \text{and}\quad \frac{\partial\lambda(\rho,T)}{\partial T}, \tag{2.47}$$

can be numerically computed by means of finite differences using the tabulated values for μ and λ. The temperature derivatives needed for the evaluation of the tensor $\partial\mathbf{Q}/\partial\mathbf{U}$ can be expressed using the chain rule on $\Theta = T(\rho, e(\rho, \mathbf{m}, E^{\mathrm{t}}))$

$$\frac{\partial\Theta}{\partial\rho} = \frac{\partial T}{\partial\rho} + \frac{\partial T}{\partial e}\frac{\partial e}{\partial\rho}, \quad \frac{\partial\Theta}{\partial E^{\mathrm{t}}} = \frac{\partial T}{\partial e}\frac{\partial e}{\partial E^{\mathrm{t}}}, \quad \text{and} \quad \frac{\partial\Theta}{\partial m_i} = -v_i\frac{\partial\Theta}{\partial E^{\mathrm{t}}}, \tag{2.48}$$

which is valid for any equation of state. The specific internal energy as a function of the conservative variables is given by

$$e(\rho, \mathbf{m}, E^{\mathrm{t}}) = \frac{1}{\rho}\left(E^{\mathrm{t}} - \frac{1}{2}\frac{\|\mathbf{m}\|^2}{\rho}\right). \tag{2.49}$$

2.5 Results

The accuracy and the convergence rate of simulations using the the inviscid and viscous flux schemes from Sec. 2.3 and 2.4 are assessed for five paradigmatic cases. These are, a one-dimensional Riemann problem, an inviscid supersonic flow over a ramp, a bi-bump channel, a cylinder in supersonic cross flow, and a turbulent subsonic flow in a turbine cascade. Several fluids, relevant for technical applications, are considered and the simulation conditions are chosen such that the fluid's thermodynamic state is close to the liquid-vapor critical point, where strong variations of thermophysical properties occur. The code used to perform the simulations is an in-house finite volume Navier–Stokes solver developed by Pecnik *et al.*[64]. The implicit Euler time integration scheme is used in all cases, except for the one-dimensional Riemann problem, which is solved using the explicit three-step Runge–Kutta method of Shu and Osher[65]. The large sparse linear system resulting from the implicit time integration is solved using PETSc[66], which implements the generalized minimal residual algorithm[67], pre-conditioned with the incomplete LU factorization. In all simulations, the initial Courant number CFL of the time integration scheme is set to 1, and gradually increased at each time step up to a maximum value $CFL = 1000$. Unless otherwise specified, a second order spatial discretization scheme is used.

The look-up table method presented in Sec. 2.2 is employed in all simulations. However, computations using direct solution of the equation of state model are also performed, but since no differences were found in the calculated flow field, those results are not presented here. The thermodynamic properties are tabulated using an in-house library[68].

2.5.1 One-dimensional Riemann problem

Helium is the selected fluid for this test case, and its thermodynamic properties are calculated according to the model implemented in Ref.[52]. The initial left and right states are summarized in Tab. 2.1. A constant time step $\Delta t = 2.5 \times 10^{-4}$ is used to integrate the equations until $t = 0.02$ s. The grid discretizes $x \in [-5, 5]$ using 200 intervals.

Results are shown in Fig. 2.4 and compared with the exact described in A.2. All numerical schemes are in good agreement with the reference solution, with the KT central

Table 2.1: Initial conditions of the one-dimensional Riemann problem. Helium is the fluid selected. The subscript $_r$ indicates reduced quantities.

	P_r	T_r	ρ [kg/m^3]	u [m/s]	P [bar]
Right	0.95	1.1	26.56	0.0	2.161
Left	2.825	1.275	96.38	0.0	6.426

scheme being the most diffusive. A discontinuity is observed in the velocity field. According to Clerc [69] this is inherent to the conservative formulation of the discretized Euler equations and depends on the nonlinear shape of the isobars in the $\rho - \rho e$ plane. However, to explain the nature of the observed phenomenon in details, further quantifications are required which is outside of the scope of this work. Fig. 2.5 shows all the thermodynamic states which define the solution of the Riemann problem on the $\rho - T$ plane, including contour lines for $1 - z$, with $z = P/\rho RT$ being the compressibility factor.

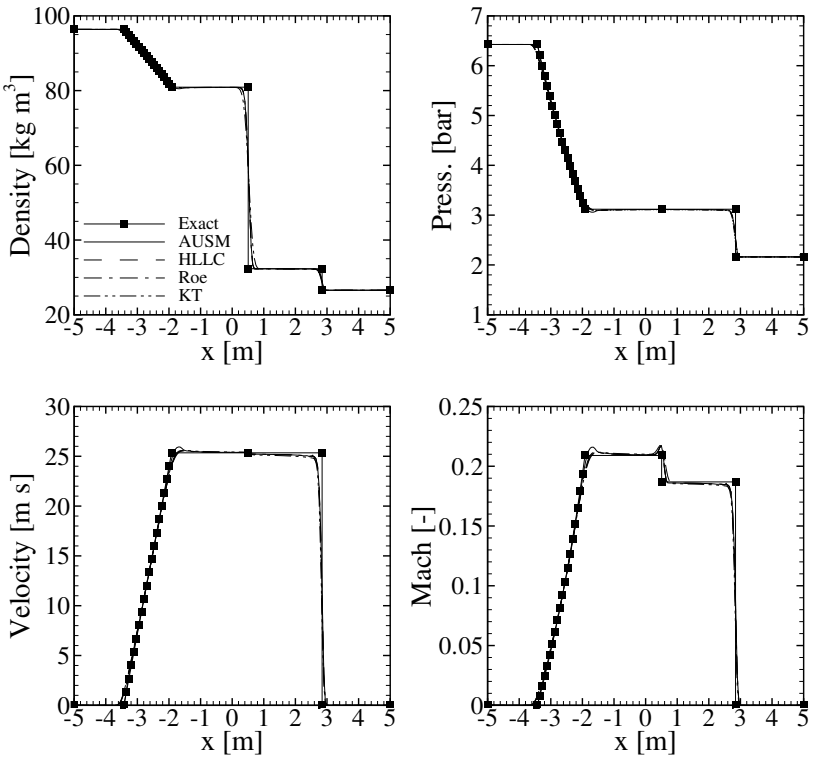

Figure 2.4: Solution of the Riemann problem. Helium is the fluid selected. The initial conditions are reported in Tab. 2.1.

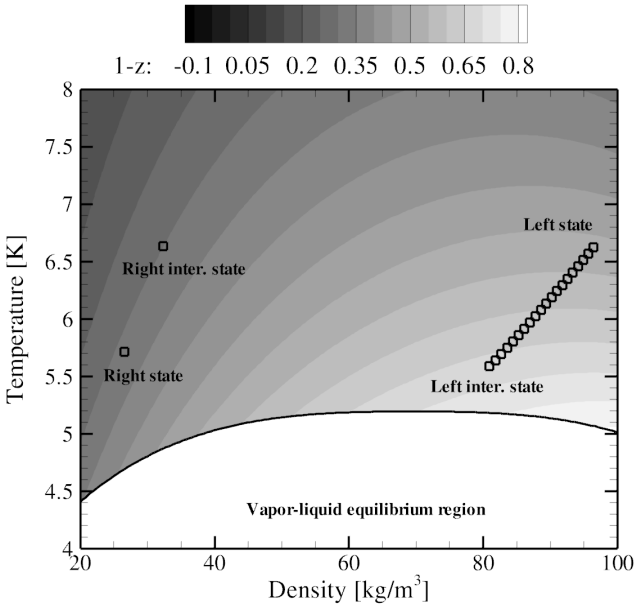

Figure 2.5: Thermodynamic states of the solution of the Riemann problem described in Tab. 2.1 and Fig. 2.4. Contour lines are for $1-z$, with $z = P/\rho RT$ being the compressibility factor. When $1 - z = 0$ the ideal gas assumption holds.

2.5.2 Supersonic flow over a ramp

This test case is a supersonic inviscid flow (inlet Mach number $M = 2$) of hydrogen over a ramp with a slope of 2.5 deg. The geometry is discretized on a mesh with 222×174 control volumes. The inlet conditions are given in terms of reduced pressure $P_r = 1.05$ and reduced temperature $T_r = 1.05$. The polynomial table interpolation is used to evaluate the thermodynamic properties. The Mach number distribution shows an oblique shock wave followed by a centered rarefaction fan, and is displayed in Fig. 2.6.

The numerical solution is compared with the exact solution obtained by solving the Rankine–Hugoniot relations across the shock wave and integrating the Prandtl–Meyer ordinary differential equation. Since no closed form solution for these two nonlinear waves can be obtained for a real gas, the two sets of equations are solved numerically. Properties are directly evaluated using the hydrogen thermodynamic model implemented in Ref.[52]. Tab. 2.2 compares the exact solution to the average post shock and post fan states obtained by the CFD solver using the four different schemes. The agreement is satisfactory with maximum deviations of less than 0.02 %.

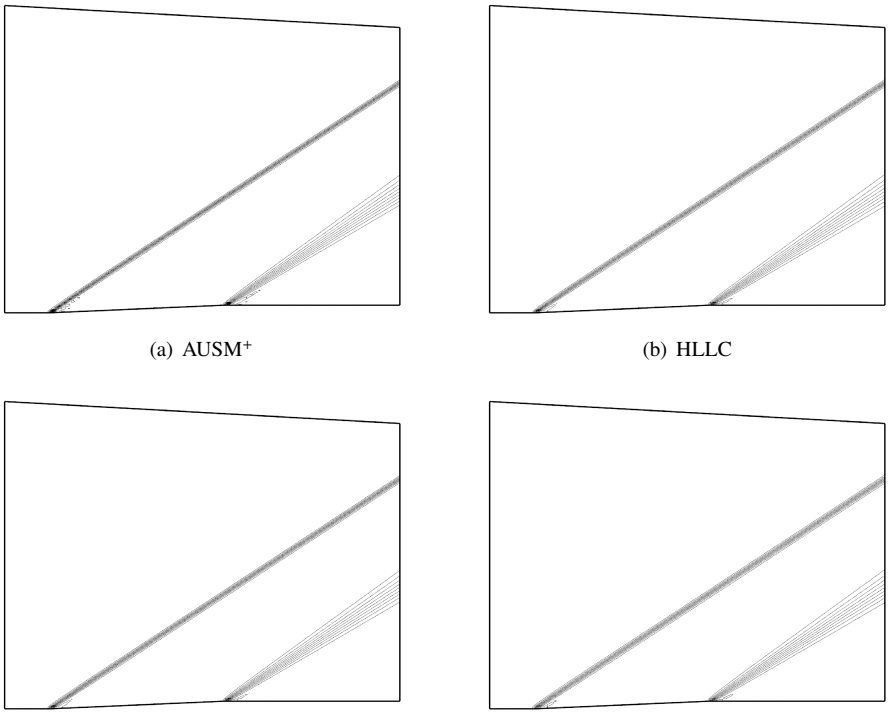

(a) AUSM$^+$ (b) HLLC

(c) Roe (d) KT

Figure 2.6: Mach number contour lines (15 levels from 1.7 to 2.0) for the ramp test case. Inlet conditions are $M = 2$, $P_r = 1.05$, $T_r = 1.05$. The angle of the slope is 2.5 deg.

Table 2.2: Post-shock and post-fan states obtained averaging the CFD results. The direct solution of the Rankine–Hugoniot relations together with the integration of the Prandtl–Meyer ordinary differential equation is also reported in the first row. Fluid properties are calculated using table interpolation except for the last simulation included, which uses direct solution of the equation of state (DC).

	Post shock state			Post fan state		
	ρ [kg/m^3]	P [bar]	M [−]	ρ [kg/m^3]	P [bar]	M [−]
Exact	18.4785	16.8556	1.79802	16.7624	13.6128	1.99969
AUSM$^+$	18.4787	16.8579	1.79791	16.7609	13.6150	1.99932
HLLC	18.4799	16.8604	1.79777	16.7580	13.6108	1.99958
Roe	18.4799	16.8604	1.79777	16.7580	13.6108	1.99958
KT	18.4806	16.8617	1.79771	16.7574	13.6102	1.99961
HLLC DC	18.4799	16.8604	1.79777	16.7580	13.6108	1.99958

Table 2.3: Initial conditions for the bi-bump test case.

Fluid	P_r	T_r	M
MD_6M	0.94	0.997	1.6
CO_2	1.05	1.15	1.6

Fig. 2.7 shows the convergence histories of the schemes using the residual of the energy equation. The AUSM$^+$, Roe, and HLLC schemes show very similar convergence features. In fact, the Roe and HLLC schemes are the same due to the supersonic nature of the flow, where the HLLC and Roe flux corresponds to the Euler flux given in Eq. (2.2). The KT scheme shows slightly slower convergence.

The convergence rate of HLLC using direct solution (DC) of the thermodynamic model is also presented, and shows a deterioration of convergence after 6 orders of magnitude. This can be related to the numerical tolerance used in the Newton–Raphson iteration for the inversion of the equation of state model in the external library.

The performance of the two hybrid schemes AUSM$^+$-KT and HLLC-KT is found to be in both cases sensibly worse as compared to the base schemes with a consistent exact Jacobian. Similar behavior of the converge history was observed by several authors when using an approximate definition of the Jacobian matrix for ideal gas simulations. Batten *et al.*[56] shown that a fully linearized approximate Riemann solver flux function converges faster than the case when the Jacobian matrix is considered frozen (for the Roe scheme) or is obtained under the assumption of frozen wave speeds (in case of HLLC scheme). In the context of adjoint shape optimization, Dwight and Brezillon[70] studied approximations of the gradients with respect to a full linearization of all the terms in the flow solver, and observed that they may have similar performance with respect to the exact differentiation in some cases, but may also converge sensibly slower in other. Similar remarks were presented by Carpentieri *et al.*[71], who highlighted that quadratic converge for the Roe scheme is obtained only if the Jacobian is exact, and concluded that first-order accurate approximations are not effective since their optimization procedure stalled for all the test cases considered.

2.5.3 Supersonic flow in a two-dimensional bi-bump channel

The bi-bump test case, introduced by Monaco *et al.*[9], is studied with two different fluids with inlet conditions reported in Tab. 2.3. The thermodynamic models are based on the iPRSV cubic equation of state[54] for MD_6M, and on the Span–Wagner multiparameter equation of state[52] CO_2. The mesh consists of 499×249 control volumes.

Considering the flow of MD_6M, a pattern of interacting shocks is observed, whose intensity is weak due to the low value of the fundamental derivative of gasdynamics Γ[4], see also Ref.[33], which is negative at the inlet. Fig. 2.9 shows that, in the case of the CO_2 flow, the shocks are stronger as the value of Γ is well above 1.

The convergence history of the energy residual is plotted in Fig. 2.10. For both simulations, a similar behavior is observed as for the ramp test case. Again, the HLLC and Roe

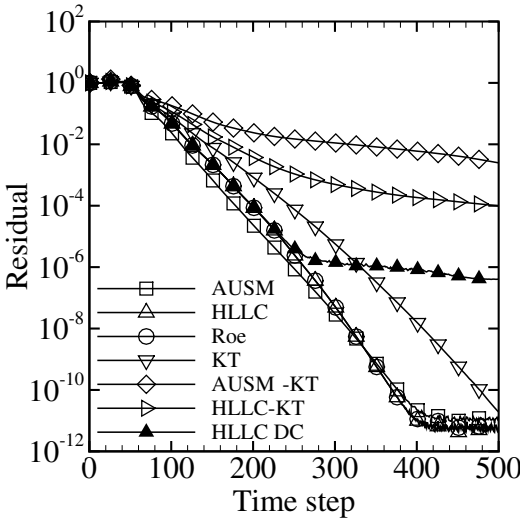

Figure 2.7: Convergence history of the energy equation residual for the ramp test case of Fig.2.6.

schemes convergence is the same. Interestingly, the AUSM$^+$ shows a temporary convergence rate deterioration after the residual has decreased by 4 orders of magnitude. Several tests with different interpolation schemes, table refinement, and also using direct solution of the thermodynamic model ruled out the inaccuracy or inconsistency of the interpolated thermodynamic properties to be the reason for this convergence deterioration. Similarly to the case discussed in Sec. 2.5.2, also here the hybrid schemes show the slowest convergence. In fact, with the AUSM$^+$-KT scheme no stable solution was achieved using the same integration parameters for the MD_6M case.

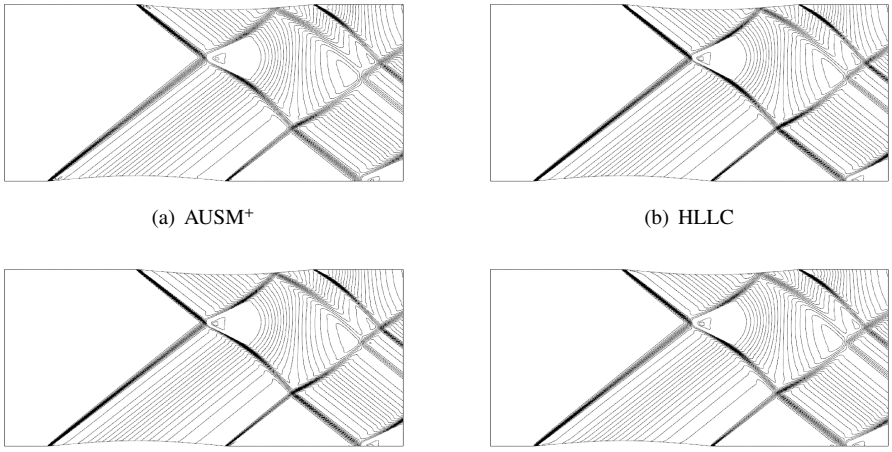

(a) AUSM$^+$ (b) HLLC

(c) Roe (d) KT

Figure 2.8: Mach number contour lines (20 levels between 1.4 and 1.9) for the supersonic MD_6M flow in a bi-bump channel. The inlet boundary conditions are summarized in Tab. 2.3.

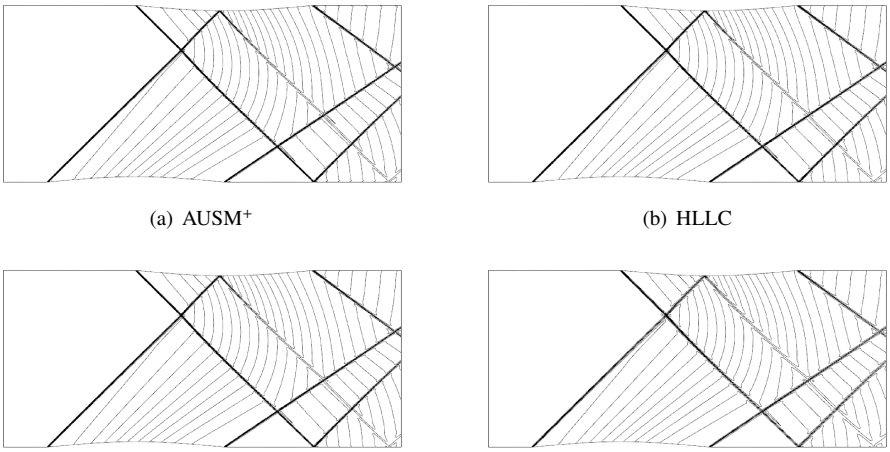

(a) AUSM$^+$ (b) HLLC

(c) Roe (d) KT

Figure 2.9: Mach number contour lines (20 levels between 1.2 and 1.9) for the supersonic CO_2 flow in a bi-bump duct. The inlet boundary conditions are summarized in Tab. 2.3.

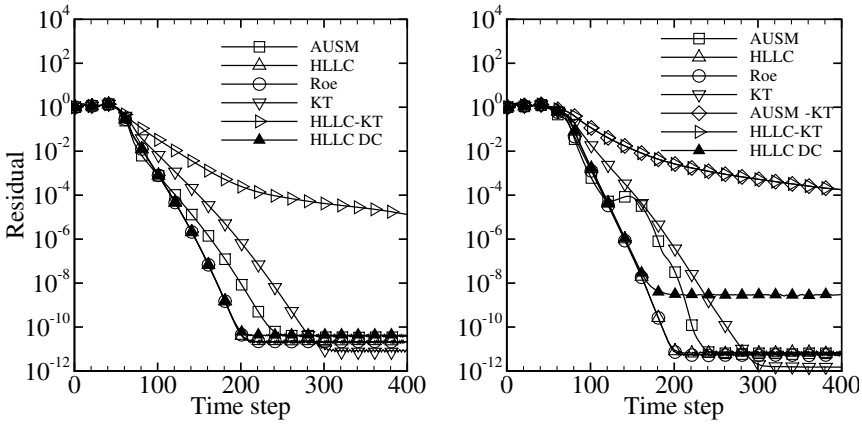

(a) Subcritical MD_6M (b) Supercritical CO_2

Figure 2.10: Convergence history of the energy equation residual for the bi-bump test case of Fig. 2.8 and 2.9.

2.5.4 Cylinder in supersonic cross flow

The inviscid simulation of a cylinder in supersonic cross flow is analyzed here with MDM vapor as the fluid. A uniform inflow at $M = 2.5$, $P = 11.48$ bar, and $T = 554.3$ K is chosen, which corresponds to the subcritical state with $P_r = 0.811$ and $T_r = 0.983$. The initial conditions are selected such that the flow evolves in the transcritical region slightly below and above the critical point, where the thermodynamic properties vary abruptly, see Fig. 2.11. The multiparameter equation of state model implemented in Ref.[52] is used to generate the table. Compared to the bi-bump and ramp test cases, a more strict CFL condition is needed in order to prevent the solution from diverging during the first integration steps. This is mainly due to the thermodynamic state falling outside the tabulated region, which covers the range of validity of the thermodynamic model. A CFL of 2.5 is used for the first 200 steps, and then gradually increased by a factor of 1.05 at each time step up to 25. All the simulations are performed using first order spatial accuracy.

The obtained Mach number distribution is depicted in Fig. 2.12. The flow field is dominated by a strong bow shock wave. Downstream of the bow shock the flow is mainly subsonic, except for the region close to the outlet boundary. The thermodynamic states computed in all the cell centers using the AUSM$^+$ scheme are plotted in the $\rho - T$ plane, see Fig. 2.11. As already mentioned, they lie in the transcritical thermodynamic region of the selected fluid, making the test of the schemes particularly challenging. Contour lines for $1 - z$ are also shown in order to identify where the deviation from the ideal gas law is larger.

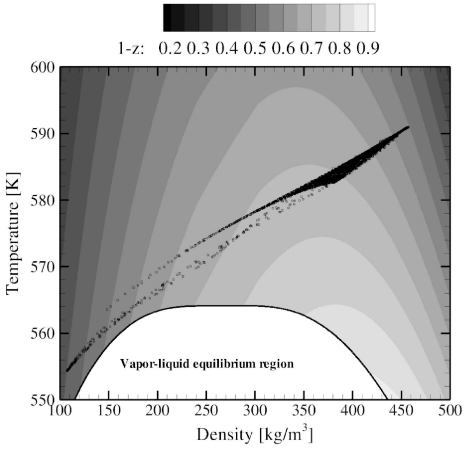

Figure 2.11: Calculated thermodynamic states of the cylinder in inviscid supersonic cross flow with MDM as the fluid. Contour lines are for $1 - z$, with $z = P/\rho RT$ being the compressibility factor.

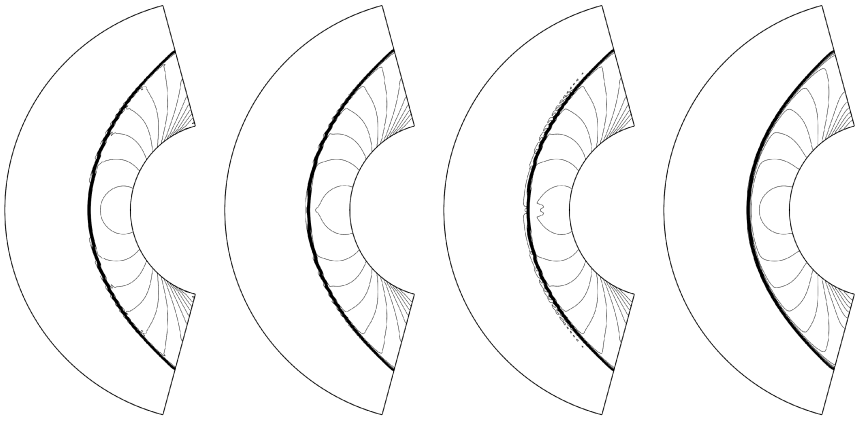

(a) AUSM$^+$ (b) HLLC (c) Roe (d) KT

Figure 2.12: Mach number contour lines (15 from 0 to 2.5) for a cylinder in supersonic cross flow with MDM as the fluid. The Inlet conditions are: $M = 2.5$, $P = 11.48$ bar, and $T = 554.3$ K.

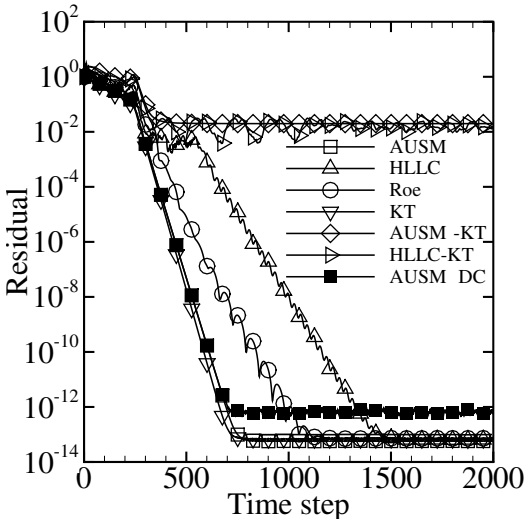

Figure 2.13: Convergence history for the supersonic flow over a cylinder test case of Fig. 2.12.

The convergence history of the energy equation residual is shown in Fig. 2.13. The best performance is obtained with the KT and AUSM$^+$ schemes, while the convergence is not monotonic for the Roe's solver which exhibits oscillations in the decrease of the residual. A trend similar to the one obtained with the ASUM$^+$ scheme for the case of supercritical CO_2 presented in Sec. 2.5.3 is observed for the HLLC scheme in this test case. After the CFL number is increased, the residual is stationary for about 300 time steps and later decreases to convergence. Both hybrid schemes fail to converge for this case. A similar stall of the residual was observed by Batten *et al.*[56] when using a frozen Jacobian matrix for the Roe solver for the same test case configuration, however for an ideal gas flow.

2.5.5 Two-dimensional subsonic flow through the VKI LS-89 turbine blade cascade

A test case of engineering interest is considered here, namely the turbulent flow of MDM through the well documented VKI LS-89 turbine cascade. The total inlet conditions are chosen to reasonably represent the operation of an organic Rankine cycle (ORC) turbine operating at supercritical temperatures: $T_{\text{tot}} = 219.1\ ^\circ\text{C}$ and $P_{\text{tot}} = 13.87$ bar. These correspond to the reduced values of $T_{\text{r}} = 1.05$ and $P_{\text{r}} = 0.98$. The outlet pressure is specified 3 chord length downstream of the trailing edge to avoid spurious reflections at the outlet affecting the flow around the blade with $P_{\text{out}} = 11$ bar.

The no-slip condition is applied on the solid wall, and periodicity is set on the upper and lower boundaries. The one equation turbulence model of Spalart and Allmaras[72] is used with the KT advection flux formulation, Eq. (2.42) and (2.43). Numerical observations showed that using the maximum local propagation speed (Eq. (2.39)) as the intensity of the numerical dissipation in Eq. (2.43) is beneficial for the convergence rate of the scalar. The inlet value of the turbulent viscosity is $\nu_{\text{SA}} \approx 1 \times 10^{-5}$. Approximately 16,000 hexahedral cells are used to discretize the domain, clustered on the blade surface. A maximum CFL number of 100 is used for the implicit time integration. The calculated Mach number flow field for the second order turbulent simulation is shown in Fig. 2.14. The predictions given by the AUSM$^+$, HLLC, and Roe's do not display significant differences, while a higher level of numerical diffusion is observed for the KT scheme.

Fig. 2.15(a) displays the convergence history of the energy equation residual for a laminar simulation using first order spatial discretization, and Fig. 2.15(b) for a turbulent simulation using second order spatial discretization. Because of the poor convergence behavior of the hybrid schemes (AUSM$^+$-KT and HLLC-KT) observed for the previous cases, they have not been considered for comparison. The convergence is found to be faster for the laminar case, showing a monotonic decrease of the residual. Interestingly, the KT scheme converges within only 500 time steps. Despite the oscillating behavior of the residual for the turbulent test case, it can be inferred from Fig. 2.15(b) that the solution is converged after 2000 steps for practical considerations (the residual is decreased by five orders of magnitude). To assess the influence of the viscous Jacobian including the derivatives of the transport properties (thermal conductivity λ and molecular viscosity

μ) two simulations were performed: one with and one without those derivatives. Based on the results (not shown) no convergence improvement was achieved. However, it is expected that closer to the pseudo critical line with strong variations of μ and λ a better convergence is obtained including the derivatives of the transport properties in the viscous Jacobian.

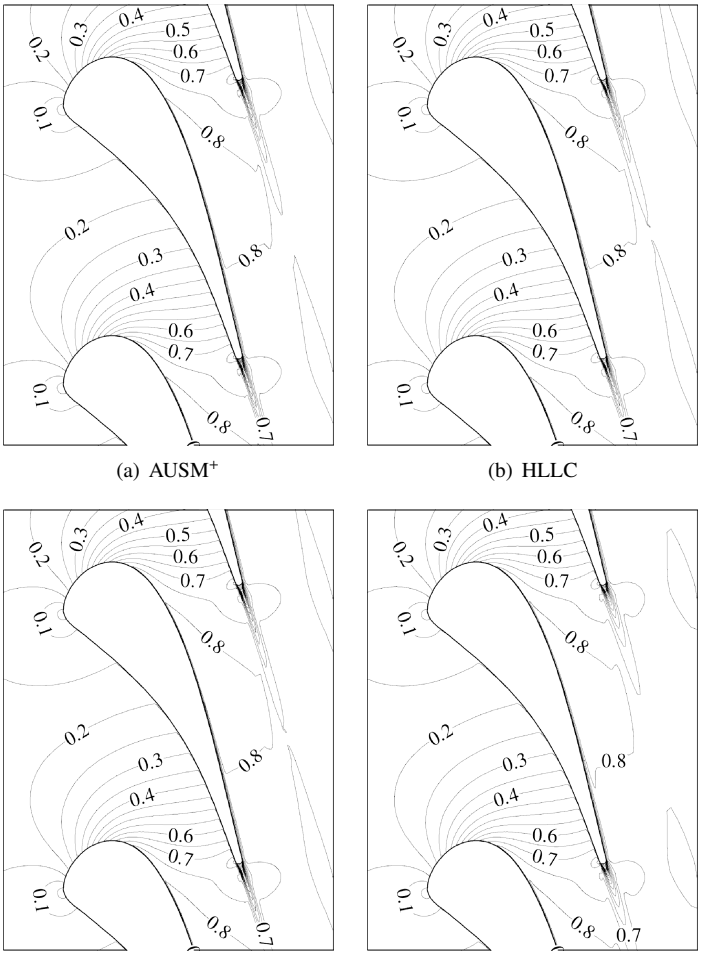

(a) AUSM$^+$ (b) HLLC

(c) Roe (d) KT

Figure 2.14: Mach number contour lines for a subsonic turbulent flow over the VKI LS-89 turbine blade cascade with MDM as the fluid.

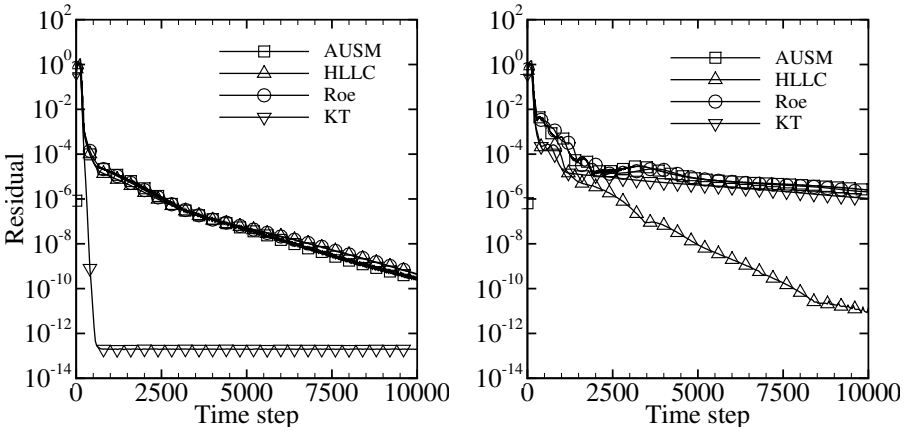

(a) Laminar first order.

(b) Turbulent second order.

Figure 2.15: Convergence history for the VKI LS-89 test case of Fig. 2.15.

2.6 Conclusions

This paper documents the implicit formulation of several approximate Riemann solvers with no assumption on the fluids' equation-of-state. The formulations are valid for any EOS model for the estimation of the fluid thermodynamic properties, and any temperature-dependent model for the transport properties. Analytical expressions of the exact flux Jacobians for the HLLC, AUSM$^+$, and Kurganov and Tadmor schemes are presented and the general approach allows the coupling to accurate thermophysical models for the simulation of real gas flows. Differences from the ideal gas formulation are pointed out, and can be summarized by the need for general expressions of partial derivatives of pressure and temperature with respect to the conserved variables vector and several additional terms in the diffusive flux Jacobians arising from temperature-dependent fluid viscosity and thermal conductivity.

A method for the computation of the fluid thermophysical properties based on the interpolation of look-up table is analyzed in terms of accuracy and consistency. Despite the latter cannot be enforced when the properties are interpolated independently one from another, a relatively small number of discretization nodes for the thermodynamic table is found to be sufficient as far as the consistency and accuracy of the property evaluations are concerned. The main advantage using the LUT method when compared to the direct solution of the equation of state model is the computational cost that is reduced by up to 4 orders of magnitude. The cost reduction can be even larger if a reference EoS model is used for the comparison.

Numerical experiments demonstrate the accuracy of the proposed numerical methods, and a comparison with the exact solution for the one-dimensional Riemann problem and the supersonic ramp test case validates their formulation. Other flow configurations are

also considered, including a turbulent flow through a turbine cascade. The wide variety of fluids selected for the test cases ensures the generality and flexibility of the methodology. From the results obtained for all the cases it is not possible to state which method performs best. However, the results indicate that in order to achieve convergence it is essential to use consistent formulations for the Jacobians based on the chosen flux scheme.

A.1 Pressure derivatives and speed of sound

The pressure relation can be conveniently written as a function of the conserved variables $\mathbf{U} = (\rho, \mathbf{m}, E^{\mathrm{t}})^{\mathrm{T}}$

$$P = P(\rho, e) = P\left(\rho, e\left(\rho, \mathbf{m}, E^{\mathrm{t}}\right)\right) = \Pi, \tag{50}$$

in which we introduced a different symbol to specify the new thermodynamic relation. In order to express the Jacobian of the Euler fluxes, the derivatives of Π are needed. Differentiating Eq. (50)

$$d\Pi = P_\rho d\rho + P_e\left(e_\rho d\rho + e_{\mathbf{m}} d\mathbf{m} + e_{E^{\mathrm{t}}} dE^{\mathrm{t}}\right). \tag{51}$$

The partial derivatives of Π can then therefore be expressed as follows

$$\Pi_\rho = P_\rho + P_e e_\rho, \qquad \Pi_{m_i} = P_e e_{m_i}, \qquad \Pi_{E^{\mathrm{t}}} = P_e e_{E^{\mathrm{t}}}. \tag{52}$$

Using the definition of the specific internal energy as a function of the conserved variables, $e = e\,(\rho, \mathbf{m}, E^{\mathrm{t}}) = E^{\mathrm{t}}/\rho - \frac{1}{2}\|\mathbf{m}\|^2/\rho^2$, it is possible to express its partial derivatives as

$$e_\rho = -\frac{1}{\rho}\left(e - \frac{1}{2}\|\mathbf{v}\|^2\right), \qquad e_{m_i} = -\frac{v_i}{\rho}, \qquad e_{E^{\mathrm{t}}} = \frac{1}{\rho}. \tag{53}$$

The derivatives of Π can now be re-written as

$$\Pi_\rho = \alpha - \frac{e}{\rho}\beta + \frac{1}{2}\frac{\beta}{\rho}\|\mathbf{v}\|^2, \qquad \Pi_{m_i} = -\frac{v_i}{\rho}\beta, \qquad \Pi_{E^{\mathrm{t}}} = \frac{\beta}{\rho}, \tag{54}$$

where

$$\alpha = \frac{\partial P(\rho, e)}{\partial \rho} \qquad \text{and} \qquad \beta = \frac{\partial P(\rho, e)}{\partial e}. \tag{55}$$

A.2 Exact solution of the Riemann problem for a real gas

Referring to Quartapelle *et al.* [73], the one-dimensional Riemann problem of gasdynamics can be formulated as follows

$$\begin{cases} u_1(T_1; \mathbf{L}) - u_3(T_3; \mathbf{R}) = 0, \\ P_1(T_1; \mathbf{L}) - P_3(T_3; \mathbf{R}) = 0, \end{cases} \tag{56}$$

where **L** and **R** indicate the initial left and right state, respectively. The subscripts $_{1,3}$ denote the two *genuinely nonlinear* eigenvalues of the Euler equations $\lambda_{1,3} = u \mp c$, while the *linearly degenerate* eigenvalue is $\lambda_2 = u$. Using this convention, the intermediate state $_1$ is bounded by λ_1 and λ_2, while $_3$ by λ_2 and λ_3. The solution of the Riemann problem is obtained imposing the continuity of the velocity and pressure across the contact discontinuity (associated with λ_2). The expressions for these two quantities are obtained integrating the rarefaction fan (if the pressure in the intermediate state is smaller than the one of the corresponding initial state) or solving the Rankine–Hugoniot shock relations

$$u_1(T;\mathrm{L}) \equiv \begin{cases} u_1^{\mathrm{rar}}(T;\mathbf{L}) & \text{if } P(T) < P_{\mathrm{L}}, \\ u_1^{\mathrm{RH}}(T;\mathbf{L}) & \text{if } P(T) > P_{\mathrm{L}}, \end{cases} \tag{57}$$

$$u_3(T;\mathrm{R}) \equiv \begin{cases} u_3^{\mathrm{rar}}(T;\mathbf{R}) & \text{if } P(T) < P_{\mathrm{R}}, \\ u_3^{\mathrm{RH}}(T;\mathbf{R}) & \text{if } P(T) > P_{\mathrm{R}}. \end{cases} \tag{58}$$

The nonlinear system (56) is solved iteratively for the two intermediate temperatures $T_{1,3}$ using the Newton–Raphson method. All the thermodynamic derivatives used for the solution of the rarefaction and shock wave relations, and needed in the definition of the Eq. (56) Jacobian are numerically approximated using centered finite differences. The Newton–Raphson iterations are stopped when the sum of the relative increments for T_1 and T_3 is smaller than 10^{-10}.

References

[1] Clerc, S., 2000. "Numerical simulation of the homogeneous equilibrium model for two-phase flows". *J. Comput. Phys.,* **161**(1), pp. 354–375.

[2] Meng, H., and Yang, V., 2003. "A unified treatment of general fluid thermodynamics and its application to a preconditioning scheme". *J. Comput. Phys.,* **189**(1), pp. 277–304.

[3] Colonna, P., Casati, E., Trapp, C., Mathijssen, T., Larjola, J., Turunen-Saaresti, T., and Uusitalo, A., 2015. "Organic Rankine cycle power systems: From the concept to current technology, applications, and an outlook to the future". *Journal of Engineering for Gas Turbines and Power,* **137**(10), p. 100801.

[4] Thompson, P. A., 1971. "A fundamental derivative in gasdynamics". *Phys. Fluids,* **14**(9), pp. 1843–1849.

[5] Thompson, P., and Lambrakis, K., 1973. "Negative shock waves". *J. Fluid Mech.,* **60**(01), pp. 187–208.

[6] Cramer, M., and Kluwick, A., 1984. "On the propagation of waves exhibiting both positive and negative nonlinearity". *J. Fluid Mech.,* **142**, pp. 9–37. cited By 60.

[7] Schnerr, G., and Leidner, P., 1991. "Diabatic supersonic flows of dense gases". *Phys. Fluids,* **3**(10), pp. 2445–2458.

[8] Cramer, M., Monaco, J., and Fabeny, B., 1994. "Fanno processes in dense gases". *Phys. Fluids,* **6**(2), pp. 674–683.

[9] Monaco, J. F., Cramer, M. S., and Watson, L. T., 1997. "Supersonic flows of dense gases in cascade configurations". *J. Fluid Mech.,* **330**, 0, pp. 31–59.

[10] Brown, B., and Argrow, B., 1997. "Two-dimensional shock tube flow for dense gases". *J. Fluid Mech.,* **349**, pp. 95–115. cited By 13.

[11] Guardone, A., 2007. "Three-dimensional shock tube flows for dense gases". *J. Fluid Mech.,* **583**, pp. 423–442.

[12] Kluwick, A., 2004. "Internal flows of dense gases". *Acta Mech.,* **169**(1-4), pp. 123–143.

[13] Wang, C.-W., and Rusak, Z., 1999. "Numerical studies of transonic bzt gas flows around thin airfoils". *J. Fluid Mech.,* **396**, pp. 109–141.

[14] Cinnella, P., and Congedo, P. M., 2007. "Inviscid and viscous aerodynamics of dense gases". *J. Fluid Mech.,* **580**, pp. 179–217.

[15] Brown, B., and Argrow, B., 2000. "Application of Bethe-Zel'dovich-Thompson fluids in organic Rankine cycle engines". *J. Propul. Power,* **16**(6), pp. 1118–1124. cited By 42.

[16] Boncinelli, P., Rubechini, F., Arnone, A., Cecconi, M., and Cortese, C., 2004. "Real gas effects in turbomachinery flows: A computational fluid dynamics model for fast computations". *J. Turbomach.,* **126**(2), pp. 268–276.

[17] Colonna, P., Harinck, J., Rebay, S., and Guardone, A., 2008. "Real-gas effects in organic Rankine cycle turbine nozzles". *J. Propul. Power,* **24**(2), pp. 282–294.

[18] Harinck, J., Guardone, A., and Colonna, P., 2009. "The influence of molecular complexity on expanding flows of ideal and dense gases". *Phys. Fluids,* **21**(8), p. 086101.

[19] Congedo, P. M., Corre, C., and Cinnella, P., 2011. "Numerical investigation of dense-gas effects in turbomachinery". *Comput. Fluids,* **49**(1), pp. 290–301.

[20] Godunov, S. K., 1959. "A difference scheme for numerical solution of discontinuous solution of hydrodynamic equations". *Matematicheskii Sbornik,* **47**(2), pp. 271–306.

[21] Colella, P., and Glaz, H. M., 1985. "Efficient solution algorithms for the Riemann problem for real gases". *J. Comput. Phys.,* **59**(2), pp. 264–289.

[22] Roe, P. L., 1981. "Approximate Riemann solvers, parameter vectors, and difference schemes". *J. Comput. Phys.,* **43**(2), pp. 357–372.

[23] Glaister, P., 1988. "An approximate linearised Riemann solver for the Euler equations for real gases". *J. Comput. Phys.,* **74**(2), pp. 382–408.

[24] Glaister, P., 1988. "An approximate linearised Riemann solver for the three-dimensional Euler equations for real gases using operator splitting". *J. Comput. Phys.,* **77**(2), pp. 361–383.

[25] Glaister, P., 1994. "An efficient numerical method for compressible flows of a real gas using arithmetic averaging". *Comput. Math. Appl.,* **28**(7), pp. 97–113.

[26] Glaister, P., 1999. "Riemann solvers with primitive parameter vectors for two-dimensional compressible flows of a real gas". *Comput. Math. Appl.,* **37**(2), pp. 75–92.

[27] Montagné, J. L., Yee, H. C., and Vinokur, M., 1989. "Comparative study of high-resolution shock-capturing schemes for a real gas". *AIAA J.,* **27**(10), pp. 1332–1346.

[28] Vinokur, M., and Montagné, J. L., 1990. "Generalized flux-vector splitting and Roe average for an equilibrium real gas". *J. Comput. Phys.,* **89**(2), pp. 276–300.

[29] Buffard, T., Gallouët, T., and Hérard, J. M., 2000. "A sequel to a rough Godunov scheme: application to real gases". *Comput. Fluids,* **29**(7), pp. 813–847.

[30] Gallouët, T., Hérard, J. M., and Seguin, N., 2002. "Some recent finite volume schemes to compute Euler equations using real gas EOS". *Int. J. Numer. Meth. Fl.,* **39**(12), pp. 1073–1138.

[31] Guardone, A., and Vigevano, L., 2002. "Roe linearization for the van der Waals gas". *J. Comput. Phys.,* **175**(1), pp. 50–78.

[32] Mottura, L., Vigevano, L., and Zaccanti, M., 1997. "An evaluation of Roe's scheme generalizations for equilibrium real gas flows". *J. Comput. Phys.,* **138**(2), pp. 354–399.

[33] Colonna, P., and Rebay, S., 2004. "Numerical simulation of dense gas flows on unstructured grids with an implicit high resolution upwind Euler solver". *Int. J. Numer. Meth. Fl.,* **46**(7), pp. 735–765.

[34] Cinnella, P., and Congedo, P., 2005. "Numerical solver for dense gas flows". *AIAA J.,* **43**(11), Nov., pp. 2457–2461.

[35] Cinnella, P., 2006. "Roe-type schemes for dense gas flow computations". *Comput. Fluids,* **35**(10), pp. 1264–1281.

[36] Cirri, M., Adami, P., and Martelli, F., 2005. "Development of a CFD real gas flow solver for hybrid grid". *Int. J. Numer. Meth. Fl.,* **47**(8-9), pp. 931–938.

[37] Steger, J. L., and Warming, R. F., 1981. "Flux vector splitting of the inviscid gas-dynamic equations with application to finite-difference methods". *J. Comput. Phys.,* **40**(2), pp. 263–293.

[38] van Leer, B., 1982. "Flux-vector splitting for the Euler equations". Vol. 170, pp. 507–512.

[39] Osher, S., 1981. "Numerical solution of singular perturbation problems and hyperbolic systems of conservation laws". *North-Holland Mathematics Studies,* **47**(C), pp. 179–204.

[40] Liou, M. S., 1996. "A sequel to AUSM: AUSM$^+$". *J. Comput. Phys.,* **129**(2), pp. 364–382.

[41] Liou, M. S., van Leer, B., and Shuen, J. S., 1990. "Splitting of inviscid fluxes for real gases". *J. Comput. Phys.,* **87**(1), pp. 1–24.

[42] Suresh, A., and Liou, M. S., 1991. "Osher's scheme for real gases". *AIAA J.,* **29**(6), pp. 920–926.

[43] Edwards, J. R., Franklin, R. K., and Liou, M. S., 2000. "Low-diffusion flux-splitting methods for real fluid flows with phase transitions". *AIAA J.,* **38**(9), pp. 1624–1633.

[44] Edwards, J. R., 2001. "Towards unified CFD simulation of real fluid flows". *AIAA Paper,* **2524**(416), pp. 1–13.

[45] Saurel, R., Larini, M., and Loraud, J. C., 1994. "Exact and approximate Riemann solvers for real gases". *J. Comput. Phys.,* **112**(1), pp. 126–137.

[46] Merkle, C. L., Sullivan, J. Y., Buelow, P. E. O., and Venkateswaran, S., 1998. "Computation of flows with arbitrary equations of state". *AIAA J.,* **36**(4), pp. 515–521.

[47] Toro, E. F., Spruce, M., and Speares, W., 1994. "Restoration of the contact surface in the HLL-Riemann solver". *Shock Waves,* **4**(1), pp. 25–34.

[48] Kurganov, A., and Tadmor, E., 2000. "New high-resolution central schemes for nonlinear conservation laws and convection-diffusion equations". *J. Comput. Phys.,* **160**(1), pp. 241–282.

[49] Pulliam, T. H., and Steger, J. L., 1985. "Recent improvements in efficiency, accuracy, and convergence for implicit approximate factorization algorithms".

[50] Span, R., and Wagner, W., 2003. "Equations of state for technical applications. I. Simultaneously optimized functional forms for nonpolar and polar fluids". *Int. J. Thermophys.,* **24**(1), pp. 1–39.

[51] Span, R., and Wagner, W., 2003. "Equations of state for technical applications. II. Results for nonpolar fluids". *Int. J. Thermophys.,* **24**(1), pp. 41–109.

[52] Lemmon, E. W., McLinden, M. O., and Huber, M. L., 2002. NIST standard reference database 23: Reference fluid thermodynamic and transport properties-REFPROP, version 8.0. Tech. rep., National Institute of Standards and Technology, Standard Reference Data Program, Gaithersburg.

[53] Berrut, J. P., and Trefethen, L. N., 2004. "Barycentric Lagrange interpolation". *SIAM Rev.,* **46**(3), pp. 501–517.

[54] van der Stelt, T. P., Nannan, N. R., and Colonna, P., 2012. "The iPRSV equation of state". *Fluid Phase Equilib.,* **330**(0), pp. 24 – 35.

[55] Span, R., and Wagner, W., 1996. "A new equation of state for carbon dioxide covering the fluid region from the triplepoint temperature to 1100 K at pressures up to 800 MPa". *J. Phys. Chem. Ref. Data,* **25**(6), pp. 1509–1596.

[56] Batten, P., Leschziner, M. A., and Goldberg, U. C., 1997. "Average-state Jacobians and implicit methods for compressible viscous and turbulent flows". *J. Comput. Phys.,* **137**(1), pp. 38–78.

[57] Einfeldt, B., Munz, C. D., Roe, P. L., and Sjögreen, B., 1991. "On Godunov-type methods near low densities". *J. Comput. Phys.,* **92**(2), pp. 273–295.

[58] Batten, P., Clarke, N., Lambert, C., and Causon, D. M., 1997. "On the choice of wavespeeds for the HLLC Riemann solver". *SIAM J. Sci. Comput.,* **18**(6), pp. 1553–1570.

[59] Kurganov, A., and Petrova, G., 2000. "Central schemes and contact discontinuities". *ESAIM Math. Model. Num.,* **34**(6), pp. 1259–1275.

[60] Kurganov, A., Noelle, S., and Petrova, G., 2002. "Semidiscrete central-upwind schemes for hyperbolic conservation laws and Hamilton-Jacobi equations". *SIAM J. Sci. Comput.,* **23**(3), pp. 707–740.

[61] Kurganov, A., and Lin, C. T., 2007. "On the reduction of numerical dissipation in central-upwind schemes". *Commun. Comput. Phys.,* **2**(1), pp. 141–163.

[62] Kim, S.-E., Makarov, B., and Caraeni, D., 2003. "A multi-dimensional linear reconstruction scheme for arbitrary unstructured grids". *AIAA paper,* **3990**, p. 2003.

[63] Ham, F., and Iaccarino, G., 2004. Energy conservation in collocated discretization schemes on unstructured meshes. Annual Research Briefs 2004, Center for Turbulence Research, NASA Ames/Stanford University, CA, Dec.

[64] Pecnik, R., Terrapon, V. E., Ham, F., Iaccarino, G., and Pitsch, H., 2012. "Reynolds-averaged Navier-Stokes simulations of the HyShot II scramjet". *AIAA J.,* **50**(8), pp. 1717–1732.

[65] Shu, C. W., and Osher, S., 1988. "Efficient implementation of essentially non-oscillatory shock-capturing schemes". *J. Comput. Phys.,* **77**(2), pp. 439–471.

[66] Satish, B., Buschelman, K., Eijkhout, V., Gropp, W. D., Kaushik, D., Knepley, M. G., McInnes, L. C., Smith, B. F., and Zhang, H., 2009. "PETSc Web page, http://www.mcs.anl.gov/petsc".

[67] Saad, Y., and Schultz, M., 1986. "GMRES: A generalized minimal residual algorithm for solving nonsymmetric linear systems". *SIAM J. Sci. Stat. Comp.,* **7**(3), pp. 856–869.

[68] Colonna, P., van der Stelt, T. P., and Guardone, A., 2012. FluidProp (Version 3.0): A program for the estimation of thermophysical properties of fluids. A program since 2004.

[69] Clerc, S., 1999. "Accurate computation of contact discontinuities in flows with general equations of state". *Comput. Method. Appl. M.,* **178**(3-4), pp. 245–255.

[70] Dwight, R. P., and Brezillon, J., 2006. "Effect of approximations of the discrete adjoint on gradient-based optimization". *AIAA J.,* **44**(12), pp. 3022–3031.

[71] Carpentieri, G., Koren, B., and van Tooren, M. J. L., 2007. "Adjoint-based aerodynamic shape optimization on unstructured meshes". *J. Comput. Phys.,* **224**(1), pp. 267–287.

[72] Spalart, P. R., and Allmaras, S. R., 1994. "One-equation turbulence model for aerodynamic flows". *Rech. Aerospatiale*(1), pp. 5–21.

[73] Quartapelle, L., Castelletti, L., Guardone, A., and Quaranta, G., 2003. "Solution of the Riemann problem of classical gasdynamics". *J. Comput. Phys.,* **190**(1), pp. 118–140.

3

Flux-conserving treatment of non-conformal interfaces for finite-volume discretization of conservation laws

The contents of this chapter appeared in:

Rinaldi, E., Colonna, P., and Pecnik, R., 2015. *Comp. Fluids*, **120**, pp. 126–139.

Abstract *We present a new flux-conserving treatment of non-conformal mesh block interfaces for the numerical solution of conservation laws by high order finite volumes schemes. An auxiliary mesh is used at the interface to establish a connectivity between non-conformal blocks. The method does not involve any flux interpolation and conservation is therefore guaranteed by construction, without enforcing additional constraints. Additionally, several gradient reconstructions across the interface have been adapted and their order of accuracy is studied analytically and numerically. Applications to two and three dimensional fluid dynamic problems are considered, and the verification of the method is provided by comparing solutions obtained on single-block grids with no interfaces. Also the accuracy and numerical stability of the interface treatment is demonstrated empirically for a variety of test cases, such as a cylinder in supersonic cross-flow, low Mach-number vortex shedding, and a transonic turbine stage. The exemplary flow simulation problems are solved using explicit and implicit time integration schemes. The obtained results successfully demonstrate the effectiveness of the proposed method for stationary non-conformal blocks domains, as well as for mesh blocks in relative motion.*

3.1 Introduction

The numerical discretization of complex geometries is a challenging task which often requires the generation of unstructured or multi-block grids in order to guarantee a high quality of the resulting computational domain. Node-to-node connectivity among the discrete elements is required by standard numerical techniques and is guaranteed by most algorithms for mesh generation. However, there are applications for which the grid must be split into subregions, or patches, with non-matching interface boundaries. Typical examples are found in aeroelasticity simulations, where the aerodynamic and structural interface nodes often do not coincide, or multiphysics simulations. A similar situation occurs when parts of the domain are in relative motions with respect to each other, as it is the case for turbomachinery computations.

The appropriate treatment of the artificially introduced internal boundaries is crucial. The most critical aspects such a treatment has to comply with are: numerical conservation, stability, accuracy and efficiency. In general, the methods can be categorized based on their numerical conservation properties, namely they can be subdivided in conservative and non-conservative schemes.

Berger[1] was among the first to propose a method to conserve variables at grid interfaces. Rai[2–4] developed a conservative zonal-boundary scheme for grids having a common cell-centered line at the interface, which was later applied to study the two-dimensional stator/rotor interaction of an axial turbine stage[5]. Lerat and Wu[6] proposed a patched grid technique based on a common cell-side line instead. Interface cell faces are sub-divided into smaller segments on which the fluxes are calculated and then summed together in order to obtain the total numerical flux, thus avoiding any interpolation. Lerat and Wu's method was later successfully applied by Benkenida *et al.*[7] to calculate transport of vortices. Zhang *et al.*[8] proposed instead a polynomial remapping of the variables on the non-matching faces, enforcing conservation in the definition of the polynomials co-

efficients. An alternative approach which ensures conservation is obtained by introducing a local mesh at the boundary between domains, whose purpose is to correctly "attach" the non-conformal patches, documented in Refs.[9–11], where CFD applications are treated, and in Refs.[12,13], which in turn are concerned with multiphysics simulations.

Non-conservative schemes suffer from possible loss of accuracy and stability issues, especially when discontinuities, e.g., shock waves, occur across the interface. One of the most widely used non-conservative scheme is the CHIMERA interpolation technique on overlapping grids in its original formulation[14,15]. As acknowledged by the authors, problems were encountered in case of shock/interface interaction. Wang[16] extended the scheme to a conservative formulation which replaces the overlapped zones by patched zones. Another modification to the original CHIMERA method is the one proposed by Kao and Liou[17]: they replaced the grid overlapping with a newly defined unstructured grid. The conservation error for the CHIMERA scheme was analyzed by Wang *et al.*[18], who showed that it is a first order term of the mesh elements size if a second order conservative scheme is used, and if discontinuities are not in the proximity of the overlapping area interface. In addition, they also showed that the non-conservative formulation might cause inaccurate solutions for smooth flows too, and pointed to the benefits of using a conservative formulation. Overlapping grids were also considered by Liu[19], who extended the central scheme of Kurganov and Tadmor[20] to account for the new mesh topology. Other alternative non-conservative interface methods were successfully applied to CFD calculations on complex geometries such as a complete aircraft configuration[21,22]. Tang and Zhou[23] rigorously investigated the convergence and accuracy of non-conservative schemes showing that the conservation error is bounded if the solution itself is bounded.

This paper presents a new flux-conserving treatment of non-conformal interfaces for the numerical solution of conservation laws by high order finite volumes schemes. The method is based on the concept of a supermesh introduced by Farrell *et al.*[24] and later applied to the conservative interpolation of cell-centered finite volume variables by Menon and Schmidt[25]. The supermesh acts as an auxiliary interface grid that establishes connectivity between the mesh blocks. The numerical fluxes are evaluated on the supermesh and then summed to the flux balance of the control volumes of their respective parent meshes.

Section 3.2 introduces the supermesh and describes its construction. The flux assembly technique for the internal control volumes and at the interface is described in Sec. 3.3. The method automatically guarantees flux conservation by construction, without any interpolation or the need to enforce additional constraints. The challenge of an accurate gradient reconstruction at the interface control volumes, which is needed for high order spatial accuracy, is addressed in Sec. 3.4. Modifications to the least-squares and Green–Gauss methods are proposed, and their order of accuracy is derived analytically and verified numerically on two and three dimensional domains. The parallelization of the supermesh generation and of the interface treatment is discussed in Sec. 3.5. The verification of the proposed interface treatment is provided by solving the Navier–Stokes equations. Several two and three dimensional numerical tests are presented and discussed in Sec. 3.6. Numerical stability is shown empirically using explicit and implicit time integration schemes. Finally, conclusions are drawn in Sec. 3.7.

3.2 Non-conformal mesh interface treatment using a supermesh

3.2.1 Supermesh definition

The auxiliary grid between two non-conformal mesh blocks, as displayed in Fig. 3.1, is constructed using the supermesh methodology. The most important properties of the supermesh, as described in Refs.[24,25], are reported in the following for the sake of completeness. Let $\mathcal{M}_A$ and $\mathcal{M}_B$ be two arbitrary surface meshes of the same geometrical domain $\Omega \subset \Re^3$. They will be referred to as *parent* meshes. $\mathcal{N}_A$ and $\mathcal{N}_B$ are the nodes of $\mathcal{M}_A$ and $\mathcal{M}_B$, respectively, and $\mathcal{E}_A$ and $\mathcal{E}_B$ the elements (faces in this case) of the two meshes.

Definition 1. A supermesh $\mathcal{M}_S$ of $\{\mathcal{M}_A, \mathcal{M}_B\}$ is a mesh of Ω which satisfies the following properties:

- $\mathcal{N}_S \supseteq \mathcal{N}_A \cup \mathcal{N}_B$;
- $A(\mathcal{E}_S \cap \mathcal{E}) \in \{0, A(\mathcal{E}_S)\} \;\forall\, \mathcal{E}_S \in \mathcal{M}_S,\ \mathcal{E} \in \mathcal{M},\ \mathcal{M} \in \{\mathcal{M}_A, \mathcal{M}_B\}$;

where A is the surface area function. ■

The first property asserts that the supermesh contains every node of the parent meshes. The second asserts that the intersection area of each element of the supermesh $\mathcal{E}_S$ with any element of a parent mesh must either be null or measure the whole supermesh element area $A(\mathcal{E}_S)$. In other words, it is possible to reconstruct every element of a parent mesh using an appropriate number of supermesh elements.

3.2.2 Supermesh construction

The supermesh construction consists of an intersection problem between $n-1$ dimensional elements, where n is the number of dimensions of the grid blocks. The task is trivial in case of 2D meshes, whereby the supermesh is made of segments demarcated by the set of nodes $\mathcal{N}_S$, which coincides with $\mathcal{N}_A \cup \mathcal{N}_B$. This is valid for every 1D intersection problem, as depicted in Fig. 3.1(a).

In case of 3D mesh blocks, the supermesh definition consists of a 2D face intersection problem between two interface surface meshes. Figure 3.1(b) shows a three-dimensional mesh consisting of two blocks with non-conformal interface elements. $\mathcal{M}_A$ and $\mathcal{M}_B$ are the surface meshes on the patched boundary faces. Unstructured quadrilateral and triangular elements are used on $\mathcal{M}_A$ and $\mathcal{M}_B$, respectively. $\mathcal{M}_S$ denotes the interface supermesh, which is an hybrid unstructured grid.

In order to satisfy the properties of Definition 1 (discussed in Sec. 3.2.1) and guarantee flux-conservation across the interface, it is crucial that the intersection scheme used to calculate $\mathcal{M}_S$ is accurate and robust. Exact numerical conservation can only be achieved if the intersection is computed to machine precision. The algorithm used in this study to calculate the intersection between two generic parent mesh elements, $\mathcal{E}_{A,i}$ and $\mathcal{E}_{B,j}$, is described graphically in Fig. 3.2 and consists of four steps:

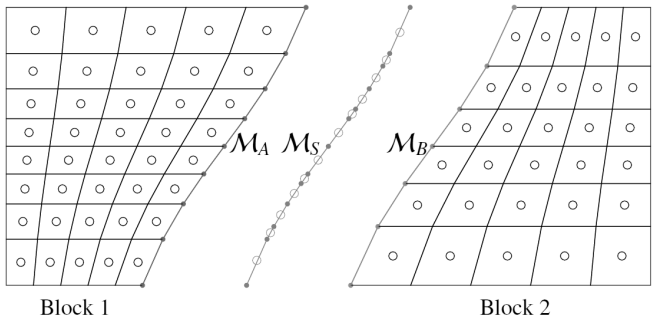

(a) 2D mesh blocks, 1D parent meshes interpolation. Empty circles indicate the cell centers of the elements, while the black circles denote $\mathcal{N}_S$.

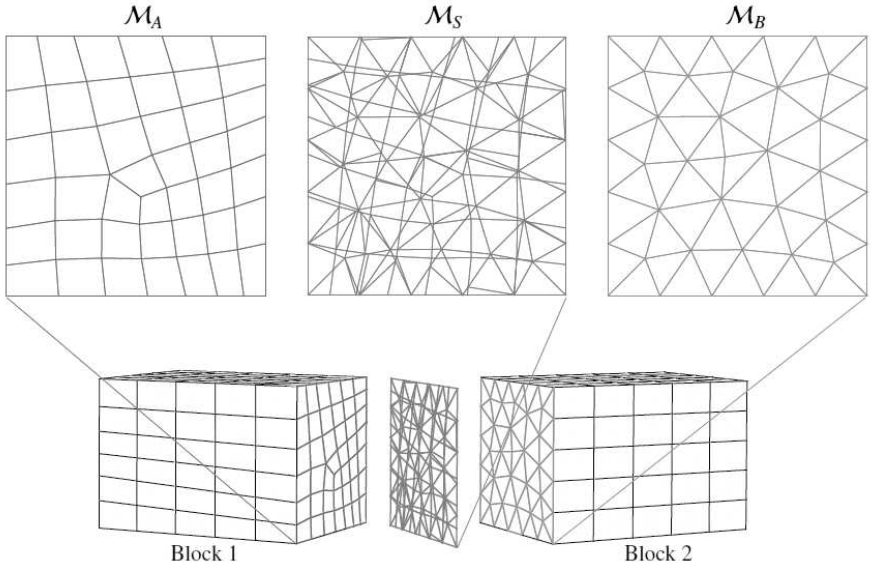

(b) 3D mesh blocks, 2D parent meshes and interpolation.

Figure 3.1: Interface supermesh definition for 2D and 3D parent grids. In both cases the mesh blocks are displaced for the sake of clarity and the interface supermesh is displayed in the middle.

1. identify the vertices of $\mathcal{E}_{A,i}$ contained within $\mathcal{E}_{B,j}$, and vice versa;
2. calculate the intersection between the edges of $\mathcal{E}_{A,i}$ and $\mathcal{E}_{B,j}$;
3. remove double points from step 1 and 2;
4. if the number of calculated nodes ($\mathcal{N}_{S,ij}$) after step 3 is larger than 2, define new supermesh elements.

At step 3, two nodes N_1 and N_2 are considered to coincide if $|\mathbf{x}_{N_1} - \mathbf{x}_{N_2}| < 10^{-14}$. Step 3 addresses all the special situations stemming from coincidental nodes or edges. In general, the intersection procedure may lead to small elements of size comparable to machine precision, which however does not pose any limitations in the flux calculation and in the choice of the time-step, the latter being computed using the volume of the mesh cells of the original blocks.

Several exemplary face intersections are shown in Fig. 3.3 in order to characterize common situations usually encountered. If $\mathcal{N}_{S,ij} = 3$ the supermesh element $\mathcal{E}_{S,k}$ is a triangle, Fig. 3.3(a), while if $\mathcal{N}_{S,ij} = 4$, $\mathcal{E}_{S,k}$ is a quadrilateral element, Fig. 3.3(b). The situation in which the calculated supermesh element $\mathcal{E}_{S,k}$ coincides either with $\mathcal{E}_{B,j}$ or with $\mathcal{E}_{A,i}$ is depicted in Fig. 3.3(c) and 3.3(d), respectively. Finally, if $\mathcal{N}_{S,ij} > 4$, multiple elements are defined, Fig. 3.3(e) and 3.3(f). In order to keep the number of supermesh elements to a minimum, it is convenient to define as many quadrilateral elements as possible at each face intersection, to limit the use of triangular elements when an odd number of nodes is available.

The intersection procedure discussed can be generalized to an arbitrary surface mesh, not necessarily planar as in Fig. 3.1(b), by parametrizing the parent meshes using a common local coordinate system, and by computing the intersections in the local frame of reference.

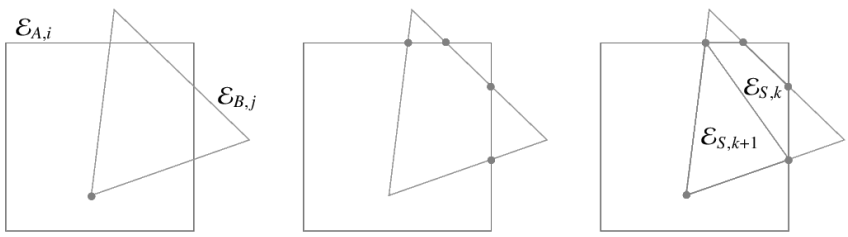

Figure 3.2: Necessary steps to calculate supermesh elements by intersecting two generic elements $\mathcal{E}_{A,i}$ and $\mathcal{E}_{B,j}$.

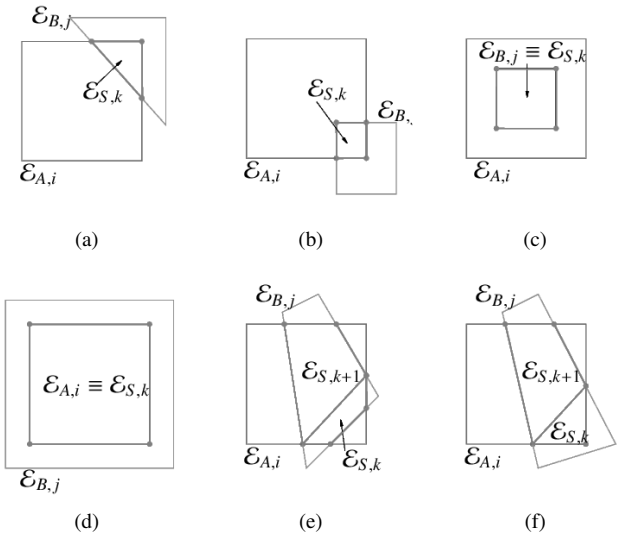

Figure 3.3: Exemplary intersections of 2D elements.

3.3 Conservative flux assembly at the interface

In this work we consider finite volume integration scheme for conservation laws written as

$$\frac{\partial}{\partial t}\int_{\Omega}\mathbf{U}d\Omega + \int_{\partial\Omega}\mathbf{F}\left(\mathbf{U}\right)dA = \mathbf{0}, \tag{3.1}$$

where $\mathbf{U}$ is the vector of the conservative variables and $\mathbf{F}(\mathbf{U})$ the flux vector, which is in general a non-linear function of $\mathbf{U}$. The physical domain of interest is denoted by Ω and its external boundary by $\partial\Omega$. In the finite-volume framework, Ω is discretized numerically into control volumes whose total number is indicated by N_{cv}. Equation (3.1) can be re-written in the semi-discrete form in the cell center of each control volume cv as

$$\frac{\partial \mathbf{U}_{cv}}{\partial t} = -\mathbf{RHS}(\mathbf{U}_{cv}), \tag{3.2}$$

where the discretized flux balance is casted to the right-hand-side (**RHS**) of the equations as

$$\mathbf{RHS}(\mathbf{U}_{cv}) = -\frac{1}{V_{cv}}\sum_{fa=1}^{N_{fa}}\mathbf{F}(\mathbf{U}_L,\mathbf{U}_R)A_{fa} - \frac{1}{V_{cv}}\sum_{fa=1}^{N_{bfa}}\mathbf{F}(\mathbf{U}_L,\mathbf{U}_{bc})A_{fa}. \tag{3.3}$$

The nomenclature used in Eq. (3.3) is displayed in Fig. 3.4. Here, V_{cv} indicates the volume of cv and N_{fa} and N_{bfa} the number of discrete faces defining the control volume, which

can be either internal or on the boundary of the domain (N_{bfa}). A_{fa} denotes the area of the face fa. The value of the face flux depends on the conservative variable states on the left and on the right side of the face, $\mathbf{U}_L$ and $\mathbf{U}_R$, and is considered positive if it points outwards of the control volume. A first order accurate scheme is obtained if $\mathbf{U}_L$ and $\mathbf{U}_R$ are assumed equal to the values in the cell centers of the respective control volumes, namely if $\mathbf{U}_L = \mathbf{U}_{cv}$ and $\mathbf{U}_R = \mathbf{U}_{nb}$, where nb indicates the neighbor of cv sharing the face fa on which the flux is calculated. The total number of internal neighbors for each cv is denoted by N_{nb} and satisfies $N_{nb} = N_{fa} - N_{bfa}$. In case one of the faces is a boundary face, the boundary condition $\mathbf{U}_{bc}$ is used in the flux calculation.

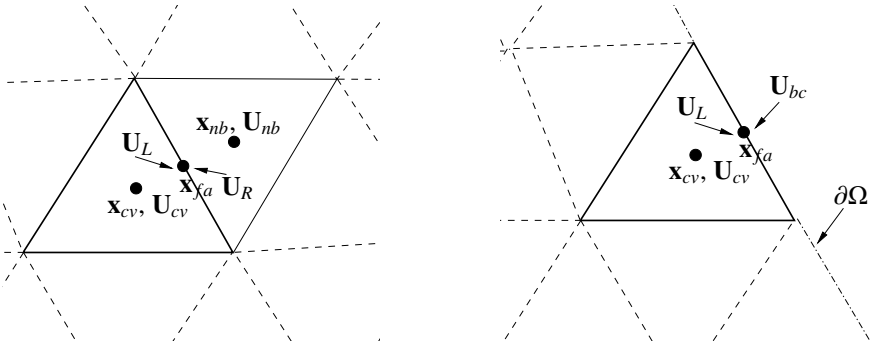

(a) Internal cell ($N_{fa} = 3$). (b) Boundary cell ($N_{fa} = 2$ and $N_{bfa} = 1$).

Figure 3.4: Schematic of the finite volume discretization.

The proposed interface treatment uses the supermesh to replace the parent meshes $\mathcal{M}_A$ and $\mathcal{M}_B$ in the flux balance calculation of the interface control volumes. At each $\mathcal{E}_S$, the left and right states used to evaluate the supermesh face flux are taken from the corresponding $\mathcal{E}_A$ and $\mathcal{E}_B$. To this end, it is necessary to map the supermesh on the parent meshes. For every $\mathcal{E}_S$, $\mathcal{T}_A$ and $\mathcal{T}_B$ contain the index of the parent mesh control volume, such that

$$\mathcal{T}_{A,i} = \mathcal{P}(k) \qquad \text{if} \qquad A\left(\mathcal{E}_{S,i} \cap \mathcal{E}_{A,k}\right) = A\left(\mathcal{E}_{S,i}\right), \tag{3.4}$$

$$\mathcal{T}_{B,i} = \mathcal{P}(k) \qquad \text{if} \qquad A\left(\mathcal{E}_{S,i} \cap \mathcal{E}_{B,k}\right) = A\left(\mathcal{E}_{S,i}\right), \tag{3.5}$$

where i and k indicate the index of a generic supermesh and parent mesh element, respectively. $\mathcal{P}(k)$ returns the index of the control volume cv, which contains the boundary face k. The flux balance for an interface control volume belonging to $\mathcal{M}_A$ on a two-dimensional structured grid is illustrated in Fig. 3.5. The fluxes computed on the supermesh faces contribute to the flux balance as

$$\mathbf{RHS}_{int}(\mathbf{U}_{cv}) = \mathbf{RHS}(\mathbf{U}_{cv}) - \frac{1}{V_{cv}} \sum_{sf=1}^{N_{sf}} \mathbf{F}\left(\mathbf{U}_{cv}, \mathbf{U}_{\mathcal{T}_{B,sf}}\right) A_{sf}, \tag{3.6}$$

where N_{sf} is the number of supermesh elements that are mapped on cv (for $cv = 6$ they are two, indicated by the indices 9 and 10), and A_{sf} is the area of the single supermesh

face. The same formula is applied to a control volume contained in $\mathcal{M}_B$ by replacing $\mathcal{T}_{B,sf}$ with $\mathcal{T}_{A,sf}$. The flux integral conservation over the whole interface is guaranteed by the second property of Definition 1, provided that the interpolation method is accurate to machine precision.

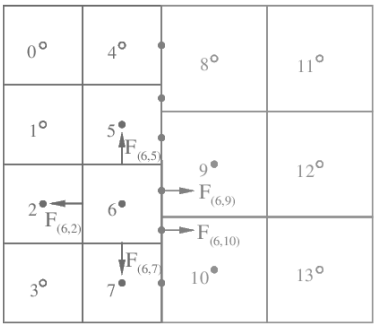

Figure 3.5: Schematic showing the flux balance calculation for the interface control volume $cv = 6$. For the case displayed $\mathcal{T}_A = (4, 5, 5, 6, 6, 7)$ and $\mathcal{T}_B = (8, 8, 9, 9, 10, 10)$, thus the neighbors of cv that contribute to the flux balance calculation are $nb = (7, 2, 5, 9, 10)$.

3.4 Interface gradient reconstruction

In order to achieve second or higher order spatial accuracy, the states are extrapolated from the cell centers to the faces using an appropriate gradient reconstruction scheme. Let us consider the exemplary unstructured mesh depicted in Fig. 3.4; a generic scalar quantity ϕ is calculated at a cell face as

$$\phi_{fa} = \phi_{cv} + \psi_{cv} \nabla\phi_{cv} \cdot \left(\mathbf{x}_{fa} - \mathbf{x}_{cv}\right), \tag{3.7}$$

whereby $\nabla\phi_{cv} = (\partial_x\phi_{cv}, \partial_y\phi_{cv}, \partial_z\phi_{cv})$ is the gradient of the scalar in the cell center, and the partial derivatives are written in the compact form $\partial_x = \partial/\partial x$, $\partial_y = \partial/\partial y$, $\partial_z = \partial/\partial z$. The location of the face and control volume centroids are denoted by $\mathbf{x}_{fa}$ and $\mathbf{x}_{cv}$, respectively, and ψ_{cv} is a slope limiter function which prevents spurious oscillations in the regions where ϕ varies sharply. The number of control volumes used to approximate the gradient at each grid cell center is referred to as *stencil* and depends on the order of accuracy of the scheme and on the scheme itself. In this paper, we consider second order methods only and we limit our discussion to the least-squares (LS) and Green–Gauss (GG) gradient reconstruction schemes.

In the following, we analyze the LS and GG methods as formulated on the internal cells of the computational domain, and we discuss their modification to be adapted to the interface problem. We make use of structured mesh blocks to describe the schemes

and to study their order of accuracy. The reasons for choosing two structured blocks are to simplify the analytical analysis of the order of accuracy (presented in Sec. 3.4.3), and to prevent the numerical results of Sec. 3.4.4 from being polluted by the quality of the internal control volumes. Hereafter, we will refer to the structured grid blocks depicted in Fig. 3.6. In order to be consistent with the equations introduced in Sec. 3.3, the naming of the elements is the same as the one adopted for the unstructured grids.

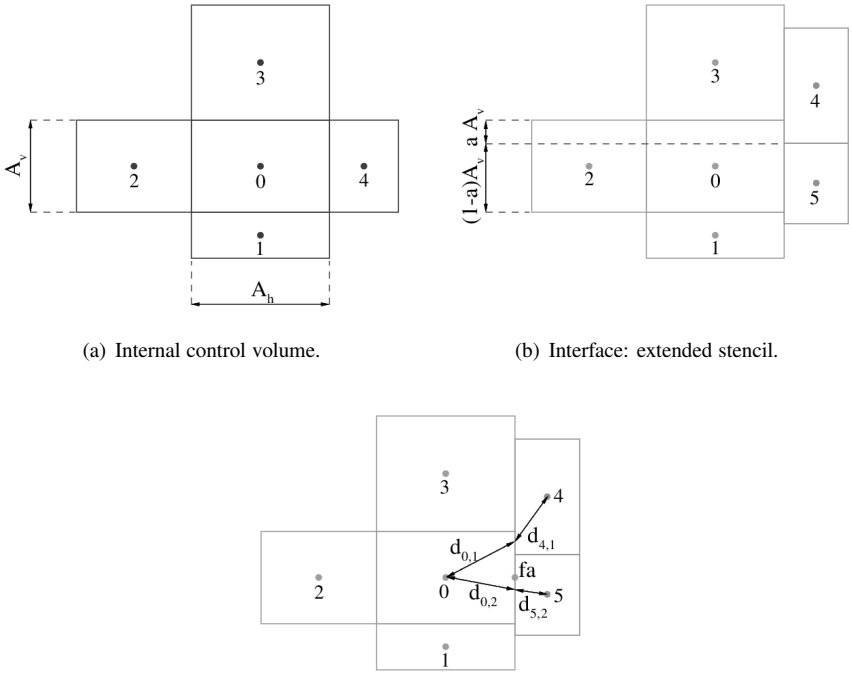

(a) Internal control volume.

(b) Interface: extended stencil.

(c) Interface: face value.

Figure 3.6: Stencil for the least-squares and Green–Gauss gradient reconstruction in the cell centroid $cv = 0$.

3.4.1 Least-squares gradient

The LS method approximates the gradient in the center of a control volume by minimizing an objective function in the form (see e.g. Mavriplis [26])

$$J = \sum_{nb=1}^{N_{nb}} w_{nb}^2 E_{nb}^2, \tag{3.8}$$

where $w_{nb}^2 = 1/|\mathbf{x}_{nb} - \mathbf{x}_{cv}|^2$ and E_{nb} denotes the error

$$E_{nb}^2 = \left(-(\phi_{nb} - \phi_{cv}) + \partial_x\phi_{cv}(x_{nb} - x_{cv}) + \partial_y\phi_{cv}(y_{nb} - y_{cv}) + \partial_z\phi_{cv}(z_{nb} - z_{cv})\right)^2. \quad (3.9)$$

The minimization of Eq. (3.8) leads to

$$\begin{pmatrix} \partial_x\phi_{cv} \\ \partial_y\phi_{cv} \\ \partial_z\phi_{cv} \end{pmatrix} = \begin{pmatrix} S_{w^2dx^2} & S_{w^2dxdy} & S_{w^2dxdz} \\ S_{w^2dxdy} & S_{w^2dy^2} & S_{w^2dydz} \\ S_{w^2dxdz} & S_{w^2dydz} & S_{w^2dz^2} \end{pmatrix}^{-1} \begin{pmatrix} \sum_{nb=1}^{Nnb} w_{nb}^2(x_{nb} - x_{cv})(\phi_{nb} - \phi_{cv}) \\ \sum_{nb=1}^{Nnb} w_{nb}^2(y_{nb} - y_{cv})(\phi_{nb} - \phi_{cv}) \\ \sum_{nb=1}^{Nnb} w_{nb}^2(z_{nb} - z_{cv})(\phi_{nb} - \phi_{cv}) \end{pmatrix}. \quad (3.10)$$

The coefficients of the matrix depend on the geometry of the mesh only, and can be efficiently calculated and stored in a pre-processing step. They are defined as

$$S_{w^2dxdy} = \sum_{nb=1}^{Nnb} w_{nb}^2(x_{nb} - x_{cv})(y_{nb} - y_{cv}), \quad (3.11)$$

and similarly for $S_{w^2dx^2}$, $S_{w^2dy^2}$, and $S_{w^2dz^2}$, S_{w^2dxdz}, and S_{w^2dydz}.

In case at least one of the faces enclosing cv is part of $\partial\Omega$, the contribution of the boundary faces must be included in the objective function, as

$$J = \sum_{nb=1}^{N_{nb}} w_{nb}^2 E_{nb}^2 + \sum_{fa=1}^{N_{bfa}} w_{fa}^2 E_{fa}^2, \quad (3.12)$$

with $w_{fa}^2 = 1/|\mathbf{x}_{fa} - \mathbf{x}_{cv}|^2$, and

$$E_{fa}^2 = \left(-(\phi_{fa} - \phi_{cv}) + \partial_x\phi_{cv}(x_{fa} - x_{cv}) + \partial_y\phi_{cv}(y_{fa} - y_{cv}) + \partial_z\phi_{cv}(z_{fa} - z_{cv})\right)^2. \quad (3.13)$$

The values of the scalar on the external faces are specified as boundary conditions. The minimization of Eq. (3.12) results in an expression for $\nabla\phi_{cv}$ similar to Eq. (3.10).

3.4.1.1 Extended stencil

An intuitive possibility is to extend the list of neighbors of a generic control volume cv by adding neighbors across the interface that share a face in the supermesh, and to make use of Eq. (3.10) with the updated connectivity (LSI-F). A generic cv in the mesh patch containing $\mathcal{M}_A$ has a number of new neighbors which corresponds to the number of supermesh elements satisfying $\mathcal{T}_{A,i} = cv$. The index which identifies the new neighbor belonging to the mesh patch containing $\mathcal{M}_B$ is given by $\mathcal{T}_{B,i}$.

Figure 3.6(b) shows the extended stencil for the interface control volume contained in $\mathcal{M}_A$ on a structured mesh; the cells 4 and 5 are added to the list $nb = 1, 2, 3$. Although, the two mesh blocks are both structured cartesian grids, the interface stencil is skewed due to the non-conformity of the grids, resembling the typical stencil used on an unstructured mesh. In case the elements of $\mathcal{M}_B$ are much smaller than the ones of $\mathcal{M}_A$, the stencil is strongly biased toward $\mathcal{M}_B$. This leads to a deterioration of the gradient accuracy not only along the direction which crosses the interface, but also along the direction parallel to it. To avoid this biasing, only the closest neighbor can be considered (LSI-C).

3.4.1.2 Approximate face value

An alternative approach consists of treating the faces of the control volume on the interface as external boundary faces whose value is computed as

$$\phi_{fa} = \frac{1}{A(\mathcal{E}_{A,k})} \sum_{i:\mathcal{T}_{A,i}=cv} A(\mathcal{E}_{S,i}) \frac{\phi_{cv} d_{\mathcal{T}_{B,i}} + \phi_{\mathcal{T}_{B,i}} d_{cv,i}}{d_{cv,i} + d_{\mathcal{T}_{B,i}}}, \tag{3.14}$$

where $\mathcal{E}_{A,k}$ is the k-th element of the parent mesh $\mathcal{M}_A$, which corresponds to the boundary face fa of cv on the interface. This approach will be referred to as LSI-Fa in the following. Note that $\sum_{i:\mathcal{T}_{A,i}=cv} A(\mathcal{E}_{S,i}) = A(\mathcal{E}_{A,k})$ by definition. $d_{cv,i}$ and $d_{\mathcal{T}_{B,i}}$ denote the distances between the face centers of the supermesh elements i and the cell centers of cv and $T_{B,i}$, respectively. Equation (3.14) assumes that cv belongs to the grid block containing $\mathcal{M}_A$. If cv is on the grid block containing $\mathcal{M}_B$, the indices A and B must be interchanged. Considering the two-dimensional case depicted in Fig. 3.6(c), Eq. (3.14) reduces to

$$\phi_{fa} = \frac{a\,(\phi_4 d_{0,1} + \phi_0 d_4)}{(d_{0,1} + d_4)} + \frac{(1-a)\,(\phi_5 d_{0,2} + \phi_0 d_5)}{(d_{0,2} + d_5)}. \tag{3.15}$$

3.4.2 Green–Gauss gradient

The GG method numerically approximates the Green–Gauss theorem as

$$\nabla\phi_{cv} = \frac{1}{V_{cv}} \sum_{fa=1}^{N_{fa}} \phi_{fa} A_{fa} \mathbf{n}_{fa}, \tag{3.16}$$

with $\mathbf{n}_{fa}$ indicating the unit vector normal to the face. In second order cell-centered numerical schemes ϕ_{fa} is commonly linearly interpolated as

$$\phi_{fa} = \frac{\phi_{cv} d_{nb} + \phi_{nb} d_{cv}}{d_{nb} + d_{cv}}, \tag{3.17}$$

where $d_{cv} = |\mathbf{x}_{cv} - \mathbf{x}_{fa}|$ and $d_{nb} = |\mathbf{x}_{nb} - \mathbf{x}_{fa}|$. The GG gradient only requires the face value on the interface boundary for the non-conformal interface problem (GGI). This is done by using Eq. (3.14). No additional modification to the standard scheme is required.

3.4.3 Analytical order of accuracy

The analytical derivation of the order of accuracy for the schemes introduced above is given in this section. The procedure is based on the Taylor series expansion of the solution in the neighboring cells, which is substituted into the schemes described above. The order of accuracy is quantified by the order of magnitude of the truncation error.

In case of internal control volumes (no interface), LS and GG are equivalent on a structured grid

$$\begin{pmatrix} \partial_x^{LS}\phi_0 \\ \\ \partial_y^{LS}\phi_0 \end{pmatrix} \equiv \begin{pmatrix} \partial_x^{GG}\phi_0 \\ \\ \partial_y^{GG}\phi_0 \end{pmatrix} = \begin{pmatrix} \frac{\phi_4-\phi_0}{2\Delta x_4} + \frac{\phi_2-\phi_0}{2\Delta x_2} \\ \\ \frac{\phi_3-\phi_0}{2\Delta y_3} + \frac{\phi_1-\phi_0}{2\Delta y_1} \end{pmatrix}, \tag{3.18}$$

with $\Delta x_{nb} = x_{nb} - x_0$ and $\Delta y_{nb} = y_{nb} - y_0$. In Eq. (3.18) and in the following it is assumed that the unit normal vectors to the faces of $cv = 0$ point outwards from the control volume. The length of the faces A_h and A_v is calculated as $A_h = x_{fa,4} - x_{fa,2}$ and $A_v = y_{fa,3} - y_{fa,1}$, where fa, nb is the face shared by $cv = 0$ and the neighbor nb. It follows that $x_0 = (x_{fa,2} + x_{fa,4})/2$ and $y_0 = (y_{fa,1} + y_{fa,3})/2$.

The function in the neighbors cell centers is approximated by the Taylor series expansion as

$$\phi_{nb} = \phi_0 + \partial_x\phi_0\Delta x_{nb} + \partial_y\phi_0\Delta y_{nb} + \partial^2_{xx}\phi_0\frac{\Delta x^2_{nb}}{2} + \partial^2_{yy}\phi_0\frac{\Delta y^2_{nb}}{2} + \partial^2_{xy}\phi_0\Delta x_{nb}\Delta y_{nb} + O(\Delta x^3) + O(\Delta y^3). \tag{3.19}$$

Substituting the Taylor expansions into Eq. (3.18) leads to

$$\begin{pmatrix} \partial^{LS}_x\phi_0 \\ \\ \partial^{LS}_y\phi_0 \end{pmatrix} \equiv \begin{pmatrix} \partial^{GG}_x\phi_0 \\ \\ \partial^{GG}_y\phi_0 \end{pmatrix} = \begin{pmatrix} \partial_x\phi_0 + \partial^2_{xx}\phi_0\frac{\Delta x_4+\Delta x_2}{4} + O(\Delta x^2) \\ \\ \partial_y\phi_0 + \partial^2_{yy}\phi_0\frac{\Delta y_3+\Delta y_1}{4} + O(\Delta y^2) \end{pmatrix}, \tag{3.20}$$

which shows that the methods are in general first order accurate on non-uniform grids and second order accurate in case either $\partial^2_{xx}\phi_0 = \partial^2_{yy}\phi_0 = 0$ or the grid is uniform ($|\Delta x_2| = |\Delta x_4|$ and $|\Delta y_1| = |\Delta y_3|$).

3.4.3.1 LSI-C

The order of accuracy for LSI-C is derived next. Note, the order of accuracy for LSI-F is the same as for LSI-C and is not shown here for the sake of brevity. Let us consider the stencil depicted in Fig. 3.6(b). The weights for the least squares gradient are

$$w_1^2 = \frac{1}{\Delta y_1^2}, \quad w_2^2 = \frac{1}{\Delta x_2^2}, \quad w_3^2 = \frac{1}{\Delta y_3^2}, \quad w_4^2 = \frac{1}{\Delta x_4^4 + \Delta y_4^2}, \tag{3.21}$$

Equation (3.10) reduces to

$$\begin{pmatrix} \partial^{LSI-C}_x\phi_0 \\ \\ \partial^{LSI-C}_y\phi_0 \end{pmatrix} = (\Delta x_4^2 + \Delta y_4^2)\begin{pmatrix} 2\Delta x_4^2 + \Delta y_4^2 & \Delta x_4\Delta y_4 \\ \\ \Delta x_4\Delta y_4 & 2\Delta x_4^2 + 3\Delta y_4^2 \end{pmatrix}^{-1}\begin{pmatrix} \frac{\phi_2-\phi_0}{\Delta x_2} + \frac{(\phi_4-\phi_0)\Delta x_4}{\Delta x_4^2+\Delta y_4^2} \\ \\ \frac{\phi_1-\phi_0}{\Delta y_1} + \frac{\phi_3-\phi_0}{\Delta y_3} + \frac{(\phi_4-\phi_0)\Delta y_4}{\Delta x_4^2+\Delta y_4^2} \end{pmatrix}. \tag{3.22}$$

The least squares approximation of the gradient can be thus written as

$$\begin{pmatrix} \partial^{LSI-C}_x\phi_0 \\ \\ \partial^{LSI-C}_y\phi_0 \end{pmatrix} = \frac{1}{4\Delta x_4^2 + 3\Delta y_4^2}\begin{pmatrix} \left(2\Delta x_4^2 + 3\Delta y_4^2\right)\frac{\phi_2-\phi_0}{\Delta x_2} - \Delta x_4\Delta y_4\left(\frac{\phi_1-\phi_0}{\Delta y_1} + \frac{\phi_3-\phi_0}{\Delta y_3}\right) + 2\Delta x_4\left(\phi_4 - \phi_0\right) \\ \\ \left(2\Delta x_4^2 + \Delta y_4^2\right)\left(\frac{\phi_1-\phi_0}{\Delta y_1} + \frac{\phi_3-\phi_0}{\Delta y_3}\right) - \Delta x_4\Delta y_4\frac{\phi_2-\phi_0}{\Delta x_2} + \Delta y_4\left(\phi_4 - \phi_0\right) \end{pmatrix}. \tag{3.23}$$

The order of accuracy of Eq. (3.23) is calculated by replacing ϕ_1, ϕ_2, ϕ_3, and ϕ_4 with their Taylor expansions

$$\begin{pmatrix} \partial_x^{LSI-C}\phi_0 \\ \\ \partial_y^{LSI-C}\phi_0 \end{pmatrix} = \begin{pmatrix} \partial_x\phi_0 + \frac{\partial^2_{xx}\phi_0}{2}\frac{\Delta x_2\left(2\Delta x_4^2+3\Delta y_4^2\right)+2\Delta x_4^3}{4\Delta x_4^2+3\Delta y_4^2} + \frac{\partial^2_{yy}\phi_0}{2}\frac{2\Delta x_4\Delta y_4^2-\Delta x_4\Delta y_4(\Delta y_1+\Delta y_3)}{4\Delta x_4^2+3\Delta y_4^2} \\ \\ \partial_y\phi_0 + \frac{\partial^2_{xx}\phi_0}{2}\frac{\Delta y_4\Delta x_4^2-\Delta x_2\Delta x_4\Delta y_4}{4\Delta x_4^2+3\Delta y_4^2} + \frac{\partial^2_{yy}\phi_0}{2}\frac{\left(2\Delta x_4^2+\Delta y_4^2\right)(\Delta y_1+\Delta y_3)+\Delta y_4^3}{4\Delta x_4^2+3\Delta y_4^2} \end{pmatrix}$$
$$+\partial^2_{xy}\phi_0\frac{\Delta x_4^2\Delta y_4}{4\Delta x_4^2+3\Delta y_4^2} + O(\Delta x^2) + O\left(\frac{\Delta y^3\Delta x}{\Delta x^2+\Delta y^2}\right) + O\left(\frac{\Delta x^4}{\Delta x^2+\Delta y^2}\right)$$
$$+\partial^2_{xy}\phi_0\frac{\Delta y_4^2\Delta x_4}{4\Delta x_4^2+3\Delta y_4^2} + O(\Delta y^2) + O\left(\frac{\Delta x^3\Delta y}{\Delta x^2+\Delta y^2}\right) + O\left(\frac{\Delta y^4}{\Delta x^2+\Delta y^2}\right) \Bigg). \quad (3.24)$$

Equation (3.24) shows that LSI-C is in general first order accurate even if the two non-conformal mesh blocks are regular structured grids of squared elements.

3.4.3.2 LSI-Fa and GGI

In case the face which is located on the interface is treated as an external boundary face, see Fig. 3.6(c), LS-Fa and GGI reduce to the same expression

$$\begin{pmatrix} \partial_x^{LSI-Fa}\phi_0 \\ \\ \partial_y^{LSI-Fa}\phi_0 \end{pmatrix} \equiv \begin{pmatrix} \partial_x^{GGI}\phi_0 \\ \\ \partial_y^{GGI}\phi_0 \end{pmatrix} = \begin{pmatrix} \frac{\phi_{fa}-\phi_0}{\Delta x_{fa}} + \frac{\phi_2-\phi_0}{2\Delta x_2} \\ \\ \frac{\phi_3-\phi_0}{2\Delta y_3} + \frac{\phi_1-\phi_0}{2\Delta y_1} \end{pmatrix}. \quad (3.25)$$

The approximation of the gradient along the direction parallel to the interface is not affected by the interface treatment, i.e. $\partial_y^{LSI-Fa}\phi_0 \equiv \partial_y^{GGI}\phi_0 \equiv \partial_y^{GG}\phi_0 \equiv \partial_y^{LS}\phi_0$. Replacing ϕ_{fa} with Eq. (3.15)

$$\partial_x^{GGI}\phi_0 = \frac{1}{2\Delta x_{fa}}\left[a\frac{\phi_4 d_{0,1}+\phi_0 d_{4,1}}{d_{0,1}+d_{4,1}} + (1-a)\frac{\phi_5 d_{0,2}+\phi_0 d_{5,2}}{d_{0,2}+d_{5,2}} - \phi_0\right] + \frac{\phi_2-\phi_0}{2\Delta x_2}. \quad (3.26)$$

Expanding ϕ_2, ϕ_4, and ϕ_5 in Taylor series we obtain

$$\begin{aligned}
\partial_x^{GGI}\phi_0 = \partial_x\phi_0 &- \frac{\partial_x\phi_0}{2}\frac{1}{\Delta x_{fa}}\left[\Delta x_{fa} - \frac{a d_{0,1}\Delta x_4}{d_{0,1}+d_{4,1}} + \frac{(1-a)d_{0,2}\Delta x_5}{d_{0,2}+d_{5,2}}\right] \\
&+ \frac{\partial_y\phi_0}{2}\frac{1}{\Delta x_{fa}}\left[\frac{a d_{0,1}\Delta y_4}{d_{0,1}+d_{4,1}} + \frac{(1-a)d_{0,2}\Delta y_5}{d_{0,2}+d_{5,2}}\right] \\
&+ \frac{\partial^2_{xx}\phi_0}{4}\frac{1}{\Delta x_{fa}}\left[\frac{a\Delta x_4^2 d_{0,1}}{d_{0,1}+d_{4,1}} + \frac{(1-a)\Delta x_5^2 d_{0,2}}{d_{0,2}+d_{5,2}} + \Delta x_2\Delta x_{fa}\right] \\
&+ \frac{\partial^2_{yy}\phi_0}{4}\frac{1}{\Delta x_{fa}}\left[\frac{a\Delta y_4^2 d_{0,1}}{d_{0,1}+d_{4,1}} + \frac{(1-a)\Delta y_5^2 d_{0,2}}{d_{0,2}+d_{5,2}}\right] \\
&+ \frac{\partial^2_{xy}\phi_0}{2}\frac{1}{\Delta x_{fa}}\left[\frac{a d_{0,1}\Delta x_4\Delta y_4}{d_{0,1}+d_{4,1}} + \frac{(1-a)d_{0,2}\Delta x_5\Delta y_5}{d_{0,2}+d_{5,2}}\right] + \ldots \quad (3.27)
\end{aligned}$$

which can be recasted as

$$\partial_x^{GGI}\phi_0 = \partial_x\phi_0 + \partial_x\phi_0 O\left(\Delta x^0\right) + \partial_y\phi_0 O\left(\frac{\Delta y}{\Delta x}\right) + \ldots, \tag{3.28}$$

showing the presence of two terms of order-0 which prevent the approximated gradient to converge as the computational grid is refined.

3.4.4 Numerical convergence

The accuracy of the gradient reconstruction is verified numerically in two and three dimensions for the following test functions

$$f_1^{2D} = x\,y, \tag{3.29}$$

$$f_2^{2D} = \sin(2\pi\bar{x})\sin(2\pi\bar{y}), \tag{3.30}$$

$$f_3^{3D} = \sin(4\pi x) + \sin(4\pi y) + \sin(4\pi z), \tag{3.31}$$

$$f_4^{3D} = \sin(2\pi\tilde{x})\ \sin(2\pi y)\ \sin(2\pi\tilde{z}). \tag{3.32}$$

where the bar $(\bar{.})$ and tilde $(\tilde{.})$ indicate a transformed coordinate system, which is rotated by $\pi/4$ about the z and y axis, respectively. The test domains are $\Omega_{2D} = [0,1]\times[0,1] \subset \Re^2$ and $\Omega_{3D} = [0,1]\times[0,1]\times[0,1] \subset \Re^3$. The interface is placed at $x = 0.5$ in the 2D case and at $z = 0.5$ in the 3D case. The computational domain is made of a coarse structured grid on the left side of the interface and of a finer grid on the right side of the interface. The elements of both grid blocks are regular quadrilaterals in 2D and cubes in 3D. The edge ratio of the fine grid elements to the coarse grid is 0.7, and it is kept constant during the mesh refinements. To assess the calculated order of accuracy of the LS, GG, LSI-C, LSI-F, LSI-Fa and GGI methods, the L_1 norm of the difference between the reconstructed and analytical value of the gradient is used, namely

$$\|\varepsilon_j\|_{L_1} = \left(\sum_{i=1}^{N} |\partial_j^{NUM}\phi_i - \partial_j\phi_i| \,/\, |\partial_j\phi_i|\right) / N, \tag{3.33}$$

where N indicates the total number of control volumes used to calculate the error, and $j = x, y, z$ is the component of the gradient. No slope limiter is used. Results for the particular case of matching mesh blocks are not included since equations (3.24) and (3.27) reduce to Eq. (3.20) in this specific situation, therefore recovering the same convergence property as for the internal cells.

Figure 3.7 displays the convergence of the error for the test functions in the 2D domain. The calculated convergence rates for LSI-F, LSI-C, LSI-Fa, and GGI are consistent with the analytical derivation of the order of accuracy of Sec. 3.4.3. LSI-F and LSI-C both converge first order, and LSI-Fa and GGI show an error of order zero along the direction which crosses the interface, while the convergence along the direction parallel to the interface is not affected and is the same as for the internal cells, see Eq. (3.25). In Fig. 3.7(a) (f_1^{2D}), the results for the LS and GG methods in the internal cells are not shown since both

methods exactly reconstruct a function that has zero second and higher order derivatives on a regular grid. The same property holds for the y derivative in case of GGI and LSI-Fa.

The calculated order of accuracy in 3D is shown in Fig. 3.8. The rate of convergence agrees with the derivation of Sec. 3.4.3 obtained in 2D case. In case of f_3^{3D}, LSI-C shows an order of accuracy close to two, while LSI-F remains first order as predicted by the analytical expression. For f_4^{3D}, the calculated converge of the y derivative of both LSI-F and LSI-C is below first order.

Overall, the results do not lead to conclusive evidence about which of the methods is best. LSI-C appears to offer a better reconstruction of the gradient as compared to LSI-F, and shows second order convergence in case of f_3^{3D} while LSI-F remains first order for all the test functions considered. GGI and LS-Fa are a trade-off between accuracy and simplicity of implementation. On the one hand a constant error in the direction perpendicular to the interface is introduced, which is quantified to about 10% at most for all the numerical tests performed. On the other hand, second order accuracy is maintained along the directions parallel to the interface.

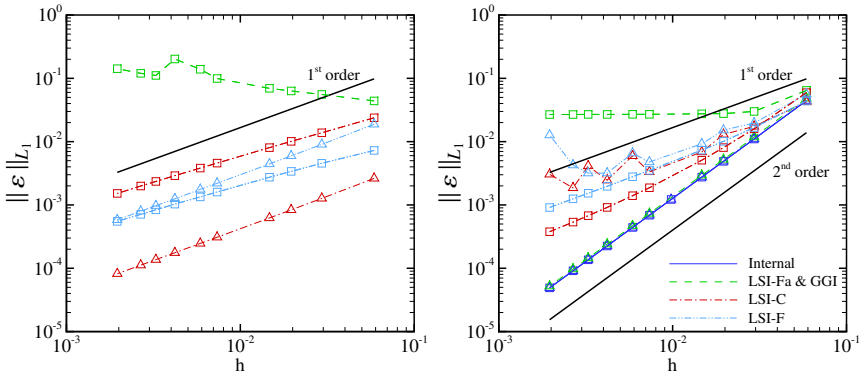

(a) $f_1^{2D} = x\,y$ (b) $f_2^{2D} = \sin(2\pi\bar{x})\sin(2\pi\bar{y})$

Figure 3.7: Average L_1 norm of the error on the gradient reconstruction in the internal and interface control volumes on a two dimensional domain. Symbols indicate the components of the derivatives, namely □ is $\partial_x\phi$ and △ is $\partial_y\phi$.

3.5 Parallelization

The parallel distribution of the supermesh generation procedure and of the interface flux calculation are discussed here. The former is independent from the topology of the mesh after the partitioning step. A possible strategy to compute the supermesh in parallel is detailed in Sec. 3.5.1. The interface flux calculation requires an adaptation in case the interface is splitted among several cores. The choice of whether to distribute the interface control volumes among different cores or not depends on several factors that are summa-

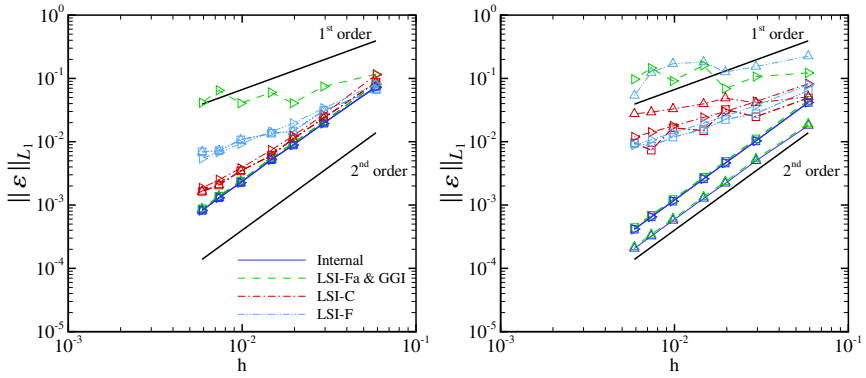

(a) $f_3^{3D} = \sin(4\pi x) + \sin(4\pi y) + \sin(4\pi z)$ (b) $f_4^{3D} = \sin(2\pi\tilde{x})\,\sin(2\pi y)\,\sin(2\pi\tilde{z})$

Figure 3.8: Average L_1 norm of the error on the gradient reconstruction in the internal and interface control volumes on a three dimensional domain. Symbols indicate the components of the derivatives, namely □ is $\partial_x\phi$, △ is $\partial_y\phi$, and ▷ is $\partial_z\phi$.

rized in Tab. 5.2. Load balancing benefits from a sub-division of the interface. However, having the interface distributed on several cores, requires additional data exchange between them in order to update the interface supermesh properties. Moreover, memory usage is penalized by the need to store these additional variables. Given the usually small ratio of interface-to-internal faces, the requirements in terms of additional memory usage and data exchange between the cores are not large enough to justify the loss in load balance. Therefore, only the case where the interface is split among multiple cores is treated here.

3.5.1 Distributed supermesh construction

The schematic graphical representation of an exemplary parallel supermesh construction is given in Fig. 3.9. It shows a 2D grid partitioning on three cores that also splits the non-conformal interface. First, the interface control volumes are pre-processed in order to define the complete parent meshes $\mathcal{M}_A$ and $\mathcal{M}_B$, see Fig. 3.9(b), and this information is shared among all the cores. Subsequently, each core checks only a limited number of

Table 3.1: Advantages and disadvantages of partitioning the non-conformal interface.

	Single core	Multiple cores
Load balance	−	+
Memory	+	−
Data exchange	+	−
Supermesh generation	+	+

$\mathcal{E}_A$ for intersections with $\mathcal{E}_B$ in order to define a temporary local supermesh $\overline{\mathcal{M}}_{S,i}$, see Fig. 3.9(c), with $i = 1, 2, 3$ in this case. All the $\overline{\mathcal{M}}_{S,i}$ are then grouped together to define the complete supermesh $\mathcal{M}_S$. The last step consists in distributing to each core only the $\mathcal{E}_S$ mapped on the local $\mathcal{M}_A$ and $\mathcal{M}_B$, see Fig. 3.9(d) and 3.9(e). As a consequence, every core has a new local supermesh $\mathcal{M}_{S,i} \subseteq \mathcal{M}_S$. If no parent mesh elements are present locally, $\mathcal{M}_{S,i} = \emptyset$, as it is the case for CORE 3 in Fig. 3.9(a). As expected, the scaling of the proposed parallelization is linear, see Fig. 3.10.

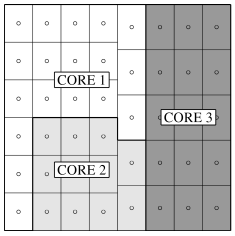

(a) Grid partition.

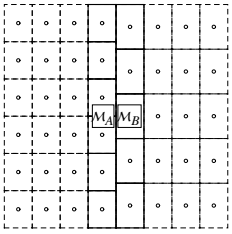

(b) Parent meshes identification.

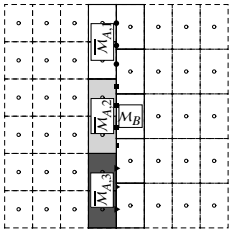

(c) Parallel supermesh generation.

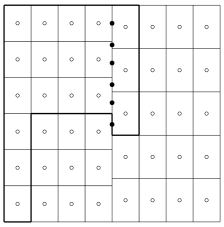

(d) Local supermesh: CORE 1.

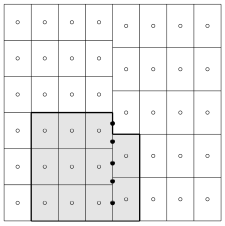

(e) Local supermesh: CORE 2.

Figure 3.9: Schematic representation of the procedural steps involved in the generation of a supermesh. Filled symbols indicate the cell centers of the supermesh elements.

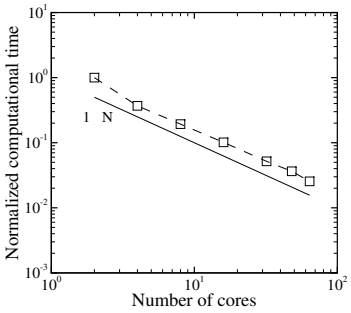

Figure 3.10: Calculated scaling of the parallel supermesh construction (dashed line). Results are obtained for two fixed $\mathcal{M}_{A,B}$ counting 5×10^4 elements each.

3.5.2 Flux assembly across the interface

If information about the control volumes, identified by $\mathcal{T}_{A,i}$ and $\mathcal{T}_{B,i}$, is stored locally on the core, no additional information is needed in order to calculate the supermesh face flux and sum it to the corresponding control volume flux balances. Every variable can be retrieved by using the control volume index only. Conversely, if either $\mathcal{T}_{A,i}$ or $\mathcal{T}_{B,i}$ is not stored locally for that core, communication is required to retrieve the necessary flow variables. Thus, we propose to store on each supermesh face the flow properties and to update them at each time step. This comes at a computational cost that depends on the number of the needed flow variables, on the number of supermesh elements, and on the number of cores used for the partition. Memory usage also increases with the number of variables and supermesh elements. However, given the relatively small interface to internal mesh face ratio, the penalty in terms of memory and computational efficiency is not expected to significantly influence the code performance.

3.6 Numerical verification for the Navier–Stokes equations

The Navier–Stokes equations are used for the verification of the proposed mesh blocks interface treatment. Five exemplary test cases provide the numerical verification. Stationary non-conformal grid blocks are considered in Sec. 3.6.2, 3.6.3 and 3.6.4, while mesh blocks in relative motion are considered in Sec. 3.6.5 and 3.6.6. A wide range of flow regimes is investigated, i.e., subsonic, transonic and supersonic flows, under steady state and unsteady conditions, including flow discontinuities (shock waves) crossing the mesh interface.

For the stationary test cases, the validation is performed by comparing the flow field calculated on a two-block mesh to the one obtained on a single-block mesh, i.e., no interface, with comparable elements size. The numerical flux conservation is verified for the continuity and energy equations as the difference between the integrated values at the interface and the ones calculated at the outlet and inlet boundaries. Relative differences were found to be of the order of machine precision and are not included here. Convergence histories are also shown and the numerical stability is demonstrated empirically for explicit and implicit time integration schemes.

3.6.1 Navier–Stokes solver

The conservative variables vector for the Navier–Stokes equations is

$$\mathbf{U} = \begin{pmatrix} \rho \\ \rho\mathbf{v} \\ \rho e^t \end{pmatrix}, \tag{3.34}$$

whereby ρ is the fluid density, $\mathbf{v}$ is the velocity vector, and $e^t = e + \frac{1}{2}|\mathbf{v}|^2$ is the specific total energy. The fluxes are conveniently splitted into a convective and diffusive part, namely $\mathbf{F} = \mathbf{F}_c + \mathbf{F}_d$ and

$$\mathbf{F}_c = \begin{pmatrix} \mathbf{n}\cdot\rho\mathbf{v} \\ \rho\mathbf{v}\,(\mathbf{n}\cdot\mathbf{v}) + P\mathbf{n} \\ (\rho e^t + P)\,(\mathbf{v}\cdot\mathbf{n}) \end{pmatrix} \quad \text{and} \quad \mathbf{F}_d = \begin{pmatrix} 0 \\ \mathbf{n}\cdot\Pi \\ \mathbf{v}\cdot(\mathbf{n}\cdot\Pi) + \mathbf{n}\cdot(\lambda\nabla T) \end{pmatrix}, \tag{3.35}$$

in which P denotes the pressure, T the temperature and λ the thermal conductivity. The stress tensor is expressed as $\Pi = \mu\left(\nabla\otimes\mathbf{v} + (\nabla\otimes\mathbf{v})^{\mathrm{T}} - \frac{2}{3}(\nabla\cdot\mathbf{v})\,\mathbb{I}\right)$, with μ being the dynamic viscosity of the fluid, T indicating the transpose operator, $\mathbb{I}$ the identity matrix, and $\otimes$ the outer (or tensor) product.

The convective fluxes are evaluated numerically at each face of the domain using an approximate Riemann solver, e.g., AUSM$^+$ [27] or HLLC [28]. The evaluation of the diffusive fluxes needs an accurate evaluation of the temperature and velocity gradients on the faces, which are calculated as

$$\nabla\phi_{fa}\cdot\mathbf{n}_{fa} = \frac{\phi_{nb}-\phi_{cv}}{|\mathbf{x}_{nb}-\mathbf{x}_{cv}|}\alpha_{fa} + \frac{1}{2}\left(\nabla\phi_{nb} + \nabla\phi_{cv}\right)\cdot\left(\mathbf{n}_{fa} - \alpha_{fa}\mathbf{s}_{fa}\right), \tag{3.36}$$

with $\alpha_{fa} = \mathbf{s}_{fa} \cdot \mathbf{n}_{fa}$, and $\mathbf{s}$ the normalized vector connecting the *nb* and *cv* cell centroids. Second order spatial accuracy is achieved using the GG method for the internal control volumes and GGI at the interface. The gradient slope limiter proposed by Venkatakrishnan [29] is adopted. More details on the flow solver used in this study are given by Pecnik *et al.* [30].

Time integration can performed using explicit three-steps Runge–Kutta (RK3) scheme [31], which is second order accurate, or implicit schemes, namely backward Euler and backward-differentiation-formula (BDF2), in order to avoid restrictions related to the choice of the time step. In case implicit schemes are used, the numerical scheme requires the definition of the flux Jacobians. A thorough derivation of the Jacobians employed in the CFD code is given by Rinaldi *et al.* [32].

3.6.2 Cylinder in supersonic cross flow

An incoming inviscid supersonic flow at Mach number $M = 4$ is considered. First order accuracy was used for the convective flux discretization and the Euler equations were integrated in time with the explicit RK3 method and the implicit backward Euler scheme. For the latter, the Courant number was gradually increased after 100 time steps from $CFL = 1$ to $CFL = 1000$.

Fig. 3.11 shows the calculated Mach number contour lines on a single-block and two-block domain. The shock waves cross the interface without generating any spurious oscillation and no discrepancies are observed between the two solutions. The only differences in the Mach distribution downstream of the cylinder are due to a coarser spacing of the elements of the right-hand side mesh block for the two-block grid. The convergence history is not affected by the presence of the interface for both, explicit and implicit simulations, see Fig. 3.12.

3.6.3 Laminar vortex shedding

A second test case is provided by the simulation of the laminar vortex shedding from a two-dimensional cylinder at Reynolds number $Re = 1300$ (based on the inlet properties and the cylinder diameter). Second order spatial and temporal accuracy is used. The Navier-Stokes equations are integrated with the explicit RK3 scheme using a constant $\Delta t = 2.5 \times 10^{-6}$ s.

The calculated flow fields for the single-block and two-block meshes are superimposed in Fig. 3.13 in terms of density, vorticity and pressure, at the same normalized time. A coarser mesh is used for the right block of the two-block computational domain, which introduces more diffusion in the vortices downstream of the cylinder and is the reason for slight differences in the contour lines. The coarse mesh block also influences the solution on the fine mesh block (left-hand side) since the information can propagate upstream in a subsonic flow.

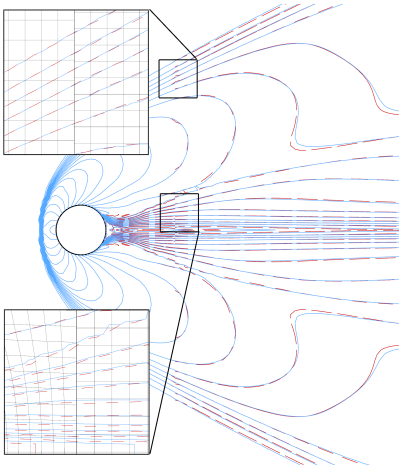

Figure 3.11: Mach number contour lines obtained from the simulation results of a cylinder in a $M = 4$ supersonic cross flow. The solution obtained on a single-block mesh (solid line) is compared to the one obtained on a two-block mesh (dashed lines). Detailed views of the wake and bow shock at the interface are given in the square boxes.

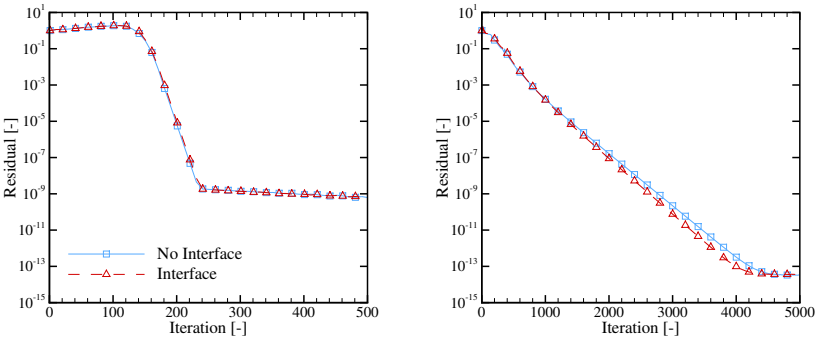

Figure 3.12: Convergence history of the energy equation related to the simulation whose results are displayed in Fig. 3.11. The Euler equations were integrated using the implicit backward Euler (top) and explicit three-steps Runge–Kutta (bottom) methods.

3.6.4 Inviscid supersonic flow in a three-dimensional double bump channel

The simulation of an inviscid, $M = 2.5$ supersonic flow in a double bump channel is used to test the interface treatment in case the flow is three-dimensional. The two bumps are located on the bottom and side wall. This configuration guarantees that the flow is fully

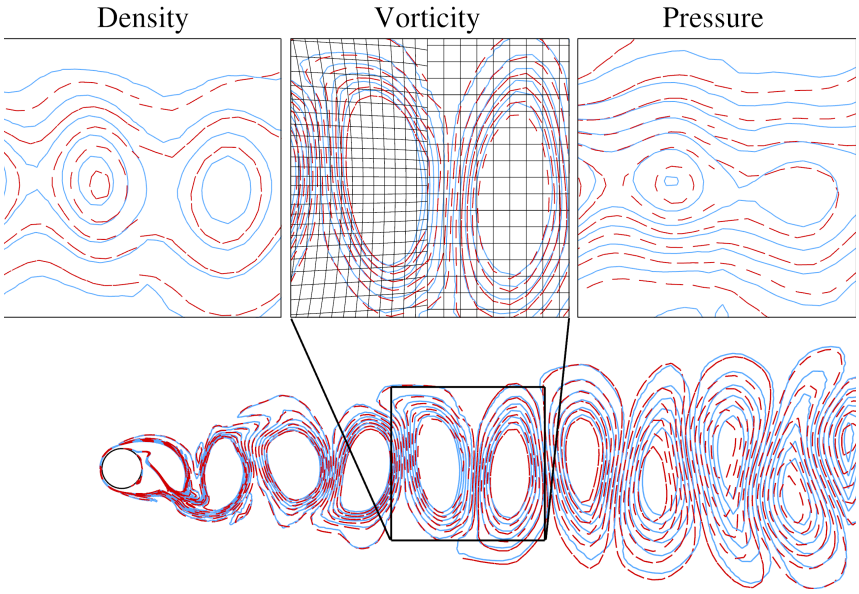

Figure 3.13: Results of the simulation of the laminar vortex shedding at $Re = 1300$. The solution obtained by means of a single-block mesh (solid line) is compared to the one obtained with a two-block mesh (dashed lines). Note that in case of a two-block mesh, the blocks are considered as disconnected by the visualization tool. Thus, the contour lines might display a discontinuity at the interface, which is not physical but merely an artifact of the visualization.

three-dimensional due to the interaction between shock waves and expansion fans. A structured mesh is used for the single-block domain. The interface for the two-block mesh is located downstream of the bumps. The mesh upstream of the interface is the same as for the single block configuration, while downstream of the interface the mesh consists of wedge elements. In both cases the computational domain counted approximately 650,000 control volumes. Second order spatial accuracy was used, and the Euler equations were integrated using the implicit backward Euler scheme with an initial $CFL = 50$, which was gradually increased after 10 time steps up to $CFL = 1000$.

The calculated flow fields are displayed in Fig. 3.14 on two planes, at half of the channel width and height. The small but appreciable differences seen in the Mach number contour lines downstream of the interface are due to the different volume distribution of mesh elements between the single-block and two-block cases. The convergence history of the energy equation is reported in Fig. 3.15 and shows a slower convergence rate for the two-block case after the residual has decreased by six orders of magnitude.

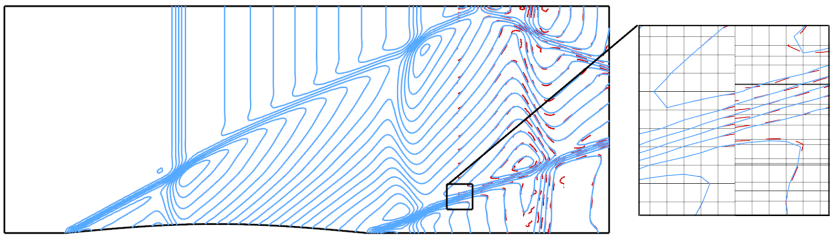

(a) Half channel height plane.

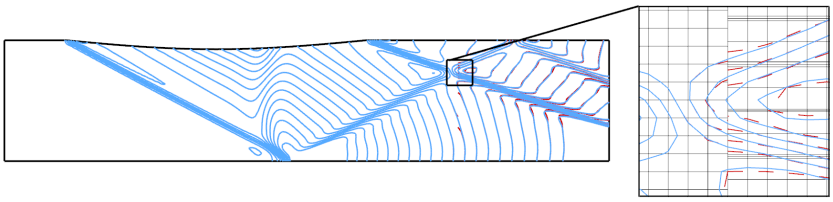

(b) Half channel width plane.

Figure 3.14: Mach number contour lines for the simulation results of an inviscid $M = 2.5$ supersonic flow in a three-dimensional double bump channel. The solution obtained by means of a single-block mesh (solid line) is compared to the one obtained with a two-block mesh (dashed lines).

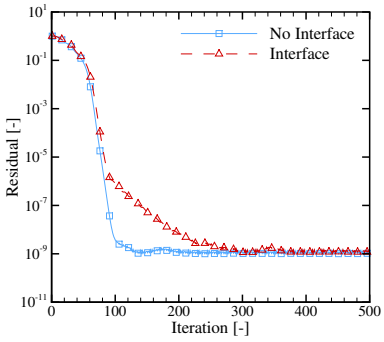

Figure 3.15: Convergence history of the energy equation related to the simulation whose results are displayed in Fig. 3.14. Equations were integrated using the backward Euler scheme.

3.6.5 Cylinders in relative motion in inviscid supersonic cross flow

This and the following section describe the results of two test cases in which the interface treatment is applied to mesh blocks in relative motion. For these cases the supermesh construction as described in Sec. 3.2 has to be repeated at every time step after the relative position of the two mesh blocks is updated.

The right patch of the computational domain moves vertically at a constant speed v_R such that $v_R/c_{in} = 0.2$, where c_{in} is the speed of sound at the inlet. The test case is the simulation of a uniform normalized ideal gas flow entering from the inlet boundary at $M = 4$ and crossing two cylinders. Periodic boundary conditions are set on the upper and lower boundaries. Second order spatial accuracy is used and Euler equations are integrated using the implicit two-steps backward-differentiation-formula (BDF2) method with a constant time step defined such that one translating period is discretized in 28,000 steps.

Fig. 3.16 displays the evolution of the Mach distribution over one period. Downstream of the first cylinder the flow is still supersonic. This results in a second bow shock in front of the moving cylinder, which interacts with the first one. The shock crosses the interface smoothly, as seen by the contour lines and the same conclusion of Sec. 3.6.2 also apply here. The convergence history shows that a periodic flow state is achieved after two complete cylinder passes, and that the present interface treatment does not have any negative effect on the periodicity, see Fig. 3.17. The peak of the residual at $t = 0$ corresponds to the downstream cylinder being in the wake of the upstream cylinder. The two peaks at $t = 0.25T$ and $t = 0.75T$, where T indicates the period, correspond to the impingement of the first bow shock tails on the front part of the second bow shock, as can be observed in Fig. 3.16.

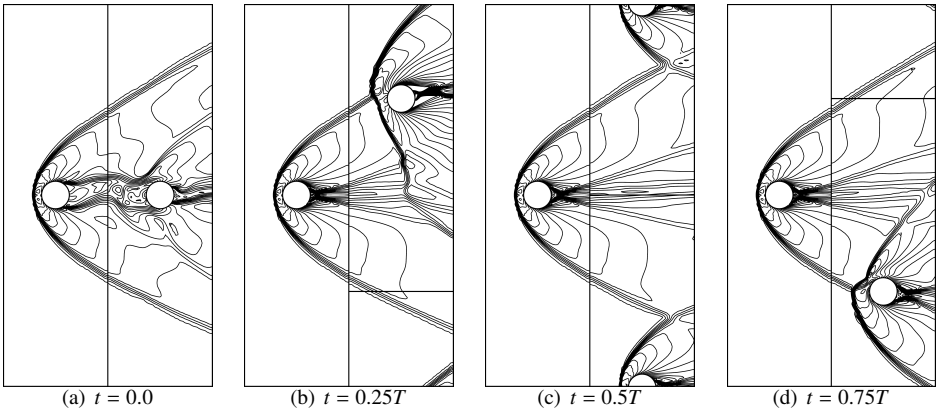

(a) $t = 0.0$ (b) $t = 0.25T$ (c) $t = 0.5T$ (d) $t = 0.75T$

Figure 3.16: Mach number contour lines for the simulation results of two cylinders in relative motion in a $M = 4$ supersonic cross flow. The external edge of the mesh blocks is shown in order to locate the interface and the periodic boundaries for the moving patch.

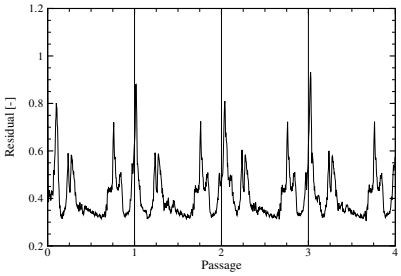

Figure 3.17: Convergence history of the energy equation related to the simulation whose results are displayed in Fig. 3.16. Equations were integrated using the BDF2 method and a constant time step chosen such that one period corresponds to 28,000 steps.

3.6.6 Transonic axial turbine stage

The final test case chosen for the verification of the interface treatment is the simulation of the transonic flow through the blades of an axial turbine stage. The considered geometry was designed by Erhard and Gehrer[33] and numerically investigated by Schennach *et al.*[34]. The purpose of this test case is to show the effectiveness of the interface treatment on a problem of engineering interest, such as an unsteady turbomachinery simulation, which features the complexity of combined vortex shedding crossing the interface and shock waves propagating upstream and downstream of the interface. Due to the periodicity of the geometry, a reduced computational domain was used to perform the CFD simulation. It includes two stator vanes and three rotor blades, counting approximately 50,000 cells in total. A two-dimensional turbulent simulation of the mid-span plane was performed using the Spalart and Allmaras (SA) turbulence model[35], whereby a non-uniform distribution of the cross-section area was included. Second order spatial accuracy was used. Total pressure $P_{tot} = 3.429$ bar and total temperature $T_{tot} = 454.4$ K were set at the inlet, while a constant static pressure $P = 1.102$ bar was imposed at the outlet. The rotor blades move at a vertical velocity of $v_R = 268.166$ m/s. The Navier–Stokes equations and the transport equation for the SA turbulence model were integrated with the BDF2 method using 40,000 time steps to discretize one period.

Contours for the magnitude of the vorticity and lines for the magnitude of the pressure gradient are shown in Fig. 3.18, which displays the evolution of the flow field over a complete period. The fluid enters the domain from the left-hand-side boundary and is accelerated in the stator to a supersonic state, which leads to the formation of a normal shock wave near the trailing edge of the stator vanes. The shock propagates to the rotor and impinges on the leading edge of the rotor blades. A second shock is then reflected back to the stator interacting with the vortex shedding from the vanes trailing edge, and eventually impinges on the vane suction side. Supersonic conditions are met also further downstream in the rotor channel, as demonstrated by the presence of a trailing edge shock wave on the rotor blades.

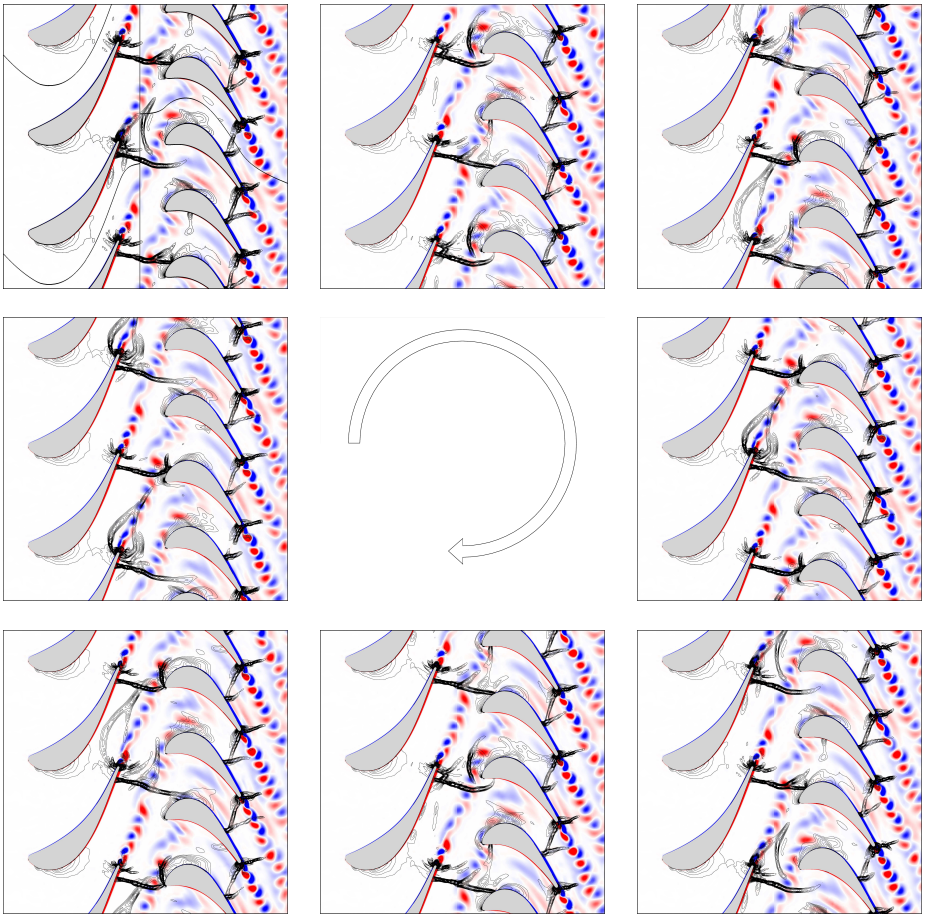

Figure 3.18: Results of the simulation of the flow in the transonic turbine stage described in Refs.[33,34]. Colors represent the vorticity field (blue indicates negative values, red positive values, the range is from -35,000 1/s to 35,000 1/s). Lines indicate the pressure gradient (100 lines are used on the range 5 MPa/m to 1,100 MPa/m). The images cover a complete time period starting from $t = 0$ in the top-left sub-figure, whereby the computational domain is shown (black line).

3.7 Conclusions

This paper presents a new flux-conserving treatment of the interface between non-conformal mesh blocks. The method is based on the definition of an auxiliary interface mesh, called supermesh, which establishes a connection between the interface control volumes and is defined by the intersection of the elements of the non-conformal interface grid blocks. The method can be applied to the finite-volume discretization of any system of conservation laws, however the present study is applied to the Euler and Navier–Stokes equations only.

Numerical flux conservation is ensured by calculating the fluxes on the supermesh elements and summing their contribution to the respective control volumes of the parent meshes, thus avoiding any flux interpolation. Details of the procedure to generate the supermesh are discussed in 2D and 3D cases. The accuracy of the intersection scheme used to define the supermesh elements is of crucial importance to satisfy the definition of the supermesh and to ensure the flux conservation property of the method. The parallelization of the supermesh generation and interface treatment is also described for simulations on multi-core computing architectures.

Modifications to the least-squares and Green–Gauss gradient reconstruction methods are proposed at the non-conformal mesh interface. The order of accuracy of the new schemes is derived analytically and a numerical verification of the results is presented for 2D and 3D domains. It is found that, in case of least-squares reconstruction, extending the stencil to the control volumes of the mesh block opposite of the interface leads to a first order convergence of the gradient along each spatial direction. Alternatively, the interface faces can be treated as external boundaries and their values can be set as a linear combination of the neighbors. In this case, the accuracy of the gradient reconstruction along the direction which crosses the interface is reduced to 0-order, thus preventing convergence as the mesh is refined.

The supermesh interface treatment is verified on five test cases featuring shock waves crossing the interface and the transport of viscous vortices. Numerical fluxes conservation is achieved to machine precision. The calculated flow fields show no spurious oscillations at the interface and agree with the results obtained on a single-block mesh, i.e., no interface. Numerical stability is demonstrated empirically by solving the equations with three different time integration schemes, namely explicit three-steps Runge–Kutta, implicit backward Euler and BDF2 methods, and by studying subsonic, transonic and supersonic flow regimes. The convergence rates were not found to be affected by the presence of the interface.

References

[1] Berger, M. J., 1987. "On conservation at grid interfaces". *SIAM J. Numer. Anal.,* **24**(5), pp. 967–984.

[2] Rai, M. M., 1986. "A conservative treatment of zonal boundaries for Euler equation calculations". *J. Comput. Phys.,* **62**(2), pp. 472–503.

[3] Hessenius, K. A., and Rai, M. M., 1986. "Applications of a conservative zonal scheme to transient and geometrically complex problems". *Computers and Fluids,* **14**(1), pp. 43–58.

[4] Rai, M. M., 1986. "An implicit, conservative, zonal-boundary scheme for Euler equation calculations". *Comput. Fluids,* **14**(3), pp. 295–319.

[5] Rai, M. M., 1987. "Navier-Stokes simulations of rotor/stator interaction using patched and overlaid grids". *J. Propul. Power,* **3**(5), pp. 387–396.

[6] Lerat, A., and Wu, Z. N., 1996. "Stable conservative multidomain treatments for implicit Euler solvers". *J. Comput. Phys.,* **123**(1), pp. 45–64.

[7] Benkenida, A., Bohbot, J., and Jouhaud, J. C., 2002. "Patched grid and adaptive mesh refinement strategies for the calculation of the transport of vortices". *Int. J. Numer. Meth. Fl.,* **40**(7), pp. 855–873.

[8] Zhang, Y., Chen, H., and Fu, S., 2011. "Improvement to patched grid technique with high-order conservative remapping method". *J. Aircraft,* **48**(3), pp. 884–893.

[9] Behr, M., and Tezduyar, T., 1999. "The shear-slip mesh update method". *Comput. Method. Appl. M.,* **174**(3-4), pp. 261–274.

[10] Behr, M., and Tezduyar, T., 2001. "Shear-slip mesh update in 3D computation of complex flow problems with rotating mechanical components". *Comput. Method. Appl. M.,* **190**(24-25), pp. 3189–3200.

[11] Wang, Y., Qin, N., Carnie, G., and Shahpar, S., 2013. "Zipper layer method for linking two dissimilar structured meshes". *J. Comput. Phys.,* **255**, pp. 130–148.

[12] Jiao, X., and Heath, M. T., 2004. "Common-refinement-based data transfer between non-matching meshes in multiphysics simulations". *Int. J. Numer. Meth. Eng.,* **61**(14), pp. 2402–2427.

[13] Gartling, D. K., 2005. "Multipoint constraint methods for moving body and non-contiguous mesh simulations". *Int. J. Numer. Meth. Fl.,* **47**(6-7), pp. 471–489.

[14] Benek, J. A., Steger, J. L., and Dougherty, F. C., 1983. "A flexible grid embedding technique with application to the Euler equations". In Computational Fluid Dynamics Conference 6^{th}, no. AIAA paper 83-1944.

[15] Benek, J. A., Buning, P. G., and Steger, J. L., 1985. "A 3-D CHIMERA grid embedding technique". In Computational Fluid Dynamics Conference 7^{th}, no. AIAA paper 85-1523.

[16] Wang, Z. J., 1995. "A fully conservative interface algorithm for overlapped grids". *J. Comput. Phys.,* **122**(1), pp. 96–106.

[17] Kao, K.-H., and Liou, M.-S., 1995. "Advance in overset grid schemes: From Chimera to DRAGON grids". *AIAA J.,* **33**(10), pp. 1809–1815.

[18] Wang, Z. J., Hariharan, N., and Chen, R., 2001. "Recent development on the conservation property of Chimera". *Int. J. Comput. Fluid D.,* **15**(4), pp. 265–278.

[19] Liu, Y., 2005. "Central schemes on overlapping cells". *J. Comput. Phys.,* **209**(1), pp. 82–104.

[20] Kurganov, A., and Tadmor, E., 2000. "New high-resolution central schemes for nonlinear conservation laws and convection-diffusion equations". *J. Comput. Phys.,* **160**(1), pp. 241–282.

[21] Chesshire, G., 1990. "Composite overlapping meshes for the solution of partial differential equations". *J. Comput. Phys.,* **90**(1), pp. 1–64.

[22] Flores, J., and Chaderjian, N. M., 1990. "Zonal Navier-Stokes methodology for flow simulation about a complete aircraf". *Journal of Aircfraft,* **27**(7), pp. 583–590.

[23] Tang, H. S., and Zhou, T., 2000. "On nonconservative algorithms for grid interfaces". *SIAM J. Numer. Anal.,* **37**(1), pp. 173–193.

[24] Farrell, P. E., Piggott, M. D., Pain, C. C., Gorman, G. J., and Wilson, C. R., 2009. "Conservative interpolation between unstructured meshes via supermesh construction". *Comput. Method. Appl. M.,* **198**(33–36), pp. 2632–2642.

[25] Menon, S., and Schmidt, D. P., 2011. "Conservative interpolation on unstructured polyhedral meshes: An extension of the supermesh approach to cell-centered finite-volume variables". *Comput. Method. Appl. M.,* **200**(41–44), pp. 2797–2804.

[26] Mavriplis, D., 2003. "Revisiting the least-squares procedure for gradient reconstruction on unstructured meshes". In AIAA paper, Vol. 3986, pp. 1–13.

[27] Liou, M.-S., 1996. "A sequel to AUSM: AUSM$^+$". *J. Comput. Phys.,* **129**(2), pp. 364–382.

[28] Toro, E. F., Spruce, M., and Speares, W., 1994. "Restoration of the contact surface in the HLL-Riemann solver". *Shock Waves,* **4**(1), pp. 25–34.

[29] Venkatakrishnan, V., 1995. "Convergence to steady state solutions of the Euler equations on unstructured grids with limiters". *J. Comput. Phys.,* **118**(1), pp. 120–130.

[30] Pecnik, R., Terrapon, V. E., Ham, F., Iaccarino, G., and Pitsch, H., 2012. "Reynolds-averaged Navier-Stokes simulations of the HyShot II scramjet". *AIAA J.,* **50**(8), pp. 1717–1732.

[31] Shu, C. W., and Osher, S., 1988. "Efficient implementation of essentially non-oscillatory shock-capturing schemes". *J. Comput. Phys.,* **77**(2), pp. 439–471.

[32] Rinaldi, E., Pecnik, R., and Colonna, P., 2014. "Exact Jacobians for implicit Navier–Stokes simulations of equilibrium real gas flows". *J. Comput. Phys.,* **270**, pp. 459–477.

[33] Erhard, J., and Gehrer, A., 2000. "Design and construction of a transonic test-turbine facility". In Proceedings of the ASME Turbo Expo, no. 2000-GT-480, pp. 1–8.

[34] Schennach, O., Pecnik, R., Paradiso, B., Göttlich, E., Marn, A., and Woisetschläger, J., 2008. "The effect of vane clocking on the unsteady flow field in a one-and-a-half stage transonic turbine". *J. Turbomach.,* **130**(3), p. 031022.

[35] Spalart, P. R., and Allmaras, S. R., 1994. "One-equation turbulence model for aerodynamic flows". *Rech. Aerospatiale*(1), pp. 5–21.

4

CFD simulation of a supercritical CO_2 compressor performance map

The contents of this chapter appeared in:

Rinaldi, E., Pecnik, R., and Colonna, P., 2015. *J. Eng. Gas Turb. Power*, **137**, pp. 072602

Abstract *The performance map of a radial compressor operating with supercritical CO_2 is computed by means of three dimensional steady state Reynolds-averaged Navier–Stokes simulations. The geometry investigated is part of a 250kW prototype which was tested at Sandia National Laboratories (SNL). An in-house fluid dynamic solver is coupled with a look-up table algorithm to evaluate the fluid properties. Tables are generated using a multiparameter equation of state, which ensures high accuracy in the fluid characterization. The compressor map is calculated considering three different rotational speeds (45 krpm, 50 krpm, and 55 krpm). For each speed-line several mass flow rates are simulated. Numerical results are compared to experimental data from SNL to prove the potential of the methodology.*

4.1 Introduction

The idea of using supercritical carbon dioxide (sCO_2) as the working fluid of closed loop Brayton cycle turbines for energy conversion was first studied in the late sixties by Angelino[1] and Feher[2]. The main advantage of this cycle configuration is the much higher conversion efficiency reachable at moderate maximum cycle temperatures, compared to competing technologies. This is possible because of the small work needed to compress the fluid close to its vapor-liquid critical point, and of the use of a high degree of regeneration. A further advantage of sCO_2 power cycle turbines is the high power density which leads to compact general assemblies, due to the high operating fluid densities and pressures.

These studies were recently resumed by the scientific community because of the high potential of using sCO_2 cycles in next-generation nuclear reactors[3–6], or to exploit low/medium temperature renewable energy sources, such as solar radiation[7–10]. This interest led to the realization of several proof-of-concept test loop facilities, as for example the one operating at Sandia National Laboratories[11,12].

Despite the fervid activity, no commercial sCO_2 power unit is currently operational. Among the challenges that need to be faced to bring this technology to the market we list the development of robust control strategies, the realization of cost effective compact heat exchangers, and the improvement of the turbomachinery performance. While significant progress has been made in the design of turbomachinery operating with fluids behaving as ideal gases, only recently the interest shifted to non-conventional machines operating with dense vapors or supercritical fluids[13–18]. Although simple one dimensional or surrogate models are commonly used for preliminary designs, only accurate fluid dynamic simulations can provide important insights on the flow field that can be used to improve the machine aerodynamics, and therefore its performance. Difficulties in the simulation and analysis of flows evolving close to the fluid vapor-liquid critical point arise from the highly nonlinear variations of the fluid thermophysical properties in this region.

This paper presents a methodology for the computational fluid dynamic (CFD) simulation of the compressible flow of sCO_2 in a radial compressor. The component analyzed is part of a 250 kW prototype investigated experimentally by Wright *et al.*[11]. A Reynolds-averaged Navier–Stokes solver[19] was coupled to a multiparameter equation of

state model to evaluate the thermophysical properties of the fluid[20,21]. A brief overview of the real gas CFD code is provided in the following, together with a description of the compressor geometry and computational mesh. Three dimensional steady state simulations were performed using a mixing-plane to treat the rotor-diffuser interface at three different rotational speeds of the impeller (45 krpm, 50 krpm, and 55 krpm), and for several mass flow rates. Finally, numerical results are compared to experiments and discussed.

4.2 CFD solver for dense vapor and supercritical fluid flows

The compressible Reynolds-averaged Navier–Stokes equations were solved using the CFD code developed by Pecnik *et al.*[19]. The solver is based on a cell-centered finite volume formulation on unstructured arbitrary polyhedral meshes. It uses a subdomain decomposition through the freely available package Parmetis[22] and the Message Passing Interface as the parallel infrastructure. The equations are discretized in the conservative form

$$\frac{\partial}{\partial t}\int_{\Omega}\mathbf{U}d\Omega+\int_{\partial\Omega}\left(\mathbf{F}_c\left(\mathbf{U}\right)-\mathbf{F}_d\left(\mathbf{U}\right)\right)dA=\int_{\Omega}\mathbf{S}d\Omega. \tag{4.1}$$

$\mathbf{U}=\mathbf{U}(\mathbf{x},t)=(\rho,m,E^{\mathrm{t}})^{\mathrm{T}}$ represents the conserved variables vector, with ρ being the density, $\mathbf{m}=\rho\mathbf{v}$ the Cartesian momentum, and $E^{\mathrm{t}}=\rho(e+\frac{1}{2}|\mathbf{v}|^2)$ the total internal energy. $\mathbf{F}_c(\mathbf{U})$ and $\mathbf{F}_d(\mathbf{U})$ are the convective and diffusive fluxes, $\mathbf{S}$ the source term, and Ω and $\partial\Omega$ are the physical domain of interest and its boundary.

The fluxes and source term vectors are expressed for a rotating non-inertial reference frame as

$$\mathbf{F}_c(\mathbf{U})=\begin{pmatrix}\mathbf{n}\cdot\rho\left(\mathbf{v}-\mathbf{v}^m\right)\\ \rho\mathbf{v}\left(\mathbf{n}\cdot\left(\mathbf{v}-\mathbf{v}^m\right)\right)+P\mathbf{n}\\ \left(E^{\mathrm{t}}+P\right)\left(\left(\mathbf{v}-\mathbf{v}^m\right)\cdot\mathbf{n}\right)+P\left(\mathbf{v}^m\cdot\mathbf{n}\right)\end{pmatrix}, \tag{4.2}$$

$$\mathbf{F}_d(\mathbf{U})=\begin{pmatrix}0\\ \mathbf{n}\cdot\Pi\\ \mathbf{v}\cdot\left(\mathbf{n}\cdot\Pi\right)+\mathbf{n}\cdot\left(\lambda\nabla T\right)\end{pmatrix}, \tag{4.3}$$

$$\mathbf{S}(\mathbf{U})=\begin{pmatrix}0\\ -\rho\left(\boldsymbol{\omega}\times\mathbf{v}\right)\\ 0\end{pmatrix}, \tag{4.4}$$

where $\boldsymbol{\omega}$ denotes the angular velocity of the rotating non-inertial reference frame, $\mathbf{v}^m=\boldsymbol{\omega}\times\mathbf{r}$, P the pressure, Π the stress tensor, λ the thermal conductivity, T the temperature, and $\mathbf{n}$ the outward pointing unit vector normal to the surface.

The convective fluxes are discretized using the AUSM$^+$ approximate Riemann solver proposed by Liou[23]. Second order accuracy is achieved using a suitable interpolation scheme (least-squares gradient) to reconstruct the state $(\rho,\mathbf{v},P)$ at each cell face. The

slope limiter proposed by Venkatakrishnan [24] and later modified by one of the authors [19] is used to reduce the discrete gradients to guarantee the monotonicity of the reconstructed variable at the face center. In order to ensure thermodynamic consistency of the reconstructed state, the fluid state is evaluated at the faces using the interpolated density and pressure.

The diffusive fluxes discretization needs an accurate and efficient evaluation of the gradients at the cell faces. Following Kim *et al.* [25], the velocity and temperature gradients at the faces are calculated as

$$\nabla\phi|_f \cdot \mathbf{n}_f = \frac{\phi_A - \phi_B}{|\mathbf{x}_A - \mathbf{x}_B|}\alpha_f + \frac{1}{2}\left(\nabla\phi|_A + \nabla\phi|_B\right) \cdot \left(\mathbf{n}_f - \alpha_f \mathbf{s}_f\right), \tag{4.5}$$

where ϕ is a generic variable, A and B the two cell centers sharing the face f, and $\alpha = \mathbf{s} \cdot \mathbf{n}$.

The set of equations is closed using the k–ω shear stress transport model of Menter [26], which represents a standard choice in turbomachinery flows computations.

In order to increase the robustness of the simulations, first order accuracy was used for the convective fluxes, while the diffusive fluxes were discretized using a second order scheme.

Equations are implicitly integrated in time using the backward Euler scheme to allow for the choice of large time steps. A newly introduced implicit formulation of AUSM$^+$ is adopted, while the diffusive fluxes Jacobian is expressed in the form suggested by Pulliam and Steger [27]. The Jacobians of the convective and diffusive fluxes expressed for a fluid governed by a complex equation of state are taken from Rinaldi *et al.* [28]. The large sparse system resulting from the fluxes linearization is solved using PETSc [29].

4.2.1 Thermophysical model

In order to accurately estimate the thermodynamic and transport properties of the supercritical fluid, a reference model based on the multiparameter equation of state of Span and Wagner [20] is used. The viscosity is computed based on the work of Fenghour *et al.* [30], while the other transport properties are based on Vesovic *et al.* [31]. A look-up table interpolation method recently developed by the authors couples the solver to the evaluation of fluid properties in order to greatly reduce the computational time [28]. The property table is obtained with an in-house library [32], which links to a well-known thermodynamic property program [21] for the evaluation of primary properties, while it relies on its own routines for the evaluation of secondary or derived properties (e.g., the pressure and temperature derivatives needed for the implicit time integration). The tabulated region is split into separate single phase and two-phase property tables to avoid large interpolation errors which would occur for states lying close to the vapor-liquid saturation lines, because some properties (e.g., the speed of sound or pressure derivatives) are discontinuous across the boundary separating the single phase and vapor-liquid equilibrium (VLE) states. The number of nodes of the tables used in the simulations was chosen in order to guarantee that the maximum interpolation error in the whole tabulated region is below 0.1%.

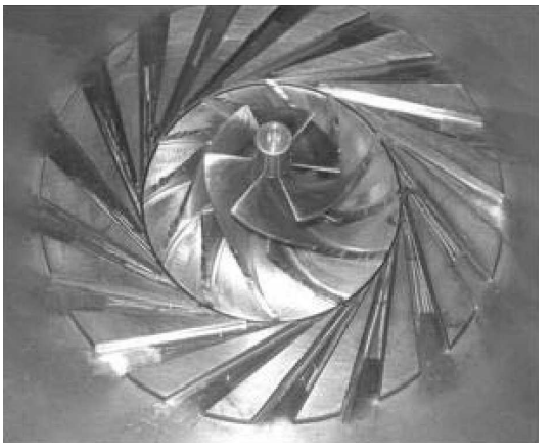

Figure 4.1: Impeller and diffuser geometry [11]

4.2.2 Boundary conditions

Constant total conditions and turbulence properties were specified at the compressor inlet, see Tab. 4.2, while a constant static pressure was set at the diffuser outlet. A no-slip boundary condition was applied at the walls, which were modeled as adiabatic. The mixing-plane approach [33] was applied to treat the interface between rotor and diffuser.

4.3 Geometry and computational mesh

The investigated case is the single stage radial compressor operating in the proof-of-concept test loop facility at Sandia National Laboratories, and is shown in Fig. 4.1. The rotor consists of 6 main blades and 6 splitter blades, while the diffuser is made of 17 wedge shaped blades. The geometrical specifications are taken from Wright *et al.* [11] and summarized in Tab. 4.1. They were used to generate the three dimensional geometry by means of a commercial software [34].

An in-house hybrid mesh generator was used to generate a flexible and high quality computational grid. The adopted software employs a geometry transformation tailored to turbomachinery geometries, which reduces the complexity of the mesh generation from three to two dimensions. The original geometry is discretized into several constant span level surfaces in the physical space (x, y, z). The frame of reference is then changed to (M, ϕ, s), with M being the normalized meridional length, ϕ the azimuthal angle, and s the normalized span. The surfaces can be therefore meshed using two dimensional grid generation schemes in the transformed space. The planes are finally transformed back to the physical space, and a node interpolation in the spanwise direction is performed in order to fill the whole three dimensional domain. In the present study, five equally spaced span level surfaces were employed.

Table 4.1: Main compressor dimensions[11]

Inlet shroud radius	9.3720 mm
Inlet hub radius	2.5375 mm
Exit blade height	1.7120 mm
Exit blade radius	18.6817 mm
Blade thickness	0.762 mm
Tip clearance	0.254 mm
Radial rotor/diffuser blades gap	0.3 mm
Inlet Blade Angle at tip	50 deg
Exit blade back sweep angle	-50 deg
Exit vaned diffuser angle	71.5 deg
Diffuser blade divergence angle	13.17 deg

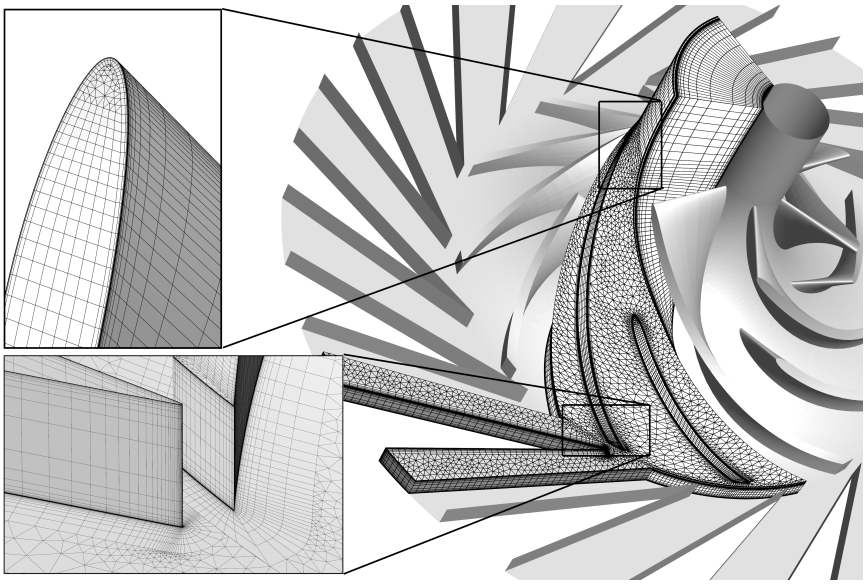

Figure 4.2: Three dimensional view of the computational mesh used to model the rotor and the diffuser vanes. The grid counts approximately 8×10^5 cells, which are clustered at the walls to ensure $y^+ \approx 1$. Hexahedral cells were used for the blades boundary layers and at the inlet of the rotor, while wedge cells were placed elsewhere. Detailed views are shown for the surface mesh of the rotor main blade, diffuser wedge, and the interface between rotor and diffuser.

An O-type structured mesh was used around the blades, and the elements were clustered at the walls to have the correct resolution of the boundary layers. The normal-to-wall velocity profile was fully resolved using a sufficiently fine grid, $y^+ \approx 1$ at the walls. An

unstructured triangulation[35] was used for the remaining part of the domain. In order to have the same mesh topology in terms of connectivity and number of nodes on the five planes (needed for the interpolation in the spanwise direction), the unstructured triangulation was performed at the hub only ($s = 0$), and morphed and smoothed (using a Laplacian scheme) on the other levels to match the new boundaries. The impeller and the tip clearance gap were meshed separately using 39 and 19 elements in the spanwise direction, respectively. The discretization of the diffuser was straightforward due to the simplicity of the geometry. At the leading edge of the diffuser blade a small curvature was introduced to remove numerical problems due to the sharp corner.

The periodicity of the geometry and the steady flow assumption allow to simulate only one passage of the rotor and one of the diffuser using about 6.5×10^5 and 1.5×10^5 elements respectively. The mesh resolution was refined with respect to previous studies[18], in order to ensure more accurate results. Figure 4.2 shows the modeled compressor geometry and the computational grid, with detailed views of the main blade leading and trailing edge and of the interface region.

4.4 Discussion of the CFD model and of the available experimental data

4.4.1 Numerical model

A critical aspect of the fluid dynamic modeling of the problem under investigation is the treatment of fluid condensation. Previous studies[18,36,37] indicated that the fluid thermodynamic state falls in the VLE region near the leading edge of the main compressor blade. Since the main goal of this investigation is the estimation of the typical performance parameters with engineering accuracy, the adoption of the single-fluid model allows to avoid a considerable increase of complexity. Therefore, the homogeneous mixture approximation was used for the thermodynamic states lying inside the vapor-liquid equilibrium region. Properties were averaged based on the vapor quality, and metastable states were not considered.

This modeling choice is further justified by the lack of accurate nucleation models close to the critical point and of experimental data against which the extended fluid flow model could be validated. Moreover, the small density differences between the liquid and vapor phases close to the critical point suggest that the influence of this modeling approximation on the results is marginal, given the small dimension of the regions where the thermodynamic state falls inside the dome. In addition to that, Baltadjiev *et al.*[37] and Lettieri *et al.*[38] shown that in practice the short residence time of the flow prevents condensation from taking place (their results were however obtained for operating conditions farther from the critical point than the ones studied in this paper).

A general limitation of RANS modeling, especially for supercritical flows, is the reliability of turbulence models to accurately mimic the effects of turbulence. Most of the models were developed and calibrated for incompressible flows of gases obeying to the ideal gas law, and for simple geometries. For a comprehensive assessment the reader is

referred to the work of He *et al.*[39]. One of the issues is the definition of the effective thermal conductivity, which is commonly modeled as the sum of molecular λ and turbulent thermal conductivity λ_{tur}, $\lambda_{\text{eff}} = \lambda + \lambda_{\text{tur}}$, with $\lambda_{\text{tur}} = c_P \mu_{\text{tur}} / Pr_{\text{tur}}$, and μ_{tur} and Pr_{tur} the turbulent viscosity and turbulent Prandtl number, respectively. While the turbulent Prandtl number can be assumed constant for an ideal gas flow, it varies significantly for a supercritical flow[40,41]. Furthermore, the value of the fluid specific heat capacity c_P is not defined in the homogeneous mixture model if the thermodynamic state is in the VLE region. For these reasons, λ_{tur} was not included in the heat transfer term in the energy equation. This modification to the equations is not expected to affect significantly the results since strong temperature gradients are not present in the flow field and the assumption of adiabatic walls was used.

4.4.2 Experimental data

The inlet conditions were taken from Wright *et al.*[11], however the values applied in the simulations may differ from the ones measured during the experimental campaign. In fact, the report does not specify the exact location of the sensors and whether the measured inlet quantities are total or static. In this work, constant total conditions were assumed and the reported values were interpreted as such.

It is worth mentioning that applying constant static conditions instead of total conditions can result in significant changes in the inlet fluid properties for states close to the critical point. This is due to the strong non-linearities and the large density, which leads to large differences between static and total conditions even for small velocities. For example, for the condition with the largest mass flow rate considered in this work, $\Delta P / P_{\text{tot}} = \frac{1}{2} \rho_{\text{in}} U_{\text{in}}^2 / P_{\text{tot}} \approx 2.5\%$. Accordingly, the transport properties change as $\Delta\mu/\mu_{\text{in}} \approx 1.7\%$, $\Delta c_P / c_{P,\text{in}} \approx 41\%$, $\Delta\lambda/\lambda_{\text{in}} \approx 14\%$.

In addition, the measured inlet conditions are given within ranges of pressure $P = [77, 81.39]$ bar and temperature $T = [304.3, 307]$ K. The uncertainty on pressure and temperature translates into a large density range $\rho = [345, 690]$ kg/m^3.

Furthermore, the compressor map measured experimentally in Ref.[11] is also affected by uncertainties related to measurement equipment, flow leakage, windage losses, etc., which are not taken into account in the CFD simulations.

4.5 Results

The compressor map was calculated by performing steady state simulations at three different rotational speeds, namely 45 krpm, 50 krpm, and 55 krpm. The inlet conditions are reported in Tab. 4.2.

Figure 4.3 shows the averaged inlet and outlet states of all simulations in the T-s diagram. Iso-pressure and iso-enthalpy lines in the range of the outlet values are also shown. Note, all the compression processes cross the pseudo-critical line for the conditions considered, which is the locus of thermodynamic states where the specific heat at constant pressure peaks and where transition between liquid-like and vapor-like behavior occurs.

The compressor performance is assessed in Fig. 4.4 in terms of isentropic efficiency $\eta = (h_{out,s} - h_{in})/(h_{out} - h_{in})$ and specific enthalpy rise. Numerical results are compared with experimental data from Wright *et al.*[11]. The calculated efficiency curves are reasonably close to the experimental data, showing a slight shift towards low flow coefficients. The difference between numerical values and experiments is within an arguably acceptable range, given the limitations discussed in the previous section. The specific enthalpy rise obtained from the simulations shows a nearly linear dependence on the flow coefficient. Therefore, the presented simulations do not capture the compressor surge at low mass flow rates and high pressure ratios (which is clearly visible in the experimental data). The order of accuracy of the convective fluxes discretization is expected to play an important role in the representation of the loss mechanisms (e.g., flow separations), and as a consequence

Table 4.2: Inlet boundary conditions[11]. $Tu = \sqrt{2/3k}/U$ is the inlet turbulence intensity, with k being the turbulent kinetic energy and U the average velocity at the inlet. $Re_T = \sqrt{k}L\rho/\mu$ is the inlet turbulent Reynolds number. Tu and Re_T are used to calculate the inlet values of turbulent kinetic energy and specific dissipation ω used by the turbulence model.

P_{tot} [bar]	T_{tot} [°C]	Tu [%]	Re_T [-]
76.9	32.8	5	100

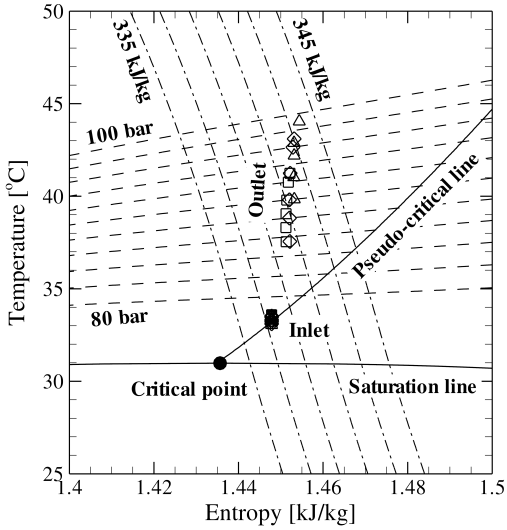

Figure 4.3: Average inlet and outlet states. Symbols correspond to 45 krpm (squares), 50 krpm (diamonds), and 55 krpm (triangles).

in the performance prediction. The fact that no back-flow or recirculation is allowed at the outlet of the diffuser can also influence the results when the operating conditions are close to surge.

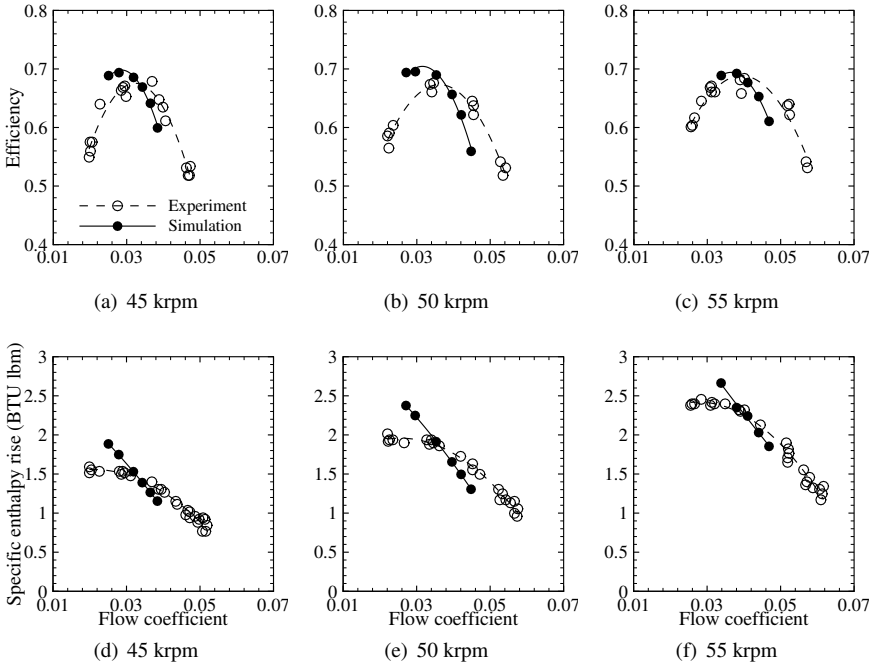

Figure 4.4: Compressor performance map

Pressure contours are depicted in Fig. 4.5 at half of the span height for two mass flow rates and at a rotational speed of 55 krpm. The distribution is smooth due to the small value of the relative Mach number in the rotor, which reaches about $M = 0.5$ at the interface location. Figure 4.5 (a) corresponds to the calculated maximum efficiency for the considered speed line, whereby the velocity angle at the inlet of the diffuser is well aligned with the diffuser blade, and the diffuser recovers pressure efficiently. A small stagnation region can be identified by the high pressure at the leading edge of the blade. As the mass flow increases, see Fig. 4.5 (b) which corresponds to the minimum efficiency of the 55 krpm speed line, the flow at the outlet of the rotor has a larger radial component. For this reason, it impinges on one side of the diffuser blade, leading to a large stagnation region which affects the overall pressure recovery in the diffuser vane. Moreover, the flow accelerates around the blade leading edge determining a small low pressure region.

Finally, it is possible to identify regions of the domain where the calculated thermodynamic states are located inside the VLE region, therefore where there is the possibility for CO_2 to condense. As already mentioned, this phenomenon has not been modeled in the presented simulations. Nevertheless, qualitative conclusions can still be drawn from the

analysis of the computed flow fields. Figures 4.6 and 4.7 present the predicted two-phase flow regions for the three considered rotational speeds, at nearly constant flow coefficients. At the leading edge of the compressor main blade, shown in Fig. 4.6, the surface which delimits the single phase and the two-phase region becomes larger for increasing rotational speeds, and is stretched in the direction of the hub. This was not observed at the leading edge of the splitter blade, where the fluid state is in the vapor single phase for each simulated condition. Given the high value of the design rotational speed, namely 75 krpm, the predicted two-phase regions are expected to increase significantly. Because of the proximity to the critical point of the inlet state, conditions for condensation can be met and consequently the modeling of two-phase flow can be important in order to predict the flow accurately.

A similar phenomenon occurs at the trailing edge of both blades, as depicted in Fig. 4.7, where the flow acceleration around the sharp corners determines a large drop in the static pressure, see Fig. 4.5. However, the dependence on the rotational speed is weaker and appears reversed. The largest region is observed for the lowest rotational speed.

For high mass flows, a two-phase flow region is predicted at the diffuser leading edge also. This can be explained referring to Fig. 4.5 (b). When the inlet flow angle is not aligned with the diffuser blade, the large acceleration around the sharp leading edge is such that the thermodynamic state falls below the saturation lines.

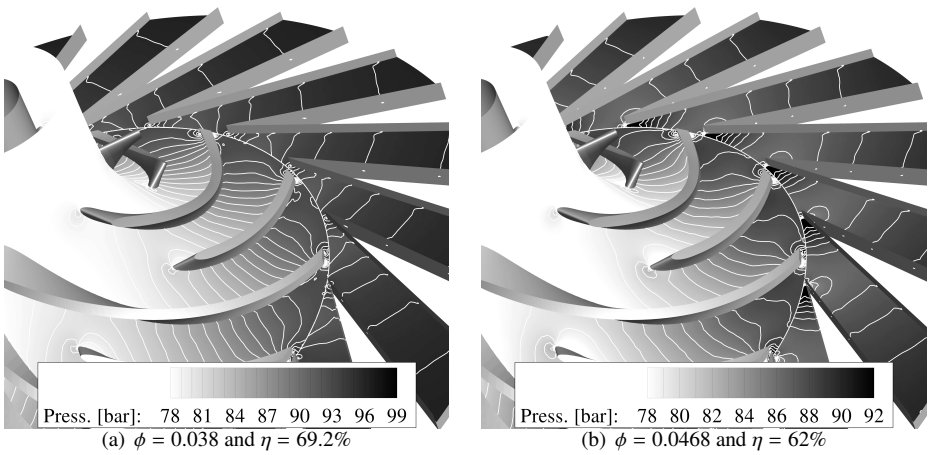

(a) ϕ = 0.038 and η = 69.2% (b) ϕ = 0.0468 and η = 62%

Figure 4.5: Contours of pressure at 50% of the span and 55 krpm

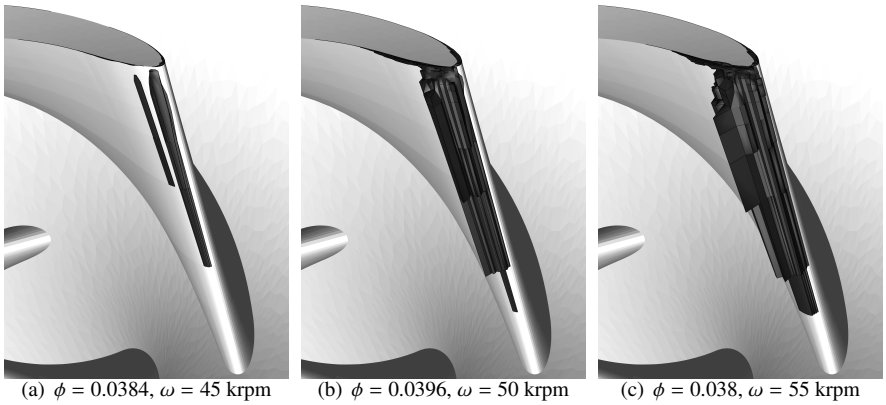

(a) ϕ = 0.0384, ω = 45 krpm (b) ϕ = 0.0396, ω = 50 krpm (c) ϕ = 0.038, ω = 55 krpm

Figure 4.6: Main blade leading edge: control volumes where the thermodynamic state is in the VLE region

(a) ϕ = 0.0384, ω = 45 krpm (b) ϕ = 0.0396, ω = 50 krpm (c) ϕ = 0.038, ω = 55 krpm

Figure 4.7: Main and splitter blade trailing edge: control volumes where the thermodynamic state is in the VLE region

4.6 Conclusions

The performance map of a radial compressor operating with supercritical CO_2 was calculated by means of three dimensional steady state simulations. The in-house computational tool is formed by a parallel RANS solver for unstructured grids obtaining fluid thermophysical properties thanks to a look-up table interpolation method. Thermophysical fluid property tables are generated with an in-house program implementing state-of-the-art models, allowing for accurate predictions even close to the fluid critical point and in the vapor-liquid equilibrium region.

Numerical results were compared to experimental data over a range of mass flow rates and for three values of the impeller rotational speed. The qualitative and quantitative prediction of the compressor isentropic efficiency was satisfactory, however showing a shift of the optimal operating condition towards low values of the flow coefficient. The specific enthalpy rise of the fluid predicted with simulations depends linearly on the mass flow, differently from values measured from experiments. Furthermore, the compressor surge could not be simulated due to the limitations of the model.

The difference between experimental and numerical results was discussed by addressing the limitations of the adopted models and those related to the experimental data.

The computed flow fields showed a smooth variation of fluid properties, and allowed to gain insights on the compressor performance degradation for high mass flow rates. Simulations also highlighted the possibility of CO_2 condensation in some regions of the domain, and allowed the study of the dependence of their extent on the impeller rotational speed. The volume of calculated thermodynamic states lying in the VLE region at the leading edge of the impellers is predicted to grow for increasing rotational speeds. A similar phenomenon with a weaker dependence on the rotational speed was observed at the trailing edge of both the main and the splitter blades, however with a reversed dependence on the rotational speed if compared to the main blade leading edge.

In conclusion, the potential of using three dimensional CFD simulations for the improvement of the aerodynamic design of non-conventional turbomachinery, such as the ones operating with supercritical fluids, was demonstrated. Although models can still be improved to a large extent, they can provide reasonable performance predictions and valuable information about the flow field that can be used in the design process.

References

[1] Angelino, G., 1968. "Carbon dioxide condensation cycles for power production". *ASME J. Eng. Power,* **10**, July, pp. 287–295.

[2] Feher, E. G., 1968. "The supercritical thermodynamic power cycle". *Ennerg. Convers.,* **8**, pp. 85–90.

[3] Dostal, V., Hejzlar, P., and Driscoll, M. J., 2006. "High-performance supercritical carbon dioxide cycle for next-generation nuclear reactors". *Nucl. Technol.,* **154**(3), pp. 265–282.

[4] Dostal, V., Hejzlar, P., and Driscoll, M. J., 2006. "The supercritical carbon dioxide power cycle: Comparison to other advanced power cycles". *Nucl. Technol.,* **154**(3), pp. 283–301.

[5] Ishiyama, S., Muto, Y., Kato, Y., Nishio, S., Hayashi, T., and Nomoto, Y., 2008. "Study of steam, helium and supercritical CO_2 turbine power generations in prototype fusion power reactor". *Prog. Nucl. Energ.,* **50**(2–6), pp. 325–332.

[6] Kim, Y. M., Kim, C. G., and Favrat, D., 2012. "Transcritical or supercritical CO_2 cycles using both low- and high-temperature heat sources". *Energy,* **43**(1), pp. 402–415.

[7] Yamaguchi, H., Sawada, N., Suzuki, H., Ueda, H., and Zhang, X.-R., 2010. "Preliminary study on a solar water heater using supercritical carbon dioxide as working fluid". *J. Sol. Energ.-T. ASME,* **132**(1), p. 011010.

[8] Garg, P., Kumar, P., and Srinivasan, K., 2013. "Supercritical carbon dioxide Brayton cycle for concentrated solar power". *J. Supercrit. Fluid.,* **76**, pp. 54–60.

[9] Iverson, B. D., Conboy, T. M., Pasch, J. J., and Kruizenga, A. M., 2013. "Supercritical CO_2 Brayton cycles for solar-thermal energy". *Appl. Energ.,* **111**, pp. 957–970.

[10] Turchi, C. S., Ma, Z., Neises, T. W., and Wagner, M. J., 2013. "Thermodynamic study of advanced supercritical carbon dioxide power cycles for concentrating solar power systems". *J. Sol. Energ.-T. ASME,* **135**(4), p. 041007.

[11] Wright, S. A., Radel, R. F., Vernon, M. E., Rochau, G. E., and Pickard, P. S., 2010. Operation and analysis of a supercritical CO_2 brayton cycle. SANDIA REPORT SAND2010-0171, Sandia National Laboratories.

[12] Conboy, T., Wright, S., Pasch, J., Fleming, D., Rochau, G., and Fuller, R., 2012. "Performance characteristics of an operating supercritical CO_2 Brayton cycle". *J. Eng. Gas Turb. Power,* **134**(11), p. 111703.

[13] Boncinelli, P., Rubechini, F., Arnone, A., Cecconi, M., and Cortese, C., 2004. "Real gas effects in turbomachinery flows: A computational fluid dynamics model for fast computations". *J. Turbomach.,* **126**(2), pp. 268–276.

[14] Colonna, P., Harinck, J., Rebay, S., and Guardone, A., 2008. "Real-gas effects in organic Rankine cycle turbine nozzles". *J. Propul. Power,* **24**(2), pp. 282–294.

[15] Harinck, J., Guardone, A., and Colonna, P., 2009. "The influence of molecular complexity on expanding flows of ideal and dense gases". *Phys. Fluids,* **21**(8), pp. 1–14.

[16] Harinck, J., Colonna, P., Guardone, A., and Rebay, S., 2010. "Influence of thermodynamic models in two-dimensional flow simulations of turboexpanders". *J. Turbomach.,* **132**(1), pp. 1–17.

[17] Congedo, P. M., Corre, C., and Cinnella, P., 2011. "Numerical investigation of dense-gas effects in turbomachinery". *Comput. Fluids,* **49**(1), pp. 290–301.

[18] Pecnik, R., Rinaldi, E., and Colonna, P., 2012. "Computational fluid dynamics of a radial compressor operating with supercritical CO_2". *J. Eng. Gas Turb. Power,* **134**(12), p. 122301.

[19] Pecnik, R., Terrapon, V. E., Ham, F., Iaccarino, G., and Pitsch, H., 2012. "Reynolds-averaged Navier-Stokes simulations of the HyShot II scramjet". *AIAA J.,* **50**(8), pp. 1717–1732.

[20] Span, R., and Wagner, W., 2003. "Equations of state for technical applications. I. Simultaneously optimized functional forms for nonpolar and polar fluids". *Int. J. Thermophys.,* **24**(1), pp. 1–39.

[21] Lemmon, E. W., McLinden, M. O., and Huber, M. L., 2002. NIST standard reference database 23: Reference fluid thermodynamic and transport properties-REFPROP, version 8.0. Tech. rep., National Institute of Standards and Technology, Standard Reference Data Program, Gaithersburg.

[22] Karypis, G., Schloegel, K., and Kumar, V., 1997. PARMETIS: Parallel graph partitioning and sparse matrix ordering library. Tech. rep., University of Minnesota, Department of Computer Science and Engineering.

[23] Liou, M.-S., 1996. "A sequel to AUSM: AUSM$^+$". *J. Comput. Phys.,* **129**(2), pp. 364–382.

[24] Venkatakrishnan, V., 1995. "Convergence to steady state solutions of the Euler equations on unstructured grids with limiters". *J. Comput. Phys.,* **118**(1), pp. 120–130.

[25] Kim, S.-E., Makarov, B., and Caraeni, D., 2003. "A multi-dimensional linear reconstruction scheme for arbitrary unstructured grids". *AIAA paper,* **No. 2003-3990**, p. 2003.

[26] Menter, F. R., 1994. "Two-equation eddy-viscosity turbulence models for engineering applications". *AIAA J.,* **32**(8), pp. 1598–1605.

[27] Pulliam, T. H., and Steger, J. L., 1985. "Recent improvements in efficiency, accuracy, and convergence for implicit approximate factorization algorithms".

[28] Rinaldi, E., Pecnik, R., and Colonna, P., 2014. "Exact Jacobians for implicit Navier–Stokes simulations of equilibrium real gas flows". *J. Comput. Phys.,* **270**, pp. 459–477.

[29] Satish, B., Buschelman, K., Eijkhout, V., Gropp, W. D., Kaushik, D., Knepley, M. G., McInnes, L. C., Smith, B. F., and Zhang, H., 2009. "PETSc Web page, http://www.mcs.anl.gov/petsc".

[30] Fenghour, A., Wakeham, W. A., and Vesovic, V., 1998. "The viscosity of carbon dioxide". *J. Phys. Chem. Ref. Data,* **27**(1), pp. 31–39.

[31] Vesovic, V., Wakeham, W. A., Olchowy, G. A., Sengers, J. V., Watson, J. T. R., and Millat, J., 1990. "The transport properties of carbon dioxide". *J. Phys. Chem. Ref. Data,* **19**(3), pp. 763–808.

[32] Colonna, P., van der Stelt, T. P., and Guardone, A., 2012. FluidProp (Version 3.0): A program for the estimation of thermophysical properties of fluids. http://www.fluidprop.com/. A program since 2004.

[33] Denton, J. D., 1992. "The calculation of three-dimensional viscous through multistage turbomachines". *J. Turbomach.,* **114**(1), pp. 18–26.

[34] ANSYS, 2009. ANSYS BladeGen, release 13.0 users guide. Tech. rep., ANSYS, Inc., Canonsburg, PA.

[35] Shewchuk, J. R., 2002. "Delaunay refinement algorithms for triangular mesh generation". *Comp. Geom.-Theor. Appl.,* **22**(1–3), pp. 21–74.

[36] Rinaldi, E., Pecnik, R., and Colonna, P., 2013. "Steady state CFD investigation of a radial compressor operating with supercritical CO_2". In Proceedings of ASME Turbo Expo 2013, pp. 1–11.

[37] Baltadjiev, N., Lettieri, C., and Spakovszky, Z., 2014. "An investigation of real gas effects in supercritical CO_2 centrifugal compressors". In Proceedings of the ASME Turbo Expo, pp. 1–13.

[38] Lettieri, C., Yang, D., and Spakovszky, Z., 2014. "An investigation of condensation effects in supercritical carbon dioxide compressors". In The 4th International Symposium - Supercritical CO2 Power Cycles, pp. 1–15.

[39] He, S., Kim, W. S., and Bae, J. H., 2008. "Assessment of performance of turbulence models in predicting supercritical pressure heat transfer in a vertical tube". *Int. J. Heat Mass Tran.,* **51**(19-20), pp. 4659–4675.

[40] Yoo, J. Y., 2013. "The turbulent flows of supercritical fluids with heat transfer". *Annu. Rev. Fluid Mech.,* **45**(1), pp. 495–525.

[41] Nemati, H., Patel, A., Boersma, B. J., and Pecnik, R., 2013. "Direct numerical simulation of turbulent flow with supercritical fluid in a heated pipe". In International Symposium on Turbulence and Shear Flow Phenomena (TSFP-8), pp. 1–6.

5

Stator/rotor interaction in a supersonic ORC turbine

Part of the contents of this chapter appeared in:

Rinaldi, E., Pecnik, R., & Colonna, P., 2015. *J. Turbomach., Under Review*.

Abstract *Organic Rankine cycle (ORC) turbogenerators are the most viable option to convert sustainable energy sources in the low-to-medium power output range (from tens of kW to several MW). While the working principle is the same as that of steam power plants, the working fluid is a complex organic compound and the turbine expansion encompasses thermodynamic states in the dense vapour region, where the ideal gas assumption does not hold. This work addresses the challenge of simulating the highly unsteady supersonic flow of a non-ideal fluid through high expansion ratio and high-speed ORC turbines, and of characterizing its effect on unsteady blade loading and turbine efficiency. Detailed unsteady Reynolds-averaged Navier–Stokes simulations of a radial inflow 150 kW turbine are documented. The expansion ratio is larger than 100 and the maximum Mach number in the stator passage is approximately 2.8. The results indicate that the blade loading fluctuations are of the same order of magnitude of the static loads, which signifies the importance of taking unsteady effects into account in designing optimal and reliable high-speed supersonic ORC turbines.*

5.1 Introduction

Organic Rankine cycle (ORC) turbogenerators are a widely recognized technology for the conversion of low-to-medium temperature heat sources in the low power output range (from few kW_e to few MW_e). Suitable external thermal energy sources are the waste heat from industrial processes or engines, biomass combustion, solar radiation and geothermal reservoirs. While the working principle of the cycle is that of the steam Rankine cycle, the use of an organic compound gives an additional degree of freedom to the designer. An optimal fluid can be selected in order to best match the temperature profile of the external thermal energy source and sink and in order to obtain an optimal turbine design. A measure of the increasing utilization of ORC power plants around the world is given by the cumulative global capacity, which has now reached approximately 2,000 MW_e and is rapidly increasing. A recent review paper by Colonna *et al.* [(1)] summarizes the history, characteristics and perspective of this technology.

An organic working fluid gives an intrinsic advantage in the design of an efficient low power output turbine, if compared to a steam turbine, due to its different thermo-physical properties: for a given power output it is possible to design a turbine with a smaller number of stages, lower rotational speed, and higher volumetric flow due to the smaller enthalpy decrease over the expansion in case the fluid is an organic compound. Furthermore, the so-called retrograde behaviour of many ORC working fluids allows for a fully dry expansion, thus avoiding issues related to condensation, like blade erosion and efficiency penalty. However, what makes the design and realization of efficient ORC turbines challenging is the fact that the expansion occurs partially in the so-called dense vapour region, whereby the thermophysical fluid properties differ from those of the ideal gas, thus calling for complex models to accurately estimate their value As a consequence, fluid dynamic features are quite different from those of conventional steam or gas turbine. Moreover, the low speed of sound of complex organic fluids results in a supersonic flow regime.

In the last decade, much effort has been dedicated to advancing the simulation state-of-the-art and to the understanding of the steady state fluid dynamic operation of ORC turbomachinery. Two-dimensional flows of organic vapors were studied by means of Euler and Reynolds-averaged Navier–Stokes (RANS) simulations by Colonna *et al.*[2], Harinck *et al.*[3–5], Sciacovelli and Cinnella[6] and Wheeler and Ong[7], focusing on the peculiarities of dense vapour gasdynamics. Sauret and Gu[8] performed 3D simulations of a single stage radial inflow turbine in off-design conditions in order to assess its performance. Several works were devoted to the development of novel design methodologies for non-conventional machines. Guardone *et al.*[9] studied the effect of the fluid molecular complexity on nozzle design by means of the method of characteristics. Quasi-1D and throughflow calculations were used to demonstrate methods for optimal turbine design by Pini *et al.*[10] and Casati *et al.*[11]. Substantial improvement of a radial inlet turbine performance by means of automated stator-blade shape optimization was showcased by Harinck *et al.*[12] and Pasquale *et al.*[13].

However, the inherent unsteadiness of ORC turbines due to transonic and often supersonic flow regime (the expansion ratio can be of the order of 100 in small-capacity single-stage radial-inflow turbines) and to the continuous shift of operation between on- and off-design conditions requires unsteady, time resolved simulations to capture a number of phenomena otherwise ignored, e.g., shock/shock, shock wave/boundary layer and wake/boundary layer interaction, which can strongly affect the turbine performance.

The unsteady fluid dynamics of standard steam and gas turbines was extensively studied both experimentally and numerically in the last decades. Unsteady external disturbances and viscous wakes interact with the boundary layer affecting its transition to turbulence[14,15] and its heat load distribution and blade cooling effectiveness, which represent a major concern in standard applications, often leading to a deterioration of the latter[16–19]. Noise generation due to the fluctuating pressure field and vibrations induced by unsteady blade loads are also critical aspects in modern engines[20–22]. Finally, unsteady simulations and experiments are crucial for the improvement of multistage machines performance by vanes clocking, which can increase the efficiency up to 1% by simply adjusting the relative position of the stator vanes[23–26].

This paper presents a computational fluid dynamic (CFD) investigation of the stator/rotor interaction in a high-speed, single-stage, highly supersonic, radial inflow ORC turbine. The considered geometry is the preliminary design of the turbine studied by Harinck *et al.*[5]. Quasi-3D unsteady RANS simulations highlight the main flow characteristics under off-design conditions. The stator/rotor interaction is investigated in terms of shock interactions and blade loads in the time and frequency domain. CFD calculations were performed using an in-house flow solver which accounts for the non-ideal properties of the fluid via look-up tables generated using a multiparameter equation of state model. The analysis provides insights on the unsteady flow field and interaction mechanisms and demonstrates the importance of unsteady CFD simulations for the design of non-conventional turbomachines.

The paper is structured as follows. The CFD code and the fluid thermophysical models are described in Sec. 5.2. An overview of the turbine geometry and of the computational domain is given in Sec. 5.3. Results are presented in Sec. 5.4, which includes a

discussion of the instantaneous flow field (Sec. 5.4.1), of the unsteady shock waves and viscous wakes interaction (Sec. 5.4.2), of the rotor and stator blade pressure distributions (Sec. 5.4.3), of the time and modal analysis of rotor blade loads (Sec. 5.4.4) and of several virtual pressure probes placed inside the domain (Sec. 5.4.5), and of the isentropic efficiency of the machine (Sec. 5.4.6). Finally, conclusions are summarized in Sec. 6.4.

5.2 Numerical infrastructure and applied methods

5.2.1 RANS solver

The CFD code used in this study was developed by Pecnik *et al.*[27] and discretizes the compressible Navier–Stokes equations using a cell-centered finite-volume formulation. Convective fluxes are calculated using Liou's AUSM$^+$[28] approximate Riemann solver. Second order spatial accuracy is achieved by a least-squares gradient reconstruction of properties. Velocity and temperature gradients, needed for the evaluation of the viscous fluxes, are estimated on the cell faces as proposed by Kim *et al.*[29]. The one equation turbulence model of Spalart and Allmaras[30] closes the RANS equations and models the Reynolds stresses. The implicit formulation of the system of equations is generalized to a complex equation of state (EoS) model as described by Rinaldi *et al.*[31]. Equations are integrated in time by the second order accurate backward differentiation formula method and the resulting linear system is solved using the package PETSc[32]. The RANS solver was previously validated on turbomachinery flows of ideal and non-ideal fluids[33–36].

5.2.2 Thermophysical models of the working fluid

Due to the proximity of the inlet fluid thermodynamic state to its critical point, the ideal gas law is not suitable to represent the fluid properties. The equation of state model adopted in this study is based on the multiparameter Helmholtz energy function derived by Lemmon and Span[37], supplied with constitutive relations for transport properties detailed in Refs.[38–41]. Secondary thermodynamic properties, such as pressure and temperature derivatives, needed in the definition of the implicit numerical flux Jacobians by the RANS solver, are calculated using an in-house thermodynamic library[42].

The computational cost of property evaluation is drastically reduced by the use of look-up table interpolation, which replaces the direct evaluation of properties by means of the EoS model. This look-up table method is thoroughly analyzed in Ref.[31]. 400×400 discrete nodes were used to tabulate the single phase region of toluene spanning the range $\rho = [0.005, 145]\,\mathrm{kg/m^3}$ and $T = [310, 690]\,\mathrm{K}$. The nodes in the table are uniformly distributed along the T and $\log(\rho)$ range. The thermodynamic table is accessed in a straightforward manner using density and internal energy (to update the thermodynamic state in the cell centers at each time step), pressure and temperature (at the walls) and density and pressure (to reconstruct the thermodynamic state on the face centers). When neither density nor temperature are used as input variables for the interpolation function, a Newton–Raphson iterative procedure is used to inversely evaluate the corresponding ρ

and T. The iteration is stopped with a relative tolerance of 10^{-10} on the calculated ρ and T. The inverse evaluation of the input thermodynamic state is used for some specific boundary conditions only, namely the total inlet conditions which require the use of enthalpy and entropy to calculate the complete fluid state.

The average and maximum interpolation error over the whole tabulated region was calculated in a pre-processing step to ensure the desired level of accuracy in the fluid property estimation. Table 5.1 reports the results obtained by using 800,000 random thermodynamic input states. The error was calculated as $\varepsilon = |\phi_{\text{tab}} - \phi_{\text{EoS}}|/\phi_{\text{EoS}}$, where ϕ_{tab} and ϕ_{EoS} are the interpolated property and the one obtained by solving the equation of state model, respectively. Deviations are shown for enthalpy h, temperature T, speed of sound c, shear viscosity μ, thermal conductivity λ and isobaric specific heat c_P using two different combinations of input thermodynamic states, namely ρ, P and ρ, u. For each property, the maximum interpolation error does not exceed 0.05%, and the average error is below 0.0005%, thus confirming the accuracy of the approach.

Table 5.1: Thermophysical properties interpolation error

	h	T	c	μ	λ	c_P
$\varepsilon_{\max}(\rho, P)$	$3.25\,10^{-5}$	$9.07\,10^{-5}$	$1.17\,10^{-4}$	$2.88\,10^{-5}$	$3.25\,10^{-5}$	$2.26\,10^{-4}$
$\varepsilon_{\text{av}}(\rho, P)$	$3.27\,10^{-6}$	$4.49\,10^{-6}$	$2.38\,10^{-6}$	$2.01\,10^{-6}$	$3.64\,10^{-6}$	$1.55\,10^{-6}$
$\varepsilon_{\max}(\rho, u)$	$2.19\,10^{-6}$	$1.48\,10^{-5}$	$8.28\,10^{-5}$	$2.16\,10^{-5}$	$2.02\,10^{-5}$	$3.26\,10^{-4}$
$\varepsilon_{\text{av}}(\rho, u)$	$5.81\,10^{-8}$	$1.06\,10^{-6}$	$1.03\,10^{-6}$	$6.20\,10^{-7}$	$4.95\,10^{-7}$	$1.02\,10^{-6}$

5.3 Turbine geometry and computational domain

The geometry investigated in this work is taken from Harinck *et al.*[5] and can be considered as a preliminary design of the turbine operating in a commercial ORC power unit with a nominal power output in the range 60 – 170 kW_e. The turbine consists of a stator counting 18 blades, a rotor counting 47 blades and a diffuser, whereby the latter has not been taken into account in the present study. Figure 5.1 shows a photograph of the turbine geometry (left) and the computational domain and mesh (right). The working fluid is toluene and the inlet total conditions are in the range of pressures $P_{0,\text{r}} = [0.7, 0.8]$ and temperatures $T_{0,\text{r}} = [0.9, 1]$, where the subscript 0 denotes the total quantities and the reduced properties are indicated by the subscript r, i.e., normalized by their vapour-liquid critical value. The rotational speed of the machine is in the range $\omega = [24, 30]$ krpm.

In order to apply standard periodic boundary conditions along the circumferential direction and to reduce the size of the computational domain, the number of rotating blades was decreased to 45 in the numerical model. Thus, it was possible to model only 40° of the whole circumference, including 2 stator blades and 5 rotor blades, see Fig. 5.1. A quasi-3D computational mesh was employed: the 2D plane at half of the channel height

was discretized using one cell only in the vertical direction, but the real cross-sectional area distribution was kept as a function of the distance from the axis of rotation. This allows the fluid to expand in a similar manner as it would do in the real 3D geometry. The computational mesh was made of approximately 200,000 hexahedrons. The blades boundary layers were generated separately using an O-mesh and elements were clustered at the wall in order to have $y^+ \approx 1$. The rest of the domain was filled using a paving algorithm.

Constant radial inward velocity angle and total properties taken from Ref.[5] were set at the inlet, a Neumann boundary condition was applied at the supersonic rotor outlet. Two off-design rotational speeds were simulated, namely $\omega_1 = 24$ krpm and $\omega_2 = 28$ krpm. Blades were modeled as adiabatic walls. A flux-conserving treatment was used at the stator/rotor sliding interface[43]. Table 5.2 summarizes the boundary conditions used in this study.

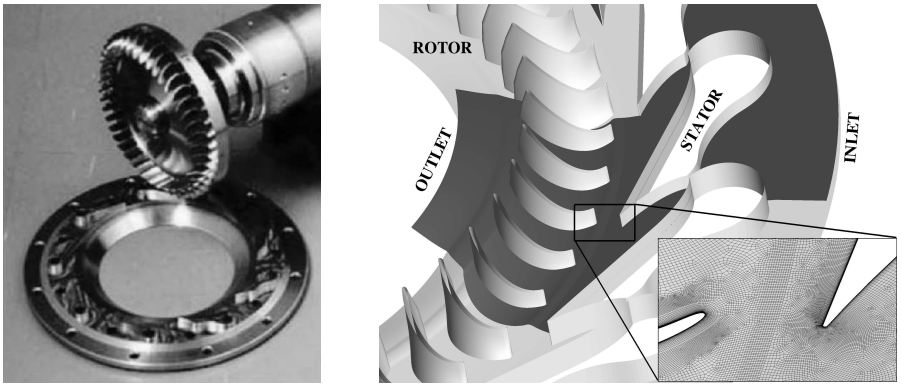

Figure 5.1: Turbine real geometry (left) and computational mesh (right)

5.4 Results

The results of the unsteady turbine simulation for two rotational speeds, namely 24 krpm and 28 krpm, are reported here. For both simulations a fixed time step was chosen such that every period was discretized in 100,000 steps, which corresponded to a maximum Courant number $CFL \approx 1.5$. Detailed results are discussed by meas of contour pots of pressure and entropy, time-averaged pressure distributions along the profiles, unsteady

Table 5.2: Turbine boundary conditions

$T_{0,in}$	$P_{0,in}$	P_{out}	ω	Walls
314.5 °C	31.9 bar	$\nabla P = 0$	24 krpm, 28 krpm	Adiabatic

blade loads, and modal analyses of the pressure field sampled at three locations of the computational domain and of the rotor blade loads.

The grid independence of the results was verified using a finer mesh counting 550,000 cells, which was obtained by applying a grid refinement strategy to the coarse grid (200,000 cells). All the cells belonging to the rotor domain were subdivided into 4 smaller control volumes. The same was done for the cells downstream of the stator blades trailing edge and for the ones crossed by the shock waves in the diverging part of the stator vanes. The average difference along the whole blade for the pressure profiles of the rotor blade at 28 krpm is summarized in table 5.3 and justifies the use of the coarse grid.

Table 5.3: Grid convergence results

	Min. PS	Max. PS	Av. PS	Min. SS	Max. SS	Av. SS
Av. difference [%]	1.17	1.27	0.59	3.58	2.86	1.20

5.4.1 Instantaneous flow field

In order to allow for an overall evaluation of the flow field, Fig. 5.2 displays the magnitude of the pressure gradient for 24 krpm and 28 krpm, which makes the visualization of the shock waves pattern distinct. Images depict the turbine field at $\tau = 0$, where $\tau = t/T$, with t being the physical time and T the time period needed by one rotor blade to move by 40 deg.

Similar flow features are observed for the operation at 24 krpm and 28 krpm. The fluid enters radially from the right hand side of the image, accelerates in the converging part of the stator vanes and reaches sonic conditions in the throat (TH). The expansion continues in the diverging part of the vane leading to highly supersonic flow with a Mach number $M \approx 2.8$. The fluid is then re-compressed by two oblique shock waves (ST1 and ST2) stemming from the rounded trailing edge of the stator blades. ST1 directly enters the rotor and interacts with the rotor blades and a complex pattern of shock waves in the rotor passages, while ST2 first hits the wall of the vane and then is reflected (R) in the rotor. The relative Mach number at the rotor inlet is supersonic in case of 24 krpm and causes the formation of strong bow shock waves (BS) in front of the blunt leading edge of the rotor blade. Weaker BS shocks are calculated at 28 krpm due to a lower (transonic) relative Mach number at the rotor inlet. For both rotational speeds, relative supersonic conditions are reached on the suction side of the rotor blades, which eventually result in oblique shock waves (OS) downstream of which the boundary layer separates forming large recirculation areas. The area variation in the rotor passages is such that the flow expands further to supersonic conditions near the blades trailing edge from which two oblique shock waves are generated (RT1 and RT2), similarly to ST1 and ST2 in the stator.

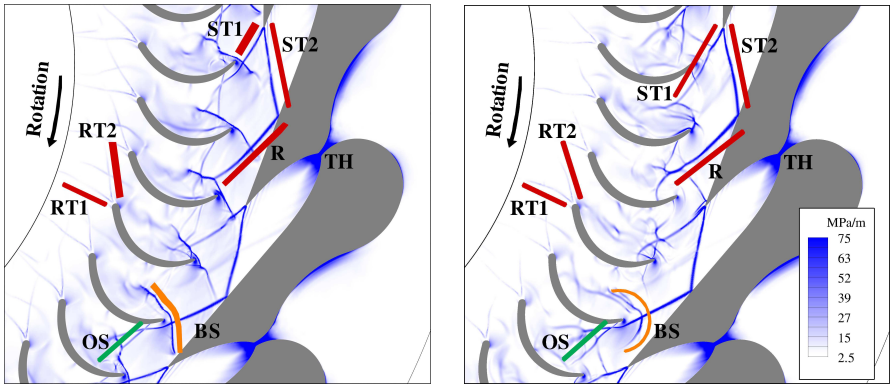

(a) ω = 24 krpm (b) ω = 28 krpm

Figure 5.2: Snapshot of the pressure gradient field at $\tau = 0$.

5.4.2 Unsteady shock wave and viscous wake interactions

Results are shown for one rotational speed only, namely 28 krpm, in order to avoid redundancy since the main features of the flow structure evolution at 24 krpm are qualitatively similar. Moreover, the machine operation at 28 krpm is more efficient, as shown in Sec. 5.4.6. Given the periodic nature of the flow field, the analysis is focused on the passage of one rotor blade, namely blade 4, through one stator vane, i.e., rotating by 20 deg, only.

Figure 5.3 shows the absolute value of the pressure gradient. At time $\tau = 0$, a bow shock wave (BS) is located in front of the leading edge of the blade due to local supersonic conditions in the relative frame of reference. The tail of the stator vane reflected shock (T1) is approached by the suction side of the rotor blade 0. A shock wave (P1) detaches from the front part of the rotor blade 3 pressure side, moving toward the middle of the channel. Subsequently, at $\tau = 1/12$ the P1 front extends along the length of rotor blade 3 and clusters with two other shock waves. Simultaneously, T1 impinges on the rotor blade 0 suction side and is reflected back toward BS, $\tau = 1/12$ and $\tau = 2/12$. The two interact at $\tau = 2/12$ merging in a single shock front at $\tau = 3/12$ which hits the stator blade wall at $\tau = 4/12$ and is reflected back (RBS) in the rotor at $\tau = 5/12$. This mechanism introduces a perturbation in the boundary layer of the stator blade, contributing to the unsteadiness in the pressure distribution highlighted in the following, see Fig. 5.5. At the same time, the reflected shock wave (T2) of the stator vane hits the pressure side of the rotor blade 3 and is convected downstream through the rotor blade channel, eventually impinging on the suction side of the rotor blade 4 at $\tau = 4/12$.

The main sources of losses are displayed by the normalized entropy field $s_n = (s - s_{in})/s_{in}$, as shown in Fig. 5.4. Entropy increase is visible in the stator blades boundary layer due to viscous dissipation. The boundary layer thickens at two locations (T1 and T2) due to the interaction with the stator trailing edge shock wave and the rotor blade

bow shock BS, see also Fig. 5.3. A large source of losses appears in the recirculation areas (S) on the suction side of the rotor blades and are caused by the boundary layer separation induced by the oblique shock waves located near the blades leading edge (OS, see Fig. 5.2(a) and Fig. 5.2(b)). Moreover, the entropy contour plot shows local peaks in the wakes of the stator. At $\tau = 0$, as the leading edge of the rotor blade 4 passes the stator blade trailing edge, a first peak (P1) is reached and convected downstream, impinging on the blade leading edge at $\tau = 3/12$. As the blade moves, the stator wake interacts with the pressure side at $\tau = 5/12$ and causes a local growth of the boundary layer. The interaction point and the wake itself are then convected downstream through the rotor blade channel (green arrow, starting from $\tau = 5/12$ and continuing from $\tau = 0$ to $\tau = 4/12$). The entropy increase induced by the shock waves are small if compared to the losses due to flow separation and viscous wakes.

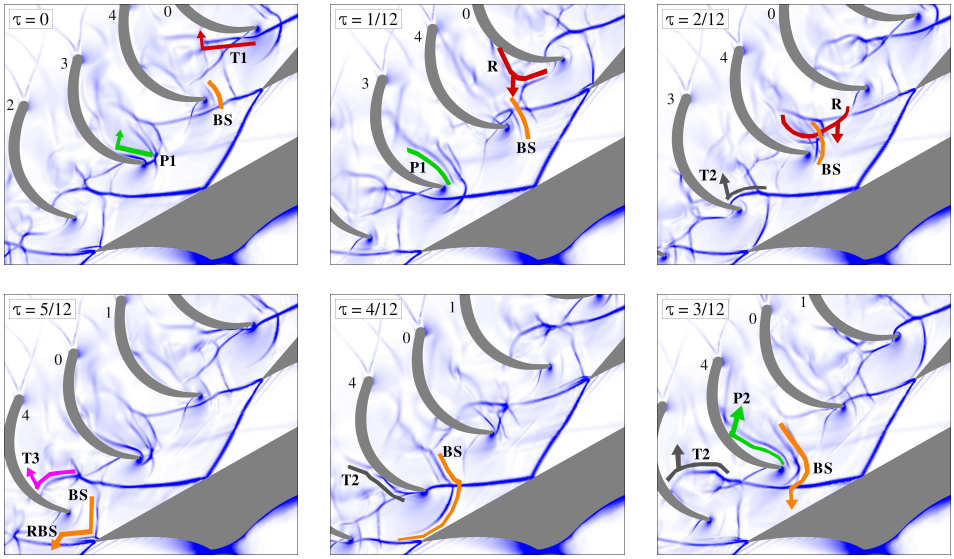

Figure 5.3: Time evolution of the pressure gradient field at 28 krpm over half time period. The color scale is the same as in Fig. 5.2(b).

5.4.3 Stator and rotor surface pressure distribution

Time-averaged pressure distributions on the rotor blade and on the diverging section of the stator nozzle are displayed in Fig. 5.5, together with the envelope of the maximum and minimum values over one time period. The collapse of the profiles for average, maximum and minimum values on the stator Side 1 indicates that the RANS result shows no unsteadiness. The same conclusion can be drawn for a large extent of Side 2. A strong shock wave (pressure is increased by a factor 3) compresses the fluid near the trailing edge of the blade and introduces a weak unsteadiness in the flow. This is partly

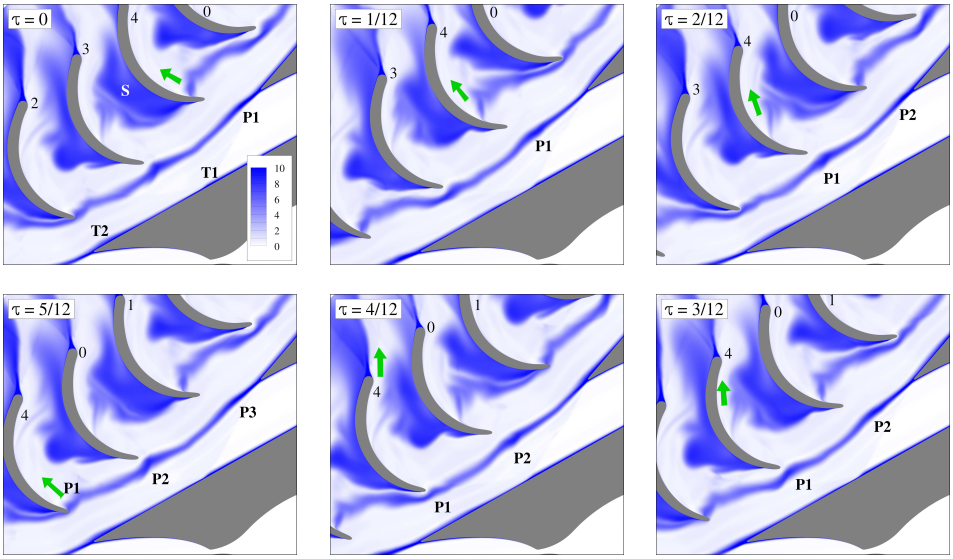

Figure 5.4: Time evolution of the normalized entropy field $s_n = (s - s_{in})/s_{in}$ at 28 krpm. The color scale goes from 0 (white) to 10 % (blue).

caused by the oscillation of the shock location on Side 2 over a range delimited by the maximum/minimum pressure lines of Fig. 5.5. The calculated pressure profiles do not present significant differences if the rotational speed is changed. Conversely, on the rotor blades the minimum/maximum pressure envelopes largely divert from the time-averaged profile. Maximum pressure deviations can be as large as 1 bar on the blade suction side at 28 krpm. This suggests that the flow in the rotor vanes is highly unsteady. Overall, positive pressure fluctuations can reach larger values on both pressure and suction sides and for both rotational speeds.

5.4.4 Modal analysis of rotor blade loads

The time evolution of the rotor blade loads is studied on a local coordinate system centered in the blade center of gravity and oriented in the radial and tangential directions with respect to the center of rotation of the rotor, as sketched in Fig. 5.7. The tangential and radial pressure forces, denoted as F_t and F_r, and the torque M_z are displayed for the rotor blade 4. Other blades profiles differ only by a shift of $\tau = 0.2$. The viscous contributions were found to be of the order of $\approx 1\%$, thus they are excluded from the analysis.

The force profiles show highly unsteady loads, featuring sharp variations due to the boundary layer interaction with shock waves. The force fluctuation can be as high as 60% of the time averaged value for the radial component and 30% for the tangential component. Torque also fluctuates largely and, notably, exhibits a change in sign for ω_2, which might be of concern in the structural design of the blade.

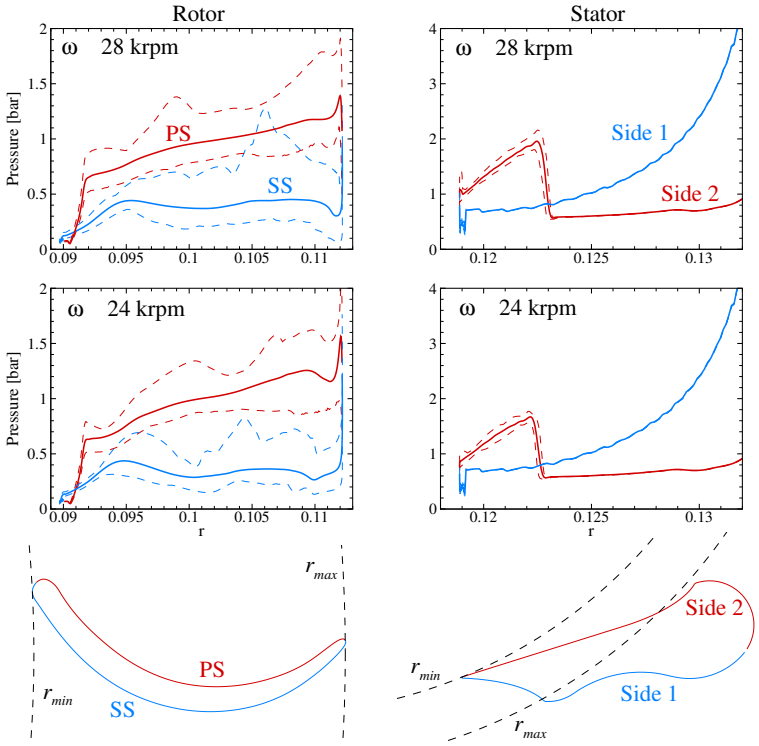

Figure 5.5: Time-averaged (solid lines), maximum and minimum values (dashed lines) of pressure on the rotor and stator blades. Quantities are functions of the radial distance $r = \sqrt{x^2 + y^2}$ from the axis of rotation.

Loads profiles can be related to the flow field evolution, described in Sec. 5.4.2. The sudden increase in the F_t magnitude at $\tau \approx 0.2 - 0.25$ is due to the pressure rise on the blade pressure side caused by the detachment of a shock wave, see P2 in Fig. 5.3. F_r increases as a consequence. This mechanism has an effect on M_z also, being responsible for the absolute minimum of the torque over the whole time period. At $\tau = 0.3 - 0.35$, the magnitude of F_t sharply decreases as a result of the impingement of the shock wave front T2 on the blade suction side, see Fig. 5.3. This affects the torque, determining a sudden decrease of M_z and eventually a chance in sign for the high rotational speed case.

A modal analysis of the blade loads highlights the different periodic contributions and gives indications on the extent of the frequency band which contains most of the energy. The calculated signal was sampled every 4.76×10^{-9} s over three periods, each amounting to 2.38×10^{-4} s. The blade loads frequency content is displayed in Fig. 5.8. Most of the energy is contained in the first 5-10 stator blade-passing-frequency (sBPF = 8,400 Hz) harmonics, and in particular in the first two. Similar profiles are obtained for 24 krpm and

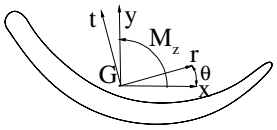

Figure 5.6: Local frame of reference for blade loads calculation

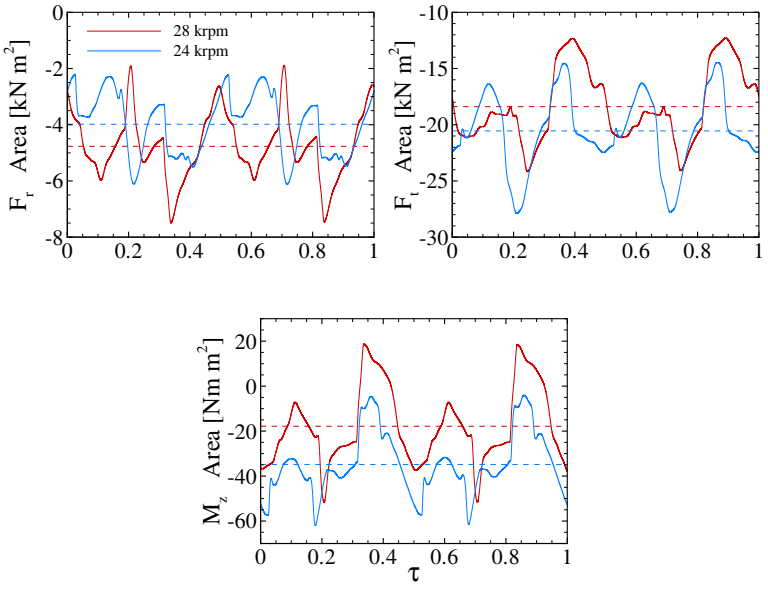

Figure 5.7: Time evolution of the blade forces and torque. Time-averaged values are also reported (dashed lines).

28 krpm.

5.4.5 Modal analysis of pressure probes

In this section, the pressure signal calculated at three locations of the computational domain is analyzed in the time and frequency domain. Figure 5.9 depicts the location of the three numerical probes; P1 is placed downstream of the stator blade trailing edge, and P2 and P3 are in front of the rotor blade leading edge and downstream of its trailing edge.

The physical signals and their spectra are displayed in Fig. 5.10. The sampling rate is the same used in the previous section. The pressure signal at P1 shows two dynamics locked by the rotor blade-passing-frequency (rBPF = 21,000 Hz); large oscillations which can be related to the oscillation of the impinging shock on the stator wall and to the interaction between the stator blade boundary layer and the rotor blades bow shocks,

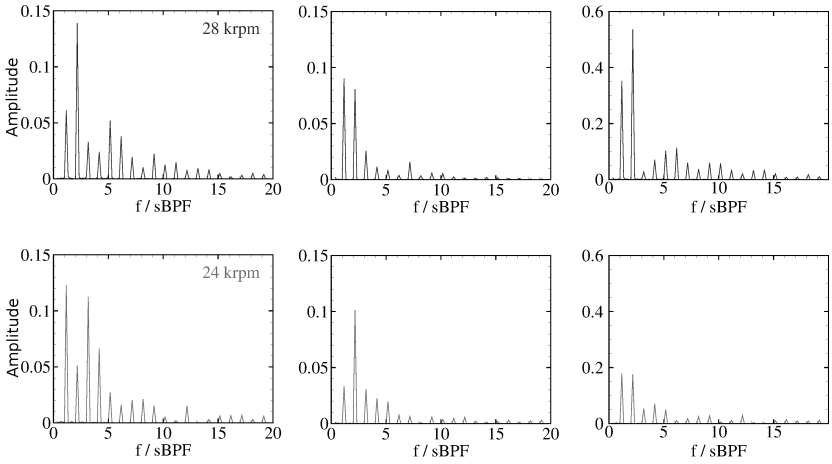

Figure 5.8: Spectra of the radial (left) and tangential (center) components of the force and torque (right) on the rotor blades. The frequency is normalized by the blade passing frequencies.

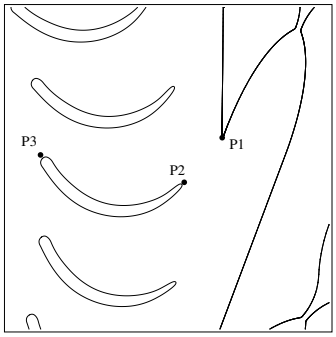

Figure 5.9: Numerical probes location

and smaller ones which are due to local peaks of vorticity which induce peaks of viscous losses, as described in Fig. 5.4. Both oscillations have larger amplitudes at high rotational speed, 28 krpm. The signal spectra separate the different periodic contributions; most of the energy is contained in the first harmonic for 24 krpm, while at 28 krpm the second and third harmonics also contribute significantly to the spectrum. P2 and P3 pressure profiles appear somewhat noisy, as confirmed by a larger number of harmonics which significantly contribute to the signals energy content. In case of P2, it is possible to identify the interaction between the rotor blade leading edge and the shock waves ST1 and ST2, see Fig. 5.2(a) and Fig. 5.2(b), by the sharp increase in pressure at $\tau \approx 0.05, 0.35, 0.55, 0.85$.

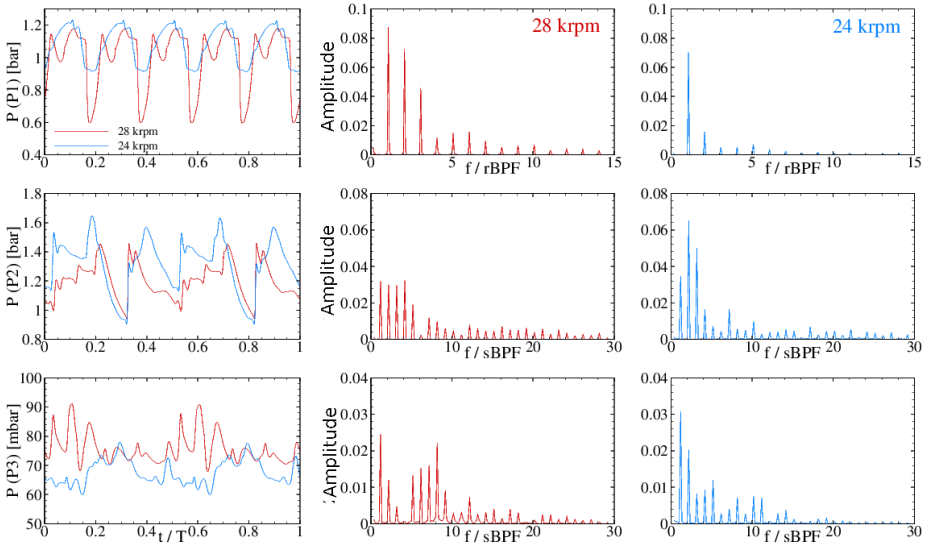

Figure 5.10: Pressure signal (left) and their spectra (center and right) calculated at the locations depicted in Fig. 5.9. The frequency is normalized by the blade passing frequencies.

5.4.6 Turbine efficiency

The calculated isentropic turbine efficiency $\eta = (h_{out} - h_{in})/(h_{out,s} - h_{in})$ is depicted in Fig. 5.11 for both rotational speeds. The time-averaged value at 28 krpm $\overline{\eta}_{\omega_2}$ was used as a reference. Based on this quantification it can be seen that for 28 krpm the efficiency is higher than for the low rotational speed. This can be partly explained by comparing Fig. 5.2(a) to Fig. 5.2(b) described in Sec. 5.4.1; a weaker shock waves structure in the rotor is calculated for 28 krpm, which leads to less losses and higher efficiency. For both rotational speeds, the efficiency profile oscillates periodically at a frequency which is twice the rotor blade-passing-frequency and five times the stator blade-passing-frequency. The amplitude of the oscillations is about 0.5 % in both cases.

5.5 Conclusions

The stator/rotor interaction in a high-speed, single-stage, highly supersonic, radial inflow ORC turbine was investigated by means of detailed quasi-3D unsteady RANS simulations in order to analyze the unsteadiness of the supersonic flow which is typical of this type of unconventional turbines. The considered geometry is the preliminary design of an operational ORC turbogenerator expander. A validated in-house CFD code was used to study the fluid dynamics of the expanding fluid, whose properties were approximated by

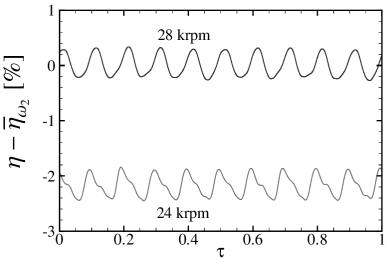

Figure 5.11: Isentropic efficiency

a multiparameter equation of state model.

The turbine performance and time evolution of the flow field were studied in terms of unsteady interactions between shock waves. Shocks generated at the trailing edge of the stator blades strongly interact with the rotor flow field and are responsible for total pressure losses and sharp fluctuations of the blade loads. Furthermore, it was possible to identify the main sources of losses, namely large recirculation areas on the suction side of the rotor blades and the viscous wake of the stator blades. Overall, higher turbine efficiency was calculated at high rotational speed.

The analysis of the rotor blade load profiles showed high unsteadiness which might be relevant as far as structural and fatigue aspect are of concern. Force fluctuations can reach up to 60% and 30% of their time-averaged value for the radial and tangential component, respectively, and are caused by the shock waves impingement on the blade surface. The torque was also found to feature ample and sharp fluctuations, and a change in sign in case of high turbine rotational speed. The steep changes in blade loads were related to the physical mechanisms of shocks interactions. A frequency domain analysis gave further information on the loads and flow field energy content, which was found to be limited to the first 5-10 harmonics for the blade loads and to a slightly larger range, 10-15 harmonics, in case of pressure signals sampled in the stator and rotor domain.

The documented analysis shows that intrinsically unsteady flow features and fluid dynamic mechanisms dominate the flow evolution in high-speed and supersonic ORC turbines. Unsteady CFD simulations are the only mean to numerically investigate those flow characteristics playing a primary role in the operation and performance of the turbine. Results allowed to identify the main loss sources and large blade loads fluctuations, whose minimization might be achieved using modern automated shape optimization techniques supplied by unsteady CFD data.

References

[1] Colonna, P., Casati, E., Trapp, C., Mathijssen, T., Larjola, J., Turunen-Saaresti, T., and Uusitalo, A., 2015. "Organic Rankine cycle power systems: From the concept to current technology, applications, and an outlook to the future". *J. Eng. Gas Turb. Power,* **137**(10), p. 100801.

[2] Colonna, P., Harinck, J., Rebay, S., and Guardone, A., 2008. "Real-gas effects in organic Rankine cycle turbine nozzles". *J. Propul. Power,* **24**(2), pp. 282–294.

[3] Harinck, J., Guardone, A., and Colonna, P., 2009. "The influence of molecular complexity on expanding flows of ideal and dense gases". *Phys. Fluids,* **21**(8), p. 086101.

[4] Harinck, J., Colonna, P., Guardone, A., and Rebay, S., 2010. "Influence of thermodynamic models in two-dimensional flow simulations of turboexpanders". *J. Turbomach.,* **132**(1), pp. 1–17.

[5] Harinck, J., Turunen-Saaresti, T., Colonna, P., Rebay, S., and van Buijtenen, J., 2010. "Computational study of a high-expansion ratio radial organic Rankine cycle turbine stator". *J. Eng. Gas Turb. Power,* **132**(5), p. 054501.

[6] Sciacovelli, L., and Cinnella, P., 2014. "Numerical study of multistage transcritical organic Rankine cycle axial turbines". *J. Eng. Gas Turb. Power,* **136**(8), p. 082604.

[7] Wheeler, A. P. S., and Ong, J., 2013. "The role of dense gas dynamics on organic Rankine cycle turbine performance". *J. Eng. Gas Turb. Power,* **135**(10), p. 102603.

[8] Sauret, E., and Gu, Y., 2014. "Three-dimensional off-design numerical analysis of an organic Rankine cycle radial-inflow turbine". *Appl. Energ.,* **135**, pp. 202–211.

[9] Guardone, A., Spinelli, A., and Dossena, V., 2013. "Influence of molecular complexity on nozzle design for an organic vapor wind tunnel". *J. Eng. Gas Turb. Power,* **135**(4), pp. 042307–6.

[10] Pini, M., Persico, G., Casati, E., and Dossena, V., 2013. "Preliminary design of a centrifugal turbine for organic Rankine cycle applications". *J. Eng. Gas Turb. Power,* **135**(4), p. 042312.

[11] Casati, E., Vitale, S., Pini, M., Persico, G., and Colonna, P., 2014. "Centrifugal turbines for mini-organic Rankine cycle power systems". *J. Eng. Gas Turb. Power,* **136**(12), p. 122607.

[12] Harinck, J., Pasquale, D., Pecnik, R., van Buijtenen, J., and Colonna, P., 2013. "Performance improvement of a radial organic Rankine cycle turbine by means of automated computational fluid dynamic design". *Proc. IMechE, Part A: J. Power and Energy,* **227**(6), pp. 637–645.

[13] Pasquale, D., Ghidoni, A., and Rebay, S., 2013. "Shape optimization of an organic Rankine cycle radial turbine nozzle". *J. Eng. Gas Turb. Power,* **135**(4), p. 042308.

[14] Schulte, V., and Hodson, H., 1998. "Unsteady wake-induced boundary layer transition in high lift LP turbines". *J. Turbomach.,* **120**(1), pp. 28–35.

[15] Wu, X., Jacobs, R., Hunt, J., and Durbin, P., 1999. "Simulation of boundary layer transition induced by periodically passing wakes". *J. Fluid Mech.,* **398**, pp. 109–153.

[16] Abhari, R., 1996. "Impact of rotor-stator interaction on turbine blade film cooling". *J. Turbomach.,* **118**(1), pp. 123–133.

[17] Shang, T., and Epstein, A., 1997. "Analysis of hot streak effects on turbine rotor heat load". *J. Turbomach.,* **119**(3), pp. 544–553.

[18] Teng, S., Sohn, D., and Han, J.-C., 2000. "Unsteady wake effect on film temperature and effectiveness distributions for a gas turbine blade". *J. Turbomach.,* **122**(2), pp. 340–347.

[19] Didier, F., Dnos, R., and Arts, T., 2002. "Unsteady rotor heat transfer in a transonic turbine stage". *J. Turbomach.,* **124**(4), pp. 614–622.

[20] Enghardt, L., Tapken, U., Neise, W., Kennepohl, F., and Heinig, K., 2001. "Turbine blade/vane interaction noise - Acoustic mode analysis using in-duct sensor rakes". In 7th AIAA/CEAS Aeroacoustics Conference and Exhibit, no. AIAA-2001-2153, AIAA, pp. 1–8.

[21] Mailach, R., Mller, L., and Vogeler, K., 2004. "Rotor-stator interactions in a four-stage low-speed axial compressor - Part II: Unsteady aerodynamic forces of rotor and stator blades". *J. Turbomach.,* **126**(4), pp. 519–526.

[22] Hushmandi, N., Fridh, J., and Fransson, T., 2011. "Unsteady forces of rotor blades in full and partial admission turbines". *J. Turbomach.,* **133**(4).

[23] Huber, F., Johnson, P., Sharma, O., Staubach, J., and Gaddis, S., 1996. "Performance improvement through indexing of turbine airfoils: Part 1 - Experimental investigation". *J. Turbomach.,* **118**(4), pp. 630–635.

[24] Griffin, L., Huber, F., and Sharma, O., 1996. "Performance improvement through indexing of turbine airfoils: Part 2 - Numerical simulation". *J. Turbomach.,* **118**(4), pp. 636–642.

[25] Arnone, A., Marconcini, M., Pacciani, R., Schipani, C., and Spano, E., 2002. "Numerical investigation of airfoil clocking in a three-stage low-pressure turbine". *J. Turbomach.,* **124**(1), pp. 61–68.

[26] Schennach, O., Pecnik, R., Paradiso, B., Göttlich, E., Marn, A., and Woisetschläger, J., 2008. "The effect of vane clocking on the unsteady flow field in a one-and-a-half stage transonic turbine". *J. Turbomach.,* **130**(3), p. 031022.

[27] Pecnik, R., Terrapon, V. E., Ham, F., Iaccarino, G., and Pitsch, H., 2012. "Reynolds-averaged Navier-Stokes simulations of the HyShot II scramjet". *AIAA J.,* **50**(8), pp. 1717–1732.

[28] Liou, M.-S., 1996. "A sequel to AUSM: AUSM$^+$". *J. Comput. Phys.,* **129**(2), pp. 364–382.

[29] Kim, S.-E., Makarov, B., and Caraeni, D., 2003. "A multi-dimensional linear reconstruction scheme for arbitrary unstructured grids". *AIAA paper,* **No. 2003-3990**, p. 2003.

[30] Spalart, P. R., and Allmaras, S. R., 1994. "One-equation turbulence model for aerodynamic flows". *Rech. Aerospatiale*(1), pp. 5–21.

[31] Rinaldi, E., Pecnik, R., and Colonna, P., 2014. "Exact Jacobians for implicit Navier–Stokes simulations of equilibrium real gas flows". *J. Comput. Phys.,* **270**, pp. 459–477.

[32] Satish, B., Buschelman, K., Eijkhout, V., Gropp, W. D., Kaushik, D., Knepley, M. G., Mc Innes, L. C., Smith, B. F., and Zhang, H., 2009. "PETSc Web page, http://www.mcs.anl.gov/petsc".

[33] Pecnik, R., Witteveen, J. A. S., and Iaccarino, G., 2013. "Assessment of uncertainities in modeling of laminar to turbulent transition for transonic flows". *Flow Turbulence Combust.,* **91**, pp. 41–61.

[34] Rinaldi, E., Suarez Raspopov, R., Colonna, P., and Pecnik, R., 2014. "Modeling curvature effects on turbulence transition for turbomachinery flows". In Proceedings of the ASME Turbo Expo, pp. 1–11.

[35] Pecnik, R., Rinaldi, E., and Colonna, P., 2012. "Computational fluid dynamics of a radial compressor operating with supercritical CO_2". *J. Eng. Gas Turb. Power,* **134**(12), p. 122301.

[36] Rinaldi, E., Pecnik, R., and Colonna, P., 2015. "Computational fluid dynamic simulation of a supercritical CO_2 compressor performance map". *J. Eng. Gas Turb. Power,* **137**(7), July, p. 072602.

[37] Lemmon, E. W., and Span, R., 2006. "Short fundamental equations of state for 20 industrial fluids". *J. Chem. Eng. Data,* **51**(3), pp. 785–850.

[38] Olchowy, G. A., and Sengers, J. V., 1989. "A simplified representation for the thermal conductivity of fluids in the critical region". *Int. J. Thermophys.,* **10**(2), pp. 417–426.

[39] Polt, A., Platzer, B., and Maurer, G., 1992. "Parameter der thermischen Zustandsgleichung von Bender fuer 14 mehratomige reine Stoffe". *Chem. Tech.(Leipzig),* **44**(6), pp. 216–224.

[40] Santos, F. J. V., Nieto De Castro, C. A., Dymond, J. H., Dalaouti, N. K., Assael, M. J., and Nagashima, A., 2006. "Standard reference data for the viscosity of toluene". *J. Phys. Chem. Ref. Data,* **35**(1), pp. 1–8.

[41] Assael, M. J., Mylona, S. K., Huber, M. L., and Perkins, R. A., 2012. "Reference correlation of the thermal conductivity of toluene from the triple point to 1000 K and up to 1000 MPa". *J. Phys. Chem. Ref. Data,* **41**(2), p. 023101.

[42] Colonna, P., van der Stelt, T. P., and Guardone, A., 2012. FluidProp (Version 3.0): A program for the estimation of thermophysical properties of fluids. http://www.fluidprop.com/. A program since 2004.

[43] Rinaldi, E., Colonna, P., and Pecnik, R., 2015. "Flux-conserving treatment of non-conformal interfaces for finite-volume discretization of conservation laws". *Comp. Fluids,* **120**, pp. 126–139.

6

Linear stability analysis of a channel flow with temperature dependent transport properties

Part of the contents of this chapter appeared in:

Rinaldi, E., Boersma, B.J., & Pecnik, R., 2015. *15th European Turbulence Conference*.

Abstract *This Chapter investigates the role of temperature dependent thermal conductivity and specific heat on the maximum energy growth of perturbations in a thermally-stratified laminar channel flow under symmetric and asymmetric reference temperature profiles. All the computations are performed assuming a constant destabilizing viscosity distribution. A parametric study is conducted to assess the effect of the Prandtl number and different property gradients across the channel. Variable properties result in a substantial modulation of the maximum energy growth and of the growth rate, therefore further stabilizing or destabilizing the flow compared to the constant property case. The results indicate that either enhancement or reduction of maximum energy growth can occur if only one property changes across the channel. Namely, enhancement of the maximum growth is obtained with cross stream decreasing thermal conductivity and increasing specific heat profiles with respect to the reference values, while the opposite effect is observed for the reversed property distribution. In case both thermal conductivity and specific heat are functions of temperature, the maximum energy growth is always amplified, irrespectively of their profiles. The maximum modulation induced by variable transport properties is found for a spanwise perturbation under a linear reference temperature profile.*

6.1 Introduction

The hydrodynamic stability of shear flows is commonly studied by means of an eigenvalue analysis of the linearized governing equations. This approach is called *modal stability* analysis and provides information on whether small perturbations to a laminar reference state are damped (stable flow) or grow exponentially in time (unstable flow)[(1)]. The first accurate calculation of the critical Reynolds number in a plane channel flow above which transition may occur dates back to 1971 and is due to Orszag, who reported $Re_{cr} \approx 5772$[(2)]. However, experimental evidence shows that transition usually occurs at lower sub-critical Reynolds numbers, $Re \approx 1000$.

The discrepancy between experiments and the prediction of the linearized theory lies in considering the asymptotic behaviour of the flow only by looking at the sign of the eigenvalues. Transient energy growth is a key mechanism for shear flows to undergo early transition and is caused by the non-normality of the linearized Navier–Stokes operator, whose eigenfunctions are by definition non-orthogonal. Small perturbations may be amplified by several orders of magnitude, and conditions may be met for other instabilities and flow non-linearities to be triggered.

In order to overcome this limitation, *non-modal stability* studies the transient behaviour of perturbations providing important insights on the physical mechanisms at the first stages of the laminar-turbulent transition[(3–5)]. In the early 90's, the pioneering studies of Reedy and Henningson[(6)] and Reddy *et al.*[(7)] showed that substantial energy growth, of order $O(1000)$, can be achieved in a channel flow with constant properties at subcritical Reynolds numbers. They also found that the highest energy amplification is obtained for streamwise independent perturbations. Several authors extended the analysis to assess whether viscosity stratification has a stabilizing or destabilizing effect. The modal stability analysis conducted by Wall and Wilson showed that an increase in viscosity

always stabilizes the flow, while a non-uniform decrease of viscosity may either destabilize, as expected, or stabilize the flow, in case a thin layer of low viscosity is formed at the heated wall[8]. The effect of a non-uniform viscosity distribution across the channel on the transient energy growth of thermally stratified flows was investigated by Chikkadi *et al.*[9], who found it to only marginally modify the temporal evolution of the perturbation energy. Their results were confirmed in a systematic investigation by Sameen and Govindarajan[10,11], who additionally considered the effect of Prandtl number Pr on the modal and non-modal stability characteristics of a heated channel flow, reporting a strong influence of Pr on the maximum energy growth. A recent review of instabilities in viscosity stratified flows is provided by Govindarajan and Sahu[12].

In this Chapter we discuss the influence of temperature dependent thermal conductivity λ and isobaric specific heat c_p on the non-modal stability of a thermally-stratified channel flow. The focus of the presented analysis is on the modulation of the maximum energy growth and of the growth rate in order to assess whether temperature dependent transport properties contribute to the stabilization or destabilization of a channel flow. Results are shown for a constant destabilizing viscosity profile and over a range of Prandtl numbers which encompasses most fluids of practical interest. The investigation of the effects of λ and c_p variation across the channel height is performed in two steps: firstly, the properties are decoupled and only one at a time is considered temperature dependent; secondly, a non-uniform distribution is imposed on both λ and c_p.

This Chapter is organized as follows. The governing equations, property profiles and numerical discretization are described in Sec. 6.2. Results are presented and discussed in Sec. 6.3. Finally, conclusions are drawn in Sec.6.4.

6.2 Governing equations

The channel flow geometry considered in this study is depicted in Fig. 6.1. The streamwise, wall-normal, and spanwise directions are indicated by x, y, and z, respectively, and the components of the velocity vector along the three directions are denoted by u, v and w. The reference temperature profiles investigated in this Chapter are also reported in the Figure: they are a linear (T1) and parabolic profile (T2), which represent an asymmetric and a symmetric heating of the flow.

In order to linearize the Navier–Stokes equations, the non-dimensional velocity vector and non-dimensional temperature are decomposed into a reference state and a perturbation

$$\mathbf{u}(x,y,z,t) = \left[U(y) + u(x,y,z,t),\ v(x,y,z,t),\ w(x,y,z,t)\right], \tag{6.1}$$

$$\Theta(x,y,z,t) = T(y) + \theta(x,y,z,t). \tag{6.2}$$

The perturbations are expressed in normal Fourier mode form as

$$v(x,y,z,t) = \tilde{v}(y)\, \mathrm{e}^{\mathrm{i}(\alpha x+\beta z-\omega t)}, \tag{6.3}$$

$$\theta(x,y,z,t) = \tilde{\theta}(y)\, \mathrm{e}^{\mathrm{i}(\alpha x+\beta z-\omega t)}, \tag{6.4}$$

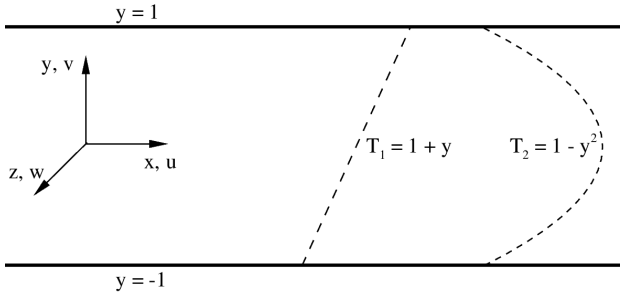

Figure 6.1: Channel flow geometry and non-dimensional temperature profiles.

where α and β denote the streamwise and spanwise wave numbers, respectively, and $\omega = c\alpha$ is the complex frequency.

The reference velocity profile, $U(y)$, cannot be determined a priori. It is calculated numerically by solving the non-dimensional momentum equation in the y direction

$$\frac{d}{dy}\left(\mu\frac{dU}{dy}\right) = -2, \tag{6.5}$$

which for a constant viscosity profile gives $U = 1 - y^2$. Equation (6.5) is solved using a spectral collocation method based on Chebyshev polynomials. In order to avoid interpolations of the reference velocity profile and of its derivatives, the same collocation nodes are used for Eq. (6.5) and for the discretization of the linear stability equations introduced below.

Viscosity, thermal conductivity, and isobaric specific heat are expressed as functions of the non-dimensional temperature only as

$$\mu_d = \overline{\mu}\,\mathrm{e}^{-K_\mu\Theta}, \qquad \lambda_d = \overline{\lambda}\,\mathrm{e}^{-K_\lambda\Theta}, \qquad c_{p_d} = \overline{c_p}\,\mathrm{e}^{-K_{c_p}\Theta}, \tag{6.6}$$

where the subscript d denotes the dimensional quantities, K indicates the rate of variation, and $\overline{\mu}$, $\overline{\lambda}$, and $\overline{c_p}$ are the reference values used to non-dimensionalize the equations and to define the Reynolds number $Re = \overline{U}\,\overline{L}\,\overline{\rho}/\overline{\mu}$, the Prandtl number $Pr = \overline{\mu}\,\overline{c_p}/\overline{\lambda}$, and the Richardson number $Ri = g\beta\Delta T\overline{L}^3\overline{\rho}^2/\overline{\mu}^2Re^2$. In the previous definitions $\overline{L}$ is the reference length scale, $\overline{\rho}$ is the reference density, g the acceleration due to gravity, β the volumetric thermal expansion coefficient of the fluid, and $\Delta T = T_s - T_b$ is the difference between the surface and bulk temperatures.

The derivatives of the transport properties with respect to the spatial coordinates are expressed using the chain rule, e.g.,

$$\frac{\partial\mu\left(\Theta(x,y,z,t)\right)}{\partial x} = \frac{d\mu(\Theta)}{d\Theta}\frac{\partial\Theta(x,y,z,t)}{\partial x}. \tag{6.7}$$

The Navier–Stokes equations are conveniently recasted in the $v-\eta$ formulation in order to remove the pressure term from the equations and to automatically satisfy the continuity constraint. The linearization procedure and the transformation to the Fourier space

using Eqs (6.3)-(6.4) lead to the following linear stability equations in non-dimensional form

$$\begin{aligned}
\mathrm{i}\alpha[(v''-k^2v)(U-c)-U''v] = \frac{1}{Re}\Bigg\{&\mu[v''''-2k^2v''+k^4v] \\
&+\frac{d\mu}{dT}T'2[v'''-k^2v']+\frac{d\mu}{dT}T''[v''+k^2v]+\frac{d^2\mu}{dT^2}(T')^2[v''+k^2v] \\
&-\frac{d\mu}{dT}\mathrm{i}\alpha[U'\theta''+2U''\theta'+(k^2U'+U''')\theta]-2\mathrm{i}\alpha\frac{d^2\mu}{dT^2}U'T'\theta' \\
&-\mathrm{i}\alpha\frac{d^2\mu}{dT^2}T''U'\theta-2\mathrm{i}\alpha\frac{d^2\mu}{dT^2}U''T'\theta-\mathrm{i}\alpha\frac{d^3\mu}{dT^3}U'(T')^2\theta\Bigg\}-Ri\,k^2\theta, \quad (6.8)
\end{aligned}$$

$$\begin{aligned}
\mathrm{i}\alpha(U-c)\eta+\mathrm{i}\beta U'v = \frac{1}{Re}\Bigg\{&\mu[\eta''-k^2\eta]+\frac{d\mu}{dT}T'\eta' \\
&+\mathrm{i}\beta\frac{d\mu}{dT}[U''\theta+U'\theta']+\mathrm{i}\beta\frac{d^2\mu}{dT^2}T'U'\theta\Bigg\}, \quad (6.9)
\end{aligned}$$

$$\mathrm{i}\alpha(U-c)\theta+T'v = \frac{1}{RePr}\frac{\lambda}{c_p}\left(\theta''-k^2\theta\right)+\frac{1}{RePr}\frac{2}{c_p}\frac{d\lambda}{dT}T'\theta', \quad (6.10)$$

which represent the Orr–Sommerfeld, Squire, and energy equations, respectively, for a fluid with temperature dependent transport properties. In Eqs. (6.8)-(6.10), the Boussinesq approximation was used to model the buoyancy term. The tilde symbol was dropped for simplicity and the prime $'$ denotes the derivative with respect to y. η is the component of the vorticity in the wall normal direction, and $k^2=\alpha^2+\beta^2$. The transport properties are non-dimensionalized as $\mu=\mu_d/\overline{\mu}$, $\lambda=\lambda_d/\overline{\lambda}$, and $c_p=c_{p_d}/\overline{c_p}$. The following boundary conditions are applied to the perturbations

$$v(\pm1)=v'(\pm1)=\eta(\pm1)=\theta(\pm1)=0. \quad (6.11)$$

Equations (6.8)-(6.10) are discretized numerically using collocated Chebyshev polynomials[13], and the spectrum of the linear operator is calculated using the software MATLAB. The validation of the numerical code used in this study is presented in the Appendix A.1.

In order to study the non-modal stability of the flow, a definition is needed to measure the energy of the perturbations. A common choice is the positive definite norm in the form[6,10,14]

$$\|\,\mathbf{v}\,\|_E^2=\frac{1}{2}\int_{-1}^{1}\left\|\frac{\partial v}{\partial y}\right\|^2+k^2\|v\|^2+\|\eta\|^2+\|\theta\|^2dy, \quad (6.12)$$

which is proportional to the energy of the perturbation vector $\mathbf{v}=[v,\eta,\theta]$. From this definition, a weight matrix can be defined, $Q=C^*C$, with C denoting the Cholesky decomposition matrix. The disturbance energy growth function is then expressed as

$$G(t)\equiv\max_{\mathbf{v}(0)\neq0}\frac{\|\,\mathbf{v}(t)\,\|_E^2}{\|\,\mathbf{v}(0)\,\|_E^2}=\frac{\left\|\,\mathrm{e}^{-\mathrm{i}\Lambda t}\mathbf{v}(0)\,\right\|_E^2}{\|\,\mathbf{v}(0)\,\|_E^2}=\left\|\,CT\mathrm{e}^{-\mathrm{i}\Lambda t}T^{-1}C^{-1}\,\right\|_2^2, \quad (6.13)$$

where $\mathcal{L} = T\Lambda T^{-1}$ is the singular value decomposition of the linear operator describing Eqs. (6.8)-(6.10) and the subscript E indicates the energy norm. Hereafter, the maximum energy growth over time will be denoted as $G_{max} = \max_{t>0} G(t)$ in case of variable properties and $G_{max,0}$ for a constant property case, i.e., $K_\lambda = K_{c_p} = 0$ (viscosity is always considered variable across the channel height). Accordingly, the time at which the maximum growth is reached will be referred to as $t_{G_{max}}$ and $t_{G_{max,0}}$.

6.3 Energy growth modulation

The effect of temperature dependent c_p and λ on the maximum energy growth is investigated for a fixed combination of flow parameters used for all the calculations presented in the following, namely $Re = 1000$, $Ri = 0$, and $K_\mu = 0.2$, the latter having a destabilizing effect on the flow with respect to a uniform viscosity case, as reported by Wall and Wilson[8].

Three perturbations with a fixed amplitude, $k = 0.5$, are considered in the following, namely a streamwise (ST), a spanwise (SP), and an oblique (OB) perturbation. The choice of the amplitude is justified by the results shown in Fig. 6.2, which displays $\log_{10}(G_{max,0})$ on the wave number space for the reported combination of flow parameters at three different Prandtl numbers, namely $Pr = 10^{-2}$, 1, 10. At low Pr, the distribution of the maximum growth function is similar to the constant viscosity case, and has its absolute maximum for the spanwise perturbation $\alpha = 0, \beta \approx 2$. The maximum growth for a streamwise perturbation is obtained for $\alpha \approx 0.4, \beta = 0$. As Prandtl increases, larger maximum amplifications are reached, the region of maximum growth for spanwise perturbations elongates on the vertical axis and its absolute maximum moves toward lower values of β. Overall, the choice $k = 0.5$ represents a compromise to reach high perturbation amplifications in each of the three directions, ST, SP, and OB, and over a wide range of Pr.

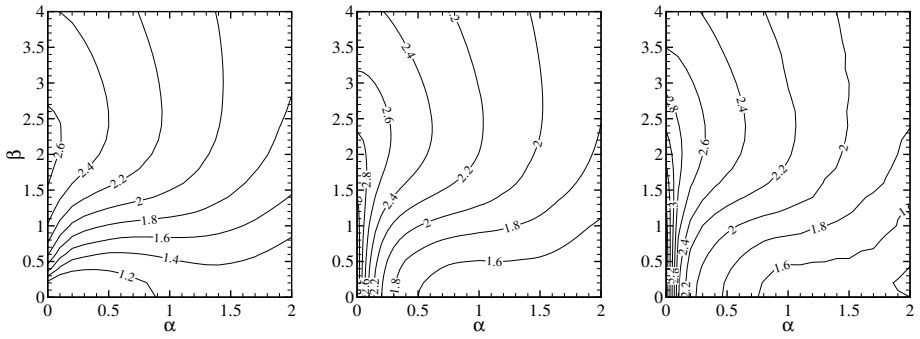

(a) $Pr = 10^{-2}$ (b) $Pr = 1$ (c) $Pr = 10$

Figure 6.2: Contour lines of $\log_{10}(G_{max,0})$ for $Re = 1000$, $Ri = 0$, and $K_\mu = 0.2$.

The individual effect of variable c_p and λ is investigated first, i.e., only one property at a time is considered as temperature dependent imposing $K_\lambda = 0$ for the variable c_p case, and vice versa. Figure 6.3 displays the ratio $G_{max}/G_{max,0}$ for a linear reference temperature profile. For each of the perturbations, maximum energy growth amplification is observed for positive values of K_λ and negative values of K_{c_p}, which correspond to a decreasing thermal conductivity $\lambda < 1$ and increasing specific heat $c_p > 1$ across the channel height, respectively. Conversely, maximum energy growth is reduced for opposite property profiles. The effect of c_p and λ is almost specular: similar amplification/reduction is in fact obtained for any considered pair of K_λ and $-K_{c_p}$. This behaviour is due to the fact that λ appears in the numerator while c_p in the denominator in Eq. (6.10). However, the presence of the derivative of the thermal conductivity in the last term on the right-hand-side of Eq. (6.10) introduces a difference in the effect of c_p and λ, visible for increasing magnitude of the exponents K_{λ,c_p}. The trends obtained under ST and OB perturbations are similar: the maximum effect is at low Prandtl numbers and amounts to up to $\pm 20\%$, it gradually decreases for increasing Pr and shows a second peak of smaller amplitude at $Pr \approx 1$ before eventually decaying. A qualitatively different behaviour is observed under a SP perturbation: the energy modulation is negligible in the limits of small and very large Pr, and shows one maximum/minimum which reaches up to $\approx \pm 30\%$ at a constant optimal Pr. Overall, the effect of variable c_p and λ is larger if compared to the ST and OB cases, and extends over a wider range of Prandtl numbers.

Results concerning a symmetric parabolic temperature profile are reported in Fig. 6.4 for the same combinations of perturbation intensities and property parameters K_{λ,c_p}. The modulation of the maximum energy growth resulting from variable properties is smaller than for a linear reference temperature profile. Maximum amplification/reduction is limited to up to $\approx \pm 10\%$ for the ST and OB perturbation cases, and to up to $\approx \pm 20\%$ for the SP case. The trends obtained under ST and OB perturbations appear to be qualitatively different from the ones obtained with a linear temperature profile: the effect of variable properties is distributed over a wider range of Pr and it appears to be almost independent from this parameter in the decade $Pr = [0.03, 0.3]$. The similarity observed between the effects of K_λ and $-K_{c_p}$ for the linear temperature profile is not found in case of a parabolic temperature profile. The variable λ curves shift toward higher Prandtl numbers, and thermal conductivity has an overall smaller effect if compared to specific heat. The latter observation is true in case of SP perturbation also.

Another useful measure of the flow stabilization or destabilization due to variable properties is the time needed to reach the maximum amplification of a perturbation. Figure 6.5 displays the ratio $t_{G_{max}}/t_{G_{max,0}}$ for a SP perturbation, which was shown to be the most effective to enhance/suppress the maximum energy growth, under both a linear and parabolic temperature profiles. Similar trends are observed in both cases: for $\lambda < 1$ and $c_p > 1$ profiles the maximum disturbance amplification takes shorter at low Prandtl numbers, if compared to the constant property case, and longer for medium/high Prandtl numbers. The opposite behaviour is observed for reversed λ and c_p profiles. Larger modulation of $t_{G_{max}}$ is obtained by variable properties under a linear temperature profile, up to $\approx \pm 20\%$, if compared to the parabolic temperature profile case, whereby the maximum effect is $\approx \pm 10\%$ and is shifted to higher Pr.

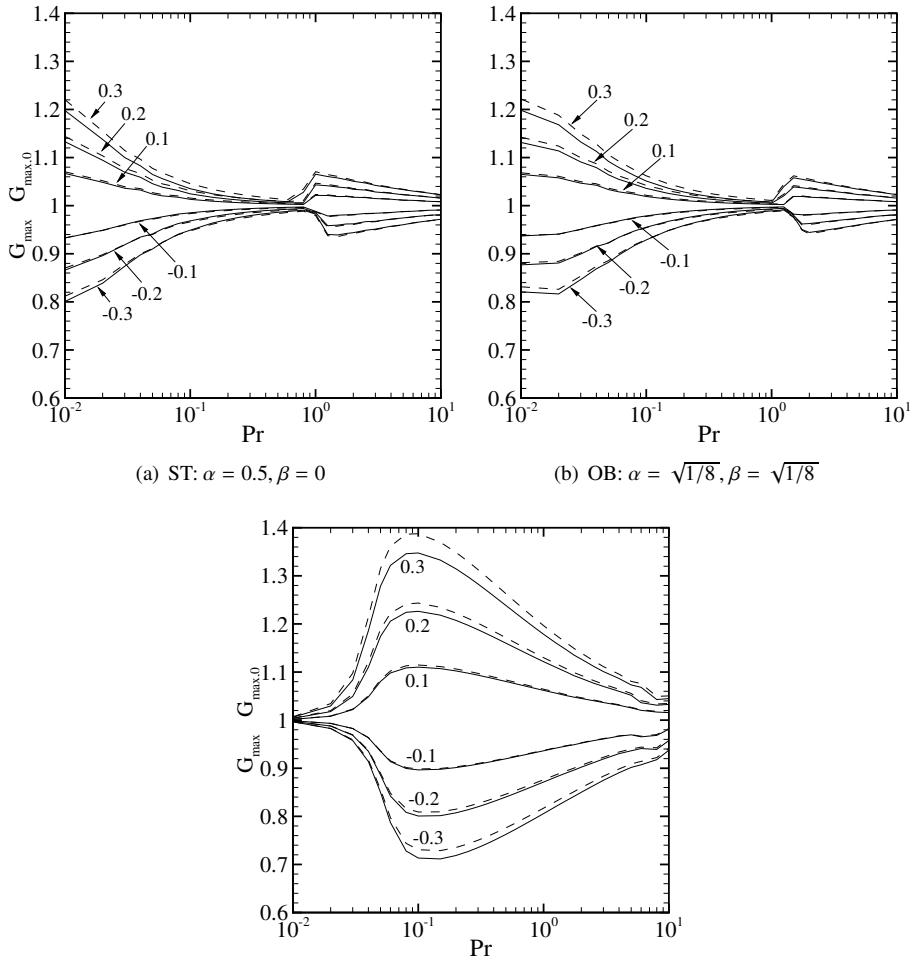

(a) ST: $\alpha = 0.5, \beta = 0$

(b) OB: $\alpha = \sqrt{1/8}, \beta = \sqrt{1/8}$

(c) SP: $\alpha = 0, \beta = 0.5$

Figure 6.3: G_{max} modulation for a linear temperature profile, $T = 1 + y$. Numbers denote values of K_λ (solid lines) and $-K_{c_p}$ (dashed lines).

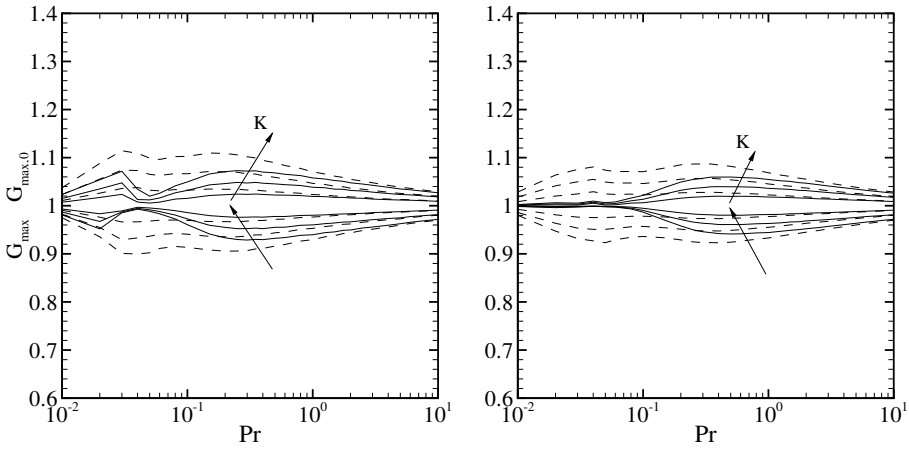

(a) ST: $\alpha = 0.5, \beta = 0$

(b) OB: $\alpha = \sqrt{1/8}, \beta = \sqrt{1/8}$

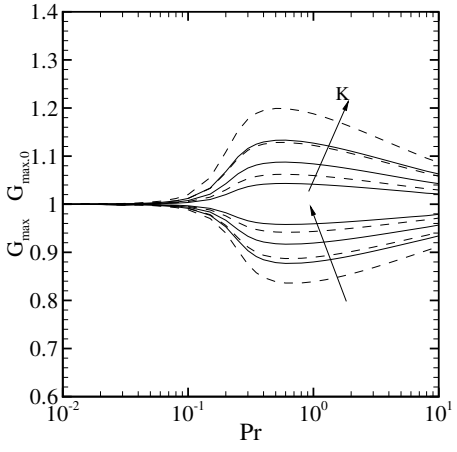

(c) SP: $\alpha = 0, \beta = 0.5$

Figure 6.4: G_{max} modulation for a parabolic temperature profile, $T = 1 - y^2$. Arrows indicate the direction of increasing K_λ (solid lines) and $-K_{c_p}$ (dashed lines).

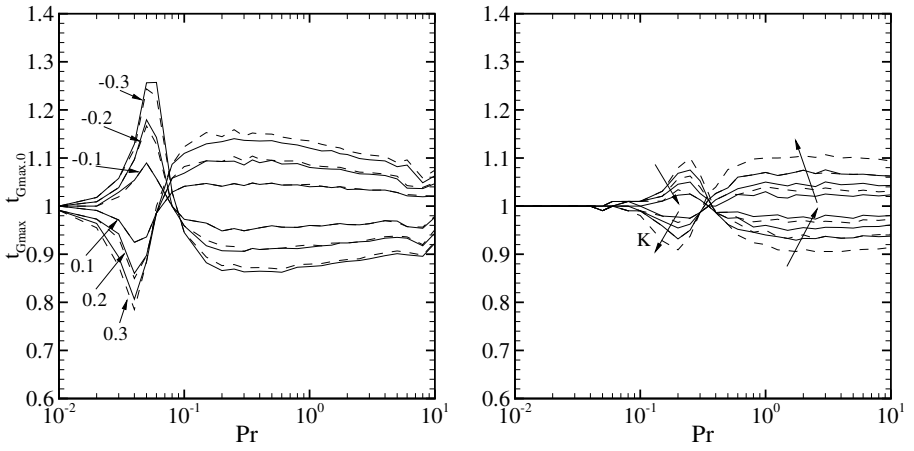

(a) $T = 1 + y$ (b) $T = 1 - y^2$

Figure 6.5: $t_{G_{max}}$ modulation under a spanwise perturbation. Numbers denote values of K_λ (solid lines) and $-K_{c_p}$ (dashed lines).

The coupled effect of variable thermal conductivity and specific heat is assessed in Fig. 6.6 under the assumption of unit local Prandtl number based on non-dimensional properties, i.e., $\mu(T)\, c_p(T)/\lambda(T) = 1$. This condition can be rewritten as $K_\lambda = K_{c_p} + K_\mu$ using Eq. (6.6). Three combinations of property parameters are used to define three qualitatively different distributions of thermal conductivity and specific heat. Namely, the first choice of parameters is $K_{c_p} = -0.3$, $K_\lambda = -0.1$, which corresponds to $c_p > 1$ and $\lambda > 1$ across the channel height, (II); the second choice is $K_{c_p} = -0.1$, $K_\lambda = 0.1$, which corresponds to $c_p > 1$ and $\lambda < 1$ profiles, (ID); finally, the third choice is $K_{c_p} = 0.1$, $K_\lambda = 0.3$, which corresponds to $c_p < 1$ and $\lambda < 1$ profiles, (DD).

Results show that regardless of the parameters choice and of the temperature profile, the coupled effect of variable λ and c_p always results in an increase of the maximum energy growth, which is larger in case of linear reference temperature profile and covers a wider range of Prandtl numbers, if compared to the parabolic temperature profile case. Similarly to the results showed for the decoupled property variation, the mechanism to reach the maximum energy growth is speeded-up at small/medium Pr due to an increased growth rate, and slowed-down at medium/large Pr as a consequence of a decreased growth rate.

6.4 Conclusions

The effect of temperature dependent thermal conductivity and specific heat on the non-modal stability of a thermally-stratified channel flow was studied in this Chapter. A fixed destabilizing viscosity profile was considered for all the computations under symmetric

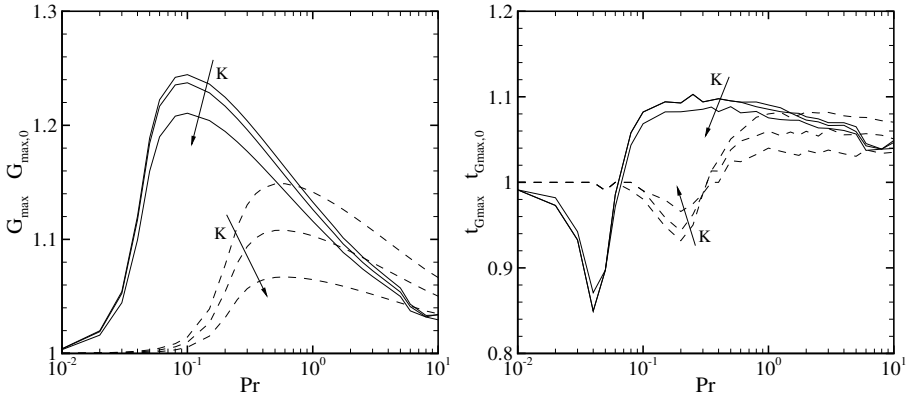

Figure 6.6: G_{max} and $t_{G_{max}}$ modulation under the coupled effect of variable c_p and λ. Increasing K corresponds to II, ID, and DD cases. Solid lines are obtained for a linear reference temperature profile, while dashed lines for a parabolic temperature profile.

and asymmetric temperature profiles. Three different perturbations were applied to the flow, namely a streamwise, spanwise, and oblique perturbation. A parametric study was conducted in order to assess the effect of the Prandtl number and of different rates of variation of λ and c_p across the channel height.

The analysis of the decoupled effects of variable λ and c_p showed that the largest modulation on the energy growth, in terms of both maximum growth and growth rate, is obtained under a spanwise perturbation and a linear temperature profile. Decreasing thermal conductivity ($\lambda < 1$) and increasing specific heat ($c_p > 1$) profiles across the channel height with respect to the reference value are responsible for a larger maximum energy amplifications if compared to a constant c_p and λ case; this mechanism is speeded-up at low Pr and slowed-down at high Pr. The opposite behaviour is observed for reversed λ and c_p profiles.

In case both thermal conductivity and specific heat are temperature dependent, the results obtained for three qualitatively different property distributions across the channel showed that variable properties always lead to an amplification of the maximum energy growth, regardless of the specific profile, i.e., whether they increase or decrease across the channel height, therefore further destabilizing the flow and promoting the transition to turbulence. A similar modulation of the growth rate is observed as in the case of decoupled λ and c_p effects.

The investigation presented in this Chapter demonstrates that substantial modulation of the maximum energy growth and of the growth rate can be obtained if transport properties are temperature dependent. This contribute to the stabilization or destabilization of the flow, promoting or delaying the transition to turbulence accordingly. The results discussed can have practical implication in devising effective flow control strategies.

A.1 Code validation

The validation of the linear stability code for the constant and variable property cases are reported in this Appendix. Hereafter, the number of modes used for the numerical discretization of the equations is referred to as N_{mod}.

A.1.1 Constant properties

Table 1: 10 least stable eigenvalues at $Re = 2000$ from Schmid and Henningson[4].

$\alpha = 1\,\beta = 0$		$\alpha = 0.5\,\beta = 1$		$\alpha = 0.25\,\beta = 2$		$\alpha = 0\,\beta = 2$	
c_r	c_i	c_r	c_i	c_r	c_i	c_r	c_i
0.98418861	-0.01631139	0.97763932	-0.02361068	0.96837728	-0.03974775	0	-0.00323370
0.31210030	-0.01979866	0.37226932	-0.03737398	0.56329537	-0.08548514	0	-0.00507754
0.95256584	-0.04793417	0.93291797	-0.06833204	0.90513428	-0.10299426	0	-0.00693480
0.42418427	-0.07671992	0.49935557	-0.09920592	0.83796079	-0.14010066	0	-0.01107002
0.92078667	-0.07804706	0.88770220	-0.10945538	0.84492959	-0.14965217	0	-0.01310331
0.92091806	-0.07820060	0.88808805	-0.10962449	0.58717755	-0.15289251	0	-0.01982549
0.92094306	-0.07955694	0.88819669	-0.11305351	0.84190728	-0.16629312	0	-0.02173921
0.88932028	-0.11117972	0.84347472	-0.15777756	0.39061440	-0.21452290	0	-0.03078177
0.24936056	-0.13725811	0.31232252	-0.16986946	0.39061296	-0.21452788	0	-0.03284251
0.24936056	-0.13725811	0.31232252	-0.16986946	0.72738833	-0.22753394	0	-0.04449131

Table 2: 10 least stable eigenvalues at $Re = 2000$ calculated in the present study.

$\alpha = 1\,\beta = 0$		$\alpha = 0.5\,\beta = 1$		$\alpha = 0.25\,\beta = 2$		$\alpha = 0\,\beta = 2$	
c_r	c_i	c_r	c_i	c_r	c_i	c_r	c_i
0.98418861	-0.01631139	0.97763932	-0.02361068	0.96837728	-0.03974775	0	-0.00323370
0.31210030	-0.01979866	0.37226932	-0.03737398	0.56329537	-0.08548514	0	-0.00507754
0.95256584	-0.04793416	0.93291797	-0.06833204	0.90513428	-0.10299426	0	-0.00693480
0.42418426	-0.07671992	0.49935556	-0.09920592	0.83796079	-0.14010066	0	-0.01107002
0.92078667	-0.07804706	0.88770220	-0.10945538	0.84492959	-0.14965217	0	-0.01310330
0.92091806	-0.07820060	0.88808805	-0.10962449	0.58717755	-0.15289251	0	-0.01982549
0.92094306	-0.07955694	0.88819669	-0.11305351	0.84190728	-0.16629312	0	-0.02173921
0.88932028	-0.11117972	0.84347472	-0.15777756	0.39061439	-0.21452290	0	-0.03078177
0.24936056	-0.13725811	0.31232252	-0.16986946	0.39061296	-0.21452788	0	-0.03284251
0.24936056	-0.13725811	0.31232252	-0.16986946	0.72738833	-0.22753394	0	-0.04449131

Table 3: 10 least stable eigenvalues at $Re = 10000$, $\alpha = 1$, $\beta = 0$.

Kirchner[15]		Present study ($N_{mod} = 200$)	
c_r	c_i	c_r	c_i
2.375264888204705e-01	3.739670622979582e-03	2.375264888201986e-01	3.739670624484771e-03
9.646309154506005e-01	-3.516727763102714e-02	9.646309154495075e-01	-3.516727763246223e-02
9.646425100392918e-01	-3.518658379244360e-02	9.646425100373770e-01	-3.518658378933739e-02
2.772043438088034e-01	-5.089872725696934e-02	2.772043438124542e-01	-5.089872725457628e-02
9.363165358813165e-01	-6.320149583992261e-02	9.363165358729421e-01	-6.320149583016497e-02
9.363517811647321e-01	-6.325156907426489e-02	9.363517811685679e-01	-6.325156908591481e-02
9.079830546294746e-01	-9.122273543365587e-02	9.079830546196597e-01	-9.122273542616052e-02
9.080563344920409e-01	-9.131286177906131e-02	9.080563345026510e-01	-9.131286173321232e-02
8.796272922071848e-01	-1.192328526196531e-01	8.796272922062681e-01	-1.192328526988089e-01
8.797556958148425e-01	-1.193707310084970e-01	8.797556957047519e-01	-1.193707312161876e-01

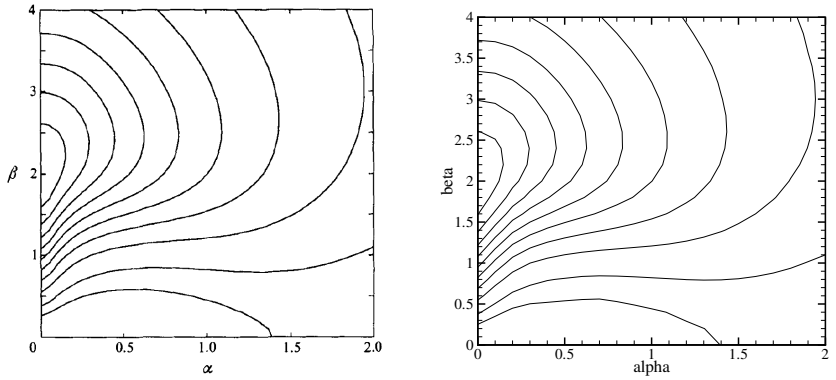

(a) Reddy and Henningson [6]. (b) Present study.

Figure 7: Maximum transient energy growth for $Re = 1000$, $N_{mod} = 101$.

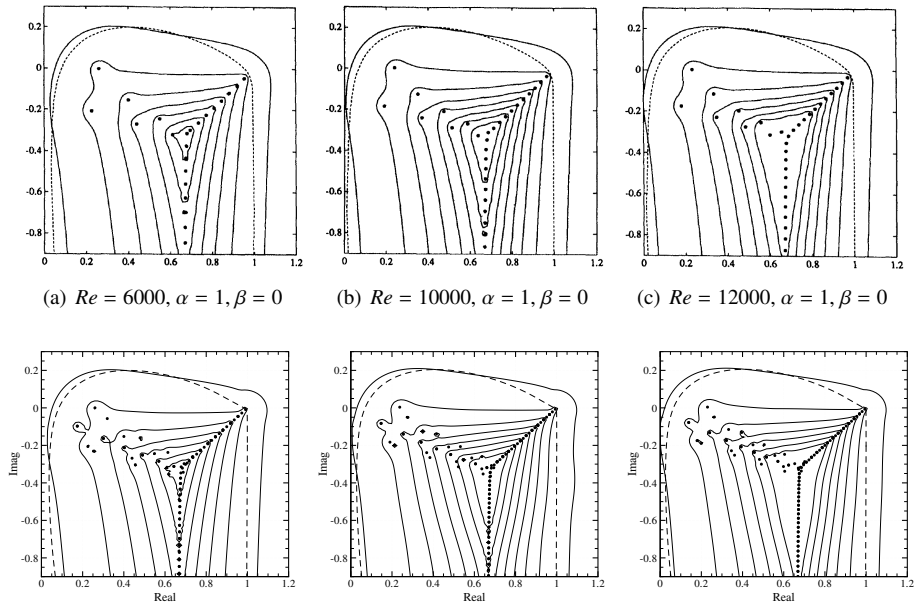

(a) $Re = 6000, \alpha = 1, \beta = 0$ (b) $Re = 10000, \alpha = 1, \beta = 0$ (c) $Re = 12000, \alpha = 1, \beta = 0$

(d) $N_{mod} = 140$ (e) $N_{mod} = 180$ (f) $N_{mod} = 210$

Figure 8: Spectra (symbols), pseudospectra (solid lines) and numerical range (dashed lines) for several combinations of flow parameters. Reference is Reddy *et al.* [7], whereby only the even part of the operator spectrum is shown.

A.1.2 Viscosity stratification

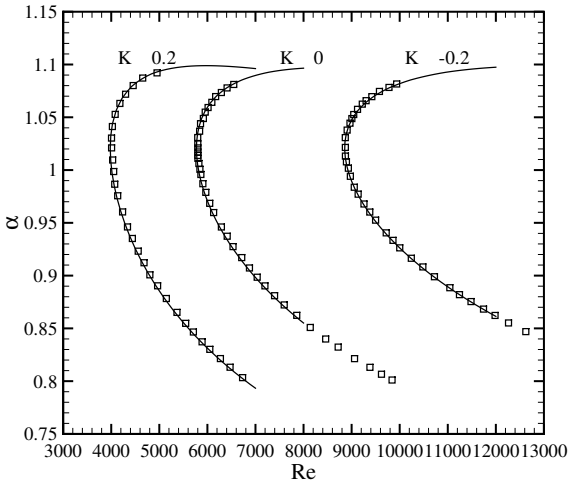

Figure 9: Marginal stability curves for $T = 1 + y$ and $K_\mu = -0.2, 0, 0.2$. Symbols are taken from Wall and Wilson[8], lines are calculated in the present study.

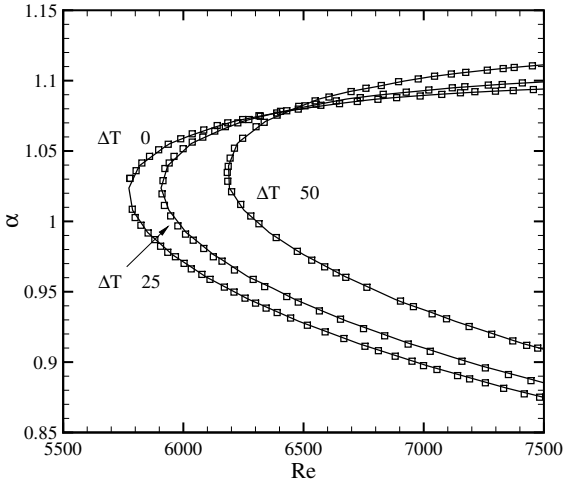

Figure 10: Marginal stability curves for a linear temperature profile with $\Delta T_d = T_{hot} - T_{cold} = 0, 25, 50$ K and $\mu_d = C_1 e^{C_2/T_d}$, whereby $C_1 = 0.00183$ Ns/m and $C_2 = 1879.9$ K. Symbols are taken from Sameen and Govindarajan[10], lines are calculated in the present study.

A.1.3 Heat diffusivity and buoyancy

A channel flow configuration under a linear temperature profile and constant viscosity is considered. Present calculations are performed using (i) a collocated spectral method based on Chebyshev polynomials and (ii) 6^{th} order finite differences (4^{th} order at the walls) using a number of nodes $N = 200$. For the finite difference discretization the convergence of the results is checked doubling the number of discretization nodes. Results obtained by the spectral method do not depend on the number of collocation points for $N > 50$. A perfect agreement is found between the critical Reynolds number is observed between the spectral method and finite differences on $N = 400$. Results for $N = 200$ appear to be closer to the reference ones by Biau and Bottaro[16].

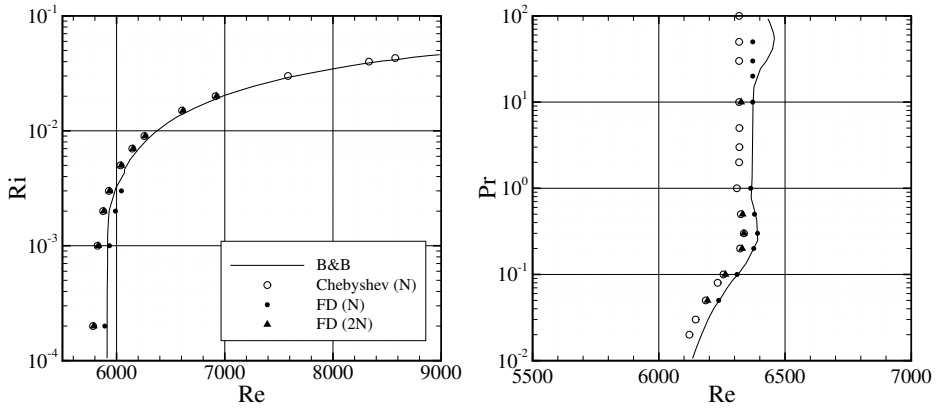

(a) $Pr = 0.7$ (b) $Ri = 10^{-2}$

Figure 11: Critical Reynolds number. Lines are taken from Biau and Bottaro[16], symbols are calculated in the present study.

References

[1] Drazin, P. G., and Reid, W. H., 1981. *Hydrodynamic stability*. Cambridge University Press.

[2] Orszag, S. A., 1971. "Accurate solution of the Orr–Sommerfeld stability equation". *J. Fluid Mech.,* **50**, 12, pp. 689–703.

[3] Trefethen, L. N., Trefethen, A. E., Reddy, S. C., and Driscoll, T. A., 1993. "Hydrodynamic stability without eigenvalues". *Science,* **261**(5121), pp. 578–584.

[4] Schmid, P. J., and Henningson, D. S., 2001. *Stability and Transition Shear Flows*. Springer.

[5] Schmid, P. J., 2007. "Nonmodal stability theory". *Annu. Rev. Fluid Mech.,* **39**, pp. 129–162.

[6] Reddy, S. C., and Henningson, D. S., 1993. "Energy growth in viscous channel flows". *J. Fluid Mech.,* **252**, pp. 209–238.

[7] Reddy, S. C., Schmid, P. J., and Henningson, D. S., 1993. "Pseudospectra of the Orr–Sommerfeld operator". *SIAM J. Appl. Math.,* **53**(1), pp. 15–47.

[8] Wall, D. P., and Wilson, S. K., 1996. "The linear stability of channel flow of fluid with temperature-dependent viscosity". *J. Fluid Mech.,* **323**, pp. 107–132.

[9] Chikkadi, V., Sameen, A., and Govindarajan, R., 2005. "Preventing transition to turbulence: A viscosity stratification does not always help". *Phys. Rev. Lett.,* **95**(26), p. 264504.

[10] Sameen, A., and Govindarajan, R., 2007. "The effect of wall heating on instability of channel flow". *J. Fluid Mech.,* **577**, pp. 417–442.

[11] Sameen, A., Bale, R., and Govindarajan, R., 2011. "The effect of wall heating on instability of channel flow – CORRIGENDUM". *J. Fluid Mech.,* **673**, pp. 603–605.

[12] Govindarajan, R., and Sahu, K. C., 2014. "Instabilities in viscosity-stratified flow". *Annu. Rev. Fluid Mech.,* **46**, pp. 331–353.

[13] Gottlieb, D., and Orszag, S. A., 1977. *Numerical analysis of spectral methods*. SIAM.

[14] Hanifi, A., Schmid, P. J., and Henningson, D. S., 1996. "Transient growth in compressible boundary layer flow". *Phys. Fluids,* **8**(3), pp. 826–837.

[15] Kirchner, N. P., 2000. "Computational aspects of the spectral Galerkin FEM for the Orr–Sommerfeld equation". *Int. J. Numer. Meth. Fl.,* **32**(1), pp. 105–121.

[16] Biau, D., and Bottaro, A., 2004. "The effect of stable thermal stratification on shear flow stability". *Phys. Fluids,* **16**(12), pp. 4742–4745.

7

Conclusions and perspectives

7.1 Conclusions

This thesis presents original research in the field of computational fluid dynamics (CFD) of non-ideal fluid flows and is organized in five self-contained chapters, each addressing a specific problem. The work is subdivided into three parts, namely numerical methods, applications, and analytical study. The material included was partly presented at international conferences and/or appeared in peer-reviewed international scientific journals. Two chapters are already published (Chapter 2 and 4), one is under review for journal publication (Chapter 3), and two were presented and included as conference proceedings and are now under review for journal publication (Chapter 5 and 6). Hereafter, the main conclusions of each Chapter are summarized and discussed.

Numerical methods

Chapter 2 presents the extension of three approximate Riemann solvers to include a complex equation of state model, and reports for the first time the exact derivation of their flux Jacobians. A look-up table interpolation is analyzed an proposed as alternative to the direct solution of the equation of state model. Numerical tests provide the verification of the newly introduced schemes. This chapter constitutes the basis for the simulations performed in Chapter 4 and 5.

- Look-up tables can speed-up the evaluation of fluid thermophysical properties by up to 4 orders of magnitude, depending on the thermodynamic conditions used as input to the EoS, and on the EoS model itself.
- A relatively small number of discretization nodes for the thermodynamic table is found to be sufficient as far as the accuracy and consistency of the interpolated property are concerned.
- Expressions of the numerical convective fluxes and their exact Jacobians are provided for HLLC, AUSM$^+$ and Kurganov–Tadmor central scheme, using a generic equation of state model.
- The main difference with respect to the ideal gas formulation of the convective and viscous Jacobians can be summarized by the need for a general expression of the pressure and temperature derivatives. The differentiation of the viscous fluxes results in additional terms due to temperature-dependent thermophysical properties, i.e., viscosity, thermal conductivity and specific heat.
- The schemes are verified on 1D and 2D test cases using exact analytical solutions when available or by comparison of the numerical solutions obtained using the different schemes. The results do not allow to draw a conclusion on which method performs best. However, the convergence histories for the considered test cases indicate that in order to achieve convergence it is essential to use a consistent discretization of the left-hand-side (Jacobian part) and right-hand-side (flux part) of the equations.

Chapter 3 describes a new flux-conserving treatment of the interface between non-conformal mesh blocks. The devised method is used in Chapter 5 to perform unsteady Reynolds-averaged Navier–Stokes (RANS) simulations of a supersonic turbine.

- The use of an auxiliary hybrid mesh, also called supermesh, at the interface establishes the connectivity among the non-matching mesh blocks and guarantees a conservative flux calculation by construction of the method, avoiding any flux interpolation or the need to enforce additional constraints.

- Despite the application to fluid dynamic simulations, the proposed method can be applied to any other system of conservation laws discretized by finite-volumes.

- The proposed parallelization of the supermesh generation reduces the computational cost of the task linearly with the number of cores.

- The accuracy of the least-squares gradient reconstruction at the interface is studied; two modifications to the standard scheme are proposed and consist of either extending the gradient stencil to include the control volumes of the disconnected block, or to properly set a boundary face value at the interface. It is shown that the latter approach is more robust and thus preferable.

- The effectiveness and conservative nature of the method are verified on five 2D and 3D test cases, which include shock waves and viscous wakes crossing the interface. No spurious solutions are seen at the interface and numerical fluxes conservation is achieved to machine precision. The turbulent simulation of the 2D stator/rotor interaction in a transonic turbine represents an important preliminary verification of the method for the investigation carried out in Chapter 5.

- The numerical stability is proved empirically by solving the equations with three different time integration schemes, namely explicit three-steps Runge–Kutta, implicit backward Euler and BDF2 methods, for subsonic, transonic and supersonic flow regimes. The convergence rates were not found to be affected by the presence of the interface.

Applications

In **Chapter 4** the performance map of a radial compressor (50 kW, 20 mm diameter, 75 krpm design rotational speed) operating with supercritical CO_2 is calculated by means of steady state RANS simulations, and the numerical results are compared to experiments. The methodology developed in Chapter 2 is used here together with a state-of-the-art multiparameter equation of state model, which ensures the best possible accuracy in the fluid property evaluation.

- The comparison between the calculated and measured isentropic efficiency and enthalpy rise provides a reasonable agreement, thus demonstrating the potential of the

methodology and validating the CFD code. However, discrepancies between simulations and experiments are visible: the calculated optimal operating conditions are at lower values of the flow coefficient and the model cannot predict the compressor surge.

- Limitations of the presented CFD simulations are discussed and these are: (i) first order accuracy for the convective fluxes to increase the stability of the simulations; (ii) lack of suitable turbulence models for non-ideal flows and in particular supercritical flows; (iii) the lack of a model for the effective thermal conductivity in the two-phase region in the framework of standard RANS modeling under the homogeneous mixture approximation of the fluid.

- Possible inaccuracy of the used experimental data are also discussed and depend on: (i) the design inlet conditions are given without specifying whether the reported properties are static or total, which in the supercritical region can lead to large differences in terms of thermodynamic and transport properties; (ii) the inlet conditions measured during the experiments are given as a temperature and pressure range, which translates in an uncertainty on the inlet density of 100%; (iii) uncertainties related to measurement equipment, flow leakage, windage losses, etc., which are not quantified in the experimental campaign and are not taken into account in the CFD simulations.

- Possible local condensation of CO_2 is investigated identifying the control volumes whose calculated thermodynamic state falls inside the vapour-liquid equilibrium region. They are mainly located at the leading edge of the rotor main-blade, and their extent largely increases with the rotational speed. Similar conditions are found at the sharp trailing edge of the rotor blades and at the leading edge of the diffuser wedges, though covering regions smaller in size and showing a weaker dependence on the rotational speed. Further investigations are needed to assess whether the residence time of the flow is long enough to trigger the condensation mechanism and whether this phenomenon can affect the machine performance.

Chapter 5 investigates the stator/rotor interaction in an ORC supersonic turbine (60-170 kW, 26 krpm design rotational speed, pressure ratio > 100, maximum vane Mach number $M \approx 3$). The machine is a single stage radial turbine and operates with toluene at slightly subcritical state at the inlet. Time-averaged and unsteady blade loads are presented, and the main flow structures and their interactions are described for two off-design rotational speeds.

- The machine operates more efficiently at high rotational speeds due to relative transonic inlet conditions in the rotor, and a less intense shock waves configuration as a consequence.

- The isentropic efficiency of the turbine is only weakly unsteady. The frequency of the oscillations is twice the rotor blade-passing-frequency, and the amplitude is 0.5%.

- The main losses are due to the viscous wakes of the stator blades and to the large flow separations induced by oblique shock waves on the suction side of the rotor blades.

- The shock waves and viscous wakes interactions and their time evolution were studied. Similar patterns are observed for both considered rotational speeds, with the exception of the presence of stationary bow shock waves at the leading edge of the rotor blades in case of low rotational speed, due to relative supersonic conditions at the inlet of the rotor.

- Rotor blade loads show highly unsteady trends featuring ample and sharp fluctuations caused by the shocks impingement on the blades. Force fluctuations in the radial and tangential direction can reach up to 60% and 30% of their time averaged values, respectively; the torque also shows large fluctuations and a change in sign in case of high rotational speed.

- The analysis of the frequency content of the flow field and of the loads separates periodic contributions and provides useful information for the structural design of the blades. Results show that most of the content is confined to the first 5-10 blade-passing-frequency harmonics.

- The results presented in this Chapter demonstrate how unsteady CFD simulations can provide crucial insights in the design process of efficient ORC turbines. Shape optimization methodologies of the rotor blades could benefit from the use of unsteady CFD data aiming at the minimization of the blade loads fluctuations by suppressing the highlighted shock interactions.

Analytical study

Chapter 6 documents a linear stability analysis of a thermally-stratified channel flow with temperature dependent transport properties. The aim is to assess whether variable thermal conductivity λ and specific heat c_p contribute to the stabilization of a laminar flow or promote its transition to a turbulent state.

- Temperature dependent transport properties can significantly modulate the transient energy growth of perturbations in terms of both maximum amplification and growth rate over a wide range of Prandtl numbers Pr, therefore contributing to the stabilization/destabilization of the flow. The maximum modulation is obtained under a spanwise perturbation and a linear reference temperature profile.

- The effect of decoupled variations of λ and c_p, i.e., only one property varies while the other is constant, can either enhance or suppress the maximum energy growth. Namely, $\lambda/\lambda_{ref} < 1$ and $c_p/c_{p,ref} > 1$ across the channel height both result in larger energy amplifications if compared to a constant λ or c_p flow. The opposite behaviour is observed for reversed property profiles.

- The coupled variation of temperature dependent properties always result in an enhancement of the maximum energy growth of spanwise perturbations regardless of whether λ and c_p decrease or increase with respect to their reference value.

- The growth rate of spanwise perturbations is affected by temperature dependent transport properties: if $\lambda/\lambda_{ref} < 1$ across the channel height, the growth rate increases for low/medium Pr and reduces in the medium/high Pr range. The same modulation is observed for $c_p/c_{p,ref} > 1$, while the opposite behaviour is observed for reversed property profiles.

- Appropriate transport property distributions across the channel might be used to devise effective flow control strategies.

7.2 Perspectives

The contribution of this thesis is twofold and consists of (i) the development of numerical techniques for the simulation of compressible flows of non-ideal fluids governed by complex thermophysical models, and of (ii) the study of the fluid dynamic behavior of such non-conventional flows from both an application perspective, considering turbomachines operating near the vapour-liquid critical point, and a fundamental point of view, investigating their hydrodynamic stability. The documented work led to improved prediction capabilities and fluid dynamic understanding which can be beneficial for the design of efficient devices operating with non-ideal fluid flows. Despite the presented study addressed several research questions, others lie on the road still waiting for an answer.

One of the main limitation of studying non-ideal fluid flows using computational tools is the lack of high quality and reliable experimental data to validate the numerical codes. On the one hand, it is reasonable to believe that computer programs validated for ideal gases and then properly adapted to include state-of-the-art thermodynamic models will perform well when applied to simulate non-ideal fluid flows also. On the other hand, extensive code validation is needed before such numerical methods can be used to support the design of devices operating with non-ideal fluids and before they can be an integral part of the development and optimization of non-conventional machines. A strong effort is therefore needed to perform experimental campaigns using fluids evolving in the proximity of their vapour-liquid critical point, and to provide the scientific community with data concerning both fundamental flows, e.g., nozzle expansion, boundary layer flow, heat exchange in simple geometries, and flows occurring in technical applications, e.g., turbomachines.

From a theoretical and modeling standpoint, three of the most promising areas of research which in the author's opinion might lead to the most significant practical implications are listed hereafter.

1. **Turbulence modeling.** Turbulence models are crucial to study from an engineering point of view complex or industrial applications, for which the Reynolds-averaged

Navier–Stokes approach often remains the only affordable option in terms of computational cost. It is a well documented fact that standard turbulence models, which were developed for simple flows of ideal gases, present severe limitations when applied to non-ideal fluid flows, especially when heat transfer prediction close to the fluid vapour-liquid critical point are concerned. Fundamental understanding of the fluid mechanics and the availability of large set of data on different flow configurations are needed in order to develop turbulence models which are suitable for non-ideal fluid flows. Direct numerical simulation (DNS) is nowadays a viable option to such aim, as demonstrated by several research groups already active in the field.

2. **Hydrodynamic stability.** Flow transition from a laminar to a turbulent state has crucial consequences on a machine performance, acting for example on the skin friction and heat transfer coefficient. The transition process has been extensively studied on ideal fluids in the past decades leading to a defined general picture of the involved mechanisms. However, the sharp and non-linear variation of thermophysical properties in the vapour-liquid critical point region can have a strong stabilizing/destabilizing effect on the flow, therefore changing the characteristics of transition. Linear stability analysis and DNS simulations are fundamental tools to provide the insights needed to understand the transition process in non-ideal fluid flows. Chapter 6 of this thesis is a first step in this direction, however on a simplified flow configuration which used simple relations for the fluid thermophysical properties and which did not include the effect of density, which sharply varies above the critical point.

3. **Fluid condensation.** As demonstrated in Chapter 4 of this thesis, conditions for local fluid condensation might be met in turbomachines operating with trans- and supercritical fluids. The occurrence of this phenomenon can strongly influence the machine operation and performance, and it therefore needs to be investigated into details. From a scientific point of view, the development of suitable nucleation models for the transcritical thermodynamic region to be coupled to computational fluid dynamic codes are the main challenge which has to be tackled studying the fundamentals of the process using theoretical and analytical models devised from first principles, and supporting them with experiments.

Acknowledgements

Writing this thesis is only the last step of a long journey began quite some time ago. I believe the first persons I have to thank if I was able to pursue this path are my high school teachers of physics and mathematics, Crippa and Malvicini: I am quite sure this whole thing would have not been the same without your passion and enthusiasm.

I also want to thank the professors I met during my studies at Politecnico di Milano, who gradually made me fall in love with fluid dynamics, in particular dr. Guardone with whom I also had the chance to discuss, learn, and collaborate while I was in Delft.

A special mention goes to prof. Quartapelle, whose attitude and teachings made me realize scientific research was what I wanted to do. If I became so curious and enthusiastic about science in general and fluid dynamics in particular I owe much to you.

I am grateful to my promotor, prof. Colonna, who believed in me when I first came to Delft and never stopped doing so throughout the years, and gave me the academic freedom to investigate the topics that intrigued me the most. There are no words that can fully express my gratitude to my supervisor, dr. Pecnik, and how lucky I was to work with him. It is mainly thanks to him if I could achieve what is included in this thesis and if I began developing my own ideas and view on scientific research. I value very much the fact that our discussions were not limited to research-related topics, but spanned all aspects of life. These four years under the supervision of both of you were unique, and I hope we will continue to collaborate long in the future.

My deepest gratitude goes to my parents, Patrizia and Roberto, who always supported me and made me feel loved, no matter what. I would not be here without them and my whole family.

I also want to thank all my Italian friends with whom I grew up and shared so much (I still do), all the new friends I have met in the Netherlands, my colleagues and office mates, rugby mates, people I met just for a coffee or a beer, or during one of my trips around the world. In a way or another you all contributed to shape myself, my mind, ideas, and thoughts, and for that I will always be grateful to each one of you.

A special thought goes to Anna, to all the days and nights spent with you talking and discussing about any possible topics, to all the happy and also difficult moments we shared, and to the fact that every single day with you is a surprise: you enrich me.

Finally, I would like to express my gratitude to the examination committee members. I appreciate their interest in my work and their time devoted to evaluating this dissertation.

Enrico Rinaldi
Delft, September 8th, 2015

List of publications

Journal papers

Rinaldi, E., Colonna, P., and Pecnik, R., 2015. "Stator/rotor interaction in a supersonic ORC turbine". *J. Turbomach.*, Under review.

Rinaldi, E., Colonna, P., and Pecnik, R., 2015. "Flux-conserving treatment of non-conformal interfaces for finite volume discretization of conservation laws". *Comp. Fluids*, **120**, pp. 126–139.

Rinaldi, E., Pecnik, R., and Colonna, P., 2015. "Computational Fluid Dynamic Simulation of a Supercritical CO_2 Compressor Performance Map". *J. Eng. Gas Turb. Power*, **135**(7), pp. 072602.

Rinaldi, E., Pecnik, R., and Colonna, P., 2014. "Exact Jacobians for implicit Navier–Stokes simulations of equilibrium real gas flows". *J. Comput. Phys.*, **270**, pp. 459–477.

Guardone, A., Colonna, P., Casati, E., and Rinaldi, E., 2014. "Non-classical gas dynamics of vapour mixtures". *J. Fluid Mech.*, **741**, pp. 681–701.

Pecnik, R., Rinaldi, E., and Colonna, P., 2012. "Computational Fluid Dynamic Simulation of a Supercritical CO_2 Compressor Performance Map". *J. Eng. Gas Turb. Power*, **134**(12), pp. 122301.

Conference proceedings

Rinaldi, E., Pecnik, R., and Colonna, P., 2015. "Unsteady RANS simulation of the off-design operation of a high expansion ratio ORC radial turbine". *Proceedings of the 3rd International Seminar on ORC Power Systems – ASME ORC-2015*, Bruxelles - Belgium, pp. 1–10.

Rinaldi, E., Boersma, B.J., and Pecnik, R., 2015. "Transient energy growth modulation by temperature dependent transport properties in a stratified plane Poiseuille flow". *Presented at the 15th European Turbulence Conference – ETC-2015*, Delft - The Netherlands, pp. 1–2.

Rinaldi, E., Pecnik, R., and Colonna, P., 2014. "Numerical computation of the performance map of a supercritical CO_2 radial compressor by means of three dimensional CFD simulations". *Proceedings of the ASME Turbo Expo 3B*, Düsseldorf - Germany, pp. 1–10.

Rinaldi, E., Suarez Raspopov, R., Colonna, P., and Pecnik, R., 2014. "Modeling curvature effects on turbulence transition for turbomachinery flows". *Proceedings of the ASME Turbo Expo*, Düsseldorf - Germany, pp. 1–11.

Rinaldi, E., Buonocore, A., Pecnik, R., and Colonna, P., 2013. "Inviscid stator/rotor interaction of a single stage high expansion ratio ORC turbine". *Presented at the 2nd International Seminar on ORC Power Systems – ASME ORC-2013*, Delft - The Netherlands, pp. 1–4.

Rinaldi, E., Pecnik, R., and Colonna, P., 2013. "Steady state CFD investigation of a radial compressor operating with supercritical CO_2". *Proceedings of the ASME Turbo Expo 8*, San Antonio, TX - United States, pp. 1–11.

Casati, E., Rinaldi, E., Guardone, A., and Colonna, P., 2012. "Nonclassical Gasdynamics of Vapor Mixtures". *Proceedings of the 6th European Congress on Computational Methods in Applied Sciences and Engineering – ECCOMAS 2012*, Vienna - Austria, pp. 4201–4211.

Rinaldi, E., Pecnik, R., and Colonna, P., 2012. "Accurate and Efficient Look-up Table Approach for Dense Gas Flow Simulations". *Proceedings of the 6th European Congress on Computational Methods in Applied Sciences and Engineering – ECCOMAS 2012*, Vienna - Austria, pp. 8690–8704.

Pecnik, R., Rinaldi, E., and Colonna, P., 2012. "Computational fluid dynamics of a radial compressor operating with supercritical CO_2". *Proceedings of the ASME Turbo Expo 5*, Copenhagen - Denmark, pp. 985–995.

About the author

Enrico Rinaldi was born in Milan, Italy, on May, 7^{th}, 1985. After completing a 5-years study period at Liceo Scientifico Francesco Severi, Milano, he received his high school diploma with majors in Mathematics, Physics, and Informatics. After a long wobbling over a choice, he finally decided to enroll for the Bachelor program in Aerospace Engineering at Politecnico di Milano and in 2008 he received his BSc. Enrico then continued his studies following the Aerodynamics track of Aeronautical Engineering at the same University. He carried out a Master project under the supervision and guidance of Prof.dr. Luigi Quartapelle, and in December 2010 he received his MSc degree. Before completing the Master program Enrico already knew what he wanted for his future: pursuing a PhD in the field of fluid dynamics. Few month later, in June 2011, he moved to Delft, The Netherlands, to start his 4-years research journey at the Process & Energy department of the Delft University of Technology under the supervision of Prof.dr. Piero Colonna and Dr. Rene Pecnik. During these years he had the chance to explore different aspects of computational fluid dynamics and to contribute to the research in this field, presenting his work at several international conferences and on international peer reviewed scientific journals. This book wraps up the last 48 months of enthusiastic and frenzied studies in Delft.